

School of Science  
Department of Physics and Astronomy  
Master Degree in Astrophysics and Cosmology

**Evidence for a complex acceleration  
mechanism in the radio relics of MACS  
J1752+4440**

Supervisor:

Prof. Annalisa Bonafede

Submitted by:

Maicol Della Chiesa

Co-supervisor:

Dr. Andrea Botteon



**THIS THESIS WORK WAS DONE AS  
PART OF THE RESEARCH ACTIVITY  
OF THE ISTITUTO DI  
RADIOASTRONOMIA - ISTITUTO  
NAZIONALE DI ASTROFISICA  
(BOLOGNA)**





# Abstract

Galaxy clusters are the most massive gravitationally bound structures in the Universe. In particular, observations in the radio band reveal their diffuse synchrotron emission which, in recent years, brought their complex internal structure to light. Radio relics are one of the types of diffuse radio sources, located at the outskirts of merging galaxy clusters, characterized by elongated arc-like shapes, with sizes ranging between 0.5 to 2 Mpc, and highly polarized emission. They are thought to trace shock waves created in the intra cluster medium (ICM) during a binary, head-on, merger event.

MACS J1752+4440 is a remarkable case of cluster hosting a double relic system, in which two radio relics are found on opposite sides of the cluster.

In this thesis work, we used LOFAR HBA (120 – 168 MHz) data from the LoTSS survey, together with new uGMRT band 3 (300 – 500 MHz) and band 4 (550 – 750 MHz) and new JVLA L-band (1 – 2 GHz) observations, to perform a spectral study at high resolution. We detect a complex morphology of the North-Eastern relic, highlighting multiple substructures, which could reveal the fine details of a merger shock propagating into the ICM.

Through the spectral analysis, we investigated the complexity of the double-relic system, observing a double-peaked surface brightness and spectral index profile for the NE relic. Moreover, we observed surprisingly flat integrated spectral indices for both relics, at  $\alpha_{int}^{NE} = -0.91 \pm 0.06$  and  $\alpha_{int}^{SW} = -0.83 \pm 0.05$ , different from previous literature studies. Through a spectral index map, we studied the spatial variation of the spectral index, observing a coherent trend with the observed substructures.

Assuming diffusive shock acceleration, we estimated an injection Mach number of  $\mathcal{M}_{NE} = 3.12_{-0.42}^{+0.82}$  and  $\mathcal{M}_{SW} = 4.19_{-0.50}^{+0.94}$ , in agreement with low shock Mach numbers. We propose a scenario for the observed relic morphology, in which the observed substructures are generated by multiple shock surfaces, and investigate

its viability.

By performing a spectral curvature analysis for both relics, generating color-color plots and a spectral curvature map, we observed two “concave” spectra represented by positive spectral curvature, in contrast with particle ageing models, which can be explained in a scenario in which different components are observed in projection. To investigate on this, we performed a polarization study on both relics, finding no correlation between the polarization fraction and the spectral curvature. Finally, we measure an equipartition magnetic field, for both radio relics, of  $B \sim 1\mu\text{G}$ .

# Table of Contents

<b>1</b>	<b>Galaxy clusters</b>	<b>1</b>
1.1	Emission from clusters of galaxies . . . . .	2
<b>2</b>	<b>Non-thermal emission in galaxy clusters</b>	<b>6</b>
2.1	Radio Halos . . . . .	9
2.2	Radio relics . . . . .	11
2.2.1	Diffusive Shock Acceleration as radio relic origin . . . . .	14
<b>3</b>	<b>MACS J1752+4440</b>	<b>17</b>
3.1	This thesis . . . . .	21
<b>4</b>	<b>Observing in the Radio band</b>	<b>22</b>
4.1	Single dish radio telescopes and interferometry . . . . .	23
4.2	WSCLEAN . . . . .	28
<b>5</b>	<b>Data reduction and imaging of MACS J1752+4440</b>	<b>30</b>
5.1	Observations and data reduction . . . . .	30
5.1.1	LOFAR . . . . .	30
5.1.2	uGMRT . . . . .	32
5.1.3	JVLA . . . . .	33
5.2	Imaging . . . . .	35
5.3	Radio Images . . . . .	36
<b>6</b>	<b>Discussion</b>	<b>40</b>
6.1	Integrated fluxes and spectrum . . . . .	40
6.2	Surface brightness and spectral index profiles . . . . .	47
6.2.1	Mach Numbers . . . . .	56
6.3	Evidence of a second shock surface? . . . . .	59
6.4	Spectral curvature . . . . .	62

6.5	Polarization . . . . .	67
6.6	Physical parameters . . . . .	72
<b>7</b>	<b>Conclusions and future perspective</b>	<b>74</b>



# Chapter 1

## Galaxy clusters

Galaxy clusters are the most massive gravitationally bound structures in the Universe, with masses reaching  $10^{15} M_{\odot}$  and sizes, defined by the virial radius ( $R_{vir}$ ), of the order of  $\sim 1 - 3$  Mpc. Although they were first noticed as gatherings of galaxies in optical observations, they're more than just a random collection of galaxies. Our current understanding reveals that these systems are more intricate than initially anticipated, as the galaxies within them account for just a minor portion of their overall mass. Studies as old as [Zwicky \(1937\)](#) show that a substantial amount of obscure matter is needed to bind the observed galaxies into long lived structures, like the Coma cluster. It is now understood that the majority, roughly 80%, of the mass in a cluster exists in the enigmatic form of dark matter, while the ordinary matter, referred to as baryonic matter, contributes only a modest portion, around 20%, to the entire mass. Most of this baryonic matter is in the form of a hot ( $T = \sim 10^7 - 10^8$  K), diluted ( $n = \sim 10^{-3} \text{ cm}^{-3}$ ) thermal plasma typically known as Intra Cluster Medium (ICM), making up for  $\sim 15\%$  of the total mass, while stars and galaxies only account for about  $\sim 5\%$  of the cluster mass.

The current theory of structure formation states that galaxy clusters form through hierarchical formation processes, following a series of merger and accretion events lead by gravity and dark matter, dominating the gravitational field. This process is described in the standard cosmological model ( $\Lambda$ CDM) as a “bottom-up” scenario, forming clusters at low redshift ( $z < 0.1$ ; [Kravtsov and Borgani, 2012](#)). Merger events are of fundamental importance, as the collision of two galaxy clusters generates the most energetic phenomena in the universe since the Big Bang, dissipating energies as large as  $10^{64}$  erg in just a crossing life-time ( $\sim 10^9$  yr). The greater portion of this energy is dissipated by shocks, heating the ICM.

## 1.1 Emission from clusters of galaxies

Due to their diversified composition, galaxy clusters can be observed at different wavelengths, appearing completely different in each band (Fig. 1.1). In the Optical and Infra-Red (IR) band, we observe light emitted by galaxies, while in the X-rays we find the thermal emission of the ICM. The radio band presents peculiar features, highlighting the presence of cosmic-rays and magnetic fields in the ICM through non-thermal emission (Sec. 2).

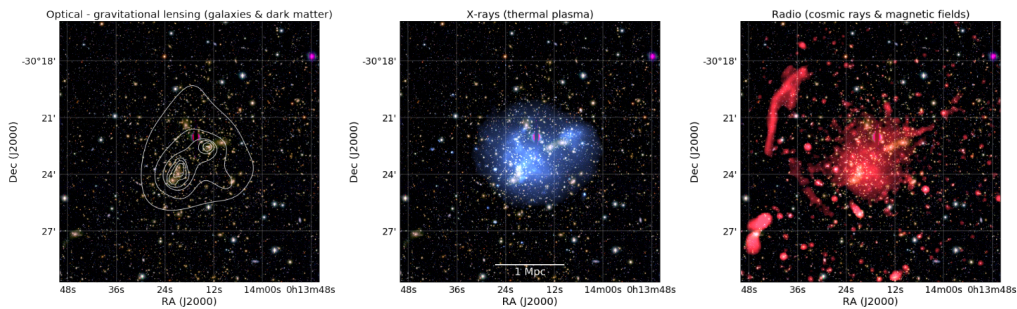


**Figure 1.1:** The galaxy cluster Abell 2744. *Left:* optical view, white contours representing the mass surface density. *Center:* X-ray emission from the thermal ICM (blue). *Right:* Radio emission in red (VLA 1 – 4 GHz), tracing cosmic rays and magnetic fields. From [van Weeren et al. \(2019\)](#).

Optical/IR emission: Stars and galaxies are the main contributors to Optical and near-IR emission we observe from galaxy clusters, in the form of black body emission coupled with emission lines from recombination processes. Observations in these bands show how the population of galaxies in clusters is dominated by early-type galaxies (ellipticals and lenticulars). Of fundamental importance is the interplay between the ICM and cluster galaxies, generating ram pressure ablation and gas stripping processes, observed in the major presence of “HI deficient” galaxies. As ram pressure scales with  $\rho_{ICM}v^2$ , where  $\rho_{ICM}$  is the density of the ICM and  $v$  is the speed of the cluster galaxies, these processes are suggested to be most important in high density regions, i.e. the core of galaxy clusters, in which the most massive galaxies in the universe are found, known as the “Brightest Cluster Galaxies” (BCG). Star formation is therefore suppressed and most of the cluster galaxies can be identified as “red sequence” galaxies ([Allen et al., 2011](#)).

X-ray emission: The X-ray image of Fig. 1.1 demonstrates the power of X-ray astronomy in the study of clusters of galaxies. Extended X-ray emission is a ubiquitous feature of massive clusters of galaxies, arising from the diffuse ICM as thermal

bremsstrahlung emission (free-free emission), along with different radiative processes which include recombination (free-bound emission), and primarily line radiation (bound-bound emission) (Allen et al., 2011). X-ray observations provide a very powerful probe of the gravitational potential of the cluster, enabling the distribution of both the hot gas and the total gravitating mass to be determined.

Sarazin (1986) showed, through the first all-sky survey of galaxy clusters, using data collected by the long dismissed *Uhuru* satellite, that the majority of galaxy clusters are X-ray luminous objects, with typical X-ray luminosities of  $L_X \sim 10^{43} - 10^{45} \text{ erg s}^{-1}$ .

Many important steps in our understanding of X-ray emission in galaxy clusters have been made thanks to the advent of further X-ray missions since the 90s. The *ROSAT* satellite discovered hundreds of new clusters in the nearby and distant universe, *ASCA* and *Beppo-SAX* satellites unveiled signs of complex physics ruling the ICM. At last, the latest generation of X-ray satellites, *Chandra* and *XMM-Newton*, revealed features in the ICM of clusters, connected with the surface brightness and temperature distribution of the cluster gas, together with an understanding of the interplay between the complex physics of the hot ICM and detailed processes of star formation (Rosati et al., 2002).

Of peculiar relevance for this work is the characterization of shock fronts in X-ray observations of galaxy clusters (Markevitch et al., 2005; Markevitch and Vikhlinin, 2007; Botteon et al., 2016).

Shock fronts are discontinuities propagating in a fluid with abrupt jumps in density, temperature and pressure traveling at a speed faster than the local speed of sound. In galaxy clusters, they can be produced in different ways: at cluster centers via the outburst of supermassive black holes, beyond a cluster's virial radius by substructures accreted from cosmic filaments, or via the collision of (at least) two subclusters, called merger shocks. When a subcluster falls through the gravitational potential of a main cluster, the gaseous component of the subcluster experiences ram pressure and deceleration (ZuHone and Su, 2022).

Following Sarazin et al. (2002), it is simple to show the analytical argument that can be used to estimate the kinematics of an individual binary cluster merger collision. Considering two sub-clusters of mass  $M_1$  and  $M_2$ , merging at time  $t_m$  and colliding from a large distance  $d_0$ , with non zero angular momentum, we can assume that the two sub-clusters are point masses, expanding away from one another in the Hubble flow, with zero radial velocity at distance  $d_0$ . The collapse can be studied

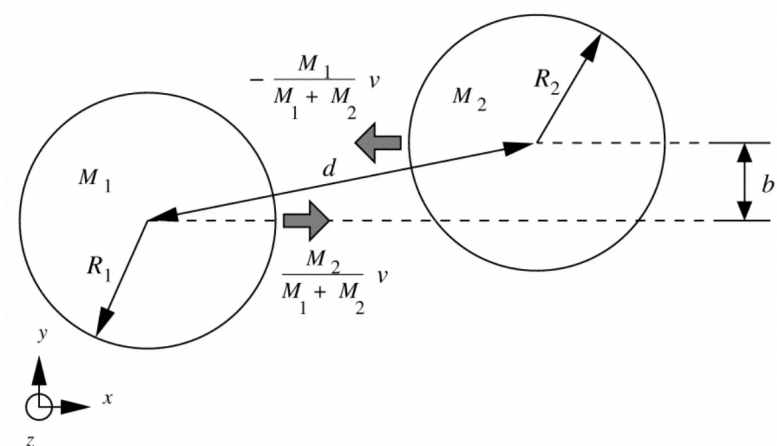


**Figure 1.2:** Schematic diagram of the kinematics for a binary cluster merger, with sub-clusters of masses  $M_1$  and  $M_2$  and radii  $R_1$  and  $R_2$ . The distance between the clusters is  $d$  and the impact parameter is  $b$ . The initial relative velocity is  $v$ . From [Sarazin and Ricker \(2001\)](#)

as the orbit of two point masses, which largest separation is given by the Kepler third law as:

$$d_0 \simeq [2G(M_1 + M_2)]^{1/3} \left( \frac{t_m}{\pi} \right)^{2/3} \quad (1.1)$$

$$\simeq 4.5 \left( \frac{M_1 + M_2}{10^{15} M_\odot} \right)^{1/3} \left( \frac{t_m}{10^{10} \text{yr}} \right)^{2/3} \quad [\text{Gyr}], \quad (1.2)$$

where  $d_0$  does not significantly affect the collision velocity as long as it is large, and the infall velocity approaches free-fall from infinity. Considering the angular momentum conservation, it is possible to derive the velocity of the merger at a distance  $d$  as:

$$v \simeq 2930 \left( \frac{M_1 + M_2}{10^{15} M_\odot} \right)^{1/2} \left( \frac{D}{1 \text{Mpc}} \right)^{-1/2} \left[ \frac{1 - \frac{d}{d_0}}{1 - \left( \frac{b}{d_0} \right)^2} \right] \quad [\text{km s}^{-1}], \quad (1.3)$$

where  $b$  is the impact parameter. Fig. 1.2 shows a sketch of the merger. Because of the high impact velocity, the motions in galaxy cluster mergers are moderately supersonic. Therefore, shock waves are driven in the ICM.

As a consequence, merger shocks are observed in X-rays as a discontinuity in the ICM surface brightness and a jump in temperature from the pre- to the post-shock region. However, the detection of shocks in X-ray wavelengths is hampered by the low brightness of the ICM outside of the cluster core ([Markevitch and Vikhlinin, 2007](#)).

Thanks to the new state of the art instruments working in the millimeter waves (New IRAM KIDs Array 2; [Adam et al., 2018](#)), cluster merger shocks can be detected through the Sunyaev-Zel'dovich (SZ) effect. This physical process is based on the presence of hot electrons in the ICM, which can lead to a small distortion of the CMB spectrum via Inverse Compton scattering.

An example of shock front, as seen in an X-ray image, can be seen in Fig. 1.3.

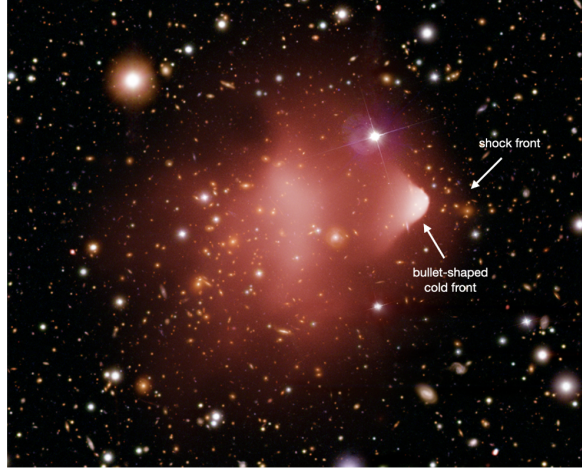


**Figure 1.3:** Composite X-ray and Optical image of the Bullet Cluster (1E 0657-56). From [Markevitch \(2006\)](#).

The strength of a shock can be described by the sonic Mach number, which is the ratio between the flow velocity and the sound speed of the medium

$$\mathcal{M} = v/c_s$$

and the sound speed,  $c_s$  can be calculated as

$$c_s = \sqrt{\frac{\Gamma k_B T}{\mu m_p}}$$

where  $T$  is the thermal temperature of the medium,  $\Gamma = 5/3$  is the specific heat for a monoatomic gas,  $k_B$  is the Boltzmann constant,  $m_p$  is the proton mass and  $\mu \approx 0.6$  is the average molecular weight.

Although the time for shock fronts to be present near the cluster center, where they are most easily detected, is relatively short, as of today, tenths of merger shocks have been detected, and studied, in the X-rays. Additionally, shocks can also be detected at radio frequencies, through synchrotron emission, as radio relics, of which we give an in-depth description in the next chapter.

# Chapter 2

## Non-thermal emission in galaxy clusters

Radio emission in galaxy clusters is of fundamental importance in understanding the nature of their clusters sources, and it can be classified in two main categories: emission coming from compact and extended sources (see e.g. the review by [van Weeren et al., 2019](#)). Compact sources are active galactic nuclei (AGN) hosted in the cluster and emitting radio synchrotron emission. These radio galaxies can span a very wide range of sizes (from  $\sim 1$  kpc up to  $\sim 1$  Mpc) and they usually show different morphologies with respect to field radio galaxies, due to the interaction with the ICM, as described in the previous chapter.

Of further importance is the observation of extended radio sources, highlighting the presence of GeV cosmic rays (CR), not directly associated with radio galaxies ([Willson, 1970](#)). The observed emission is synchrotron emission, coming from cosmic ray electrons (CRE) with very high Lorentz Factor ( $\gamma > 10^{3-4}$ , corresponding to GeV energies) in the presence of  $\sim \mu$ Gauss ICM magnetic fields. To better understand this statement, a brief discussion of synchrotron theory is given.

### Synchrotron theory

Charged particles accelerated by a magnetic field will radiate. For non-relativistic velocities the complete nature of the radiation is rather simple and is called cyclotron radiation.

However, for extremely relativistic particles the frequency spectrum is much more complex and can extend to many times the gyration frequency. This radiation is known as *synchrotron* radiation.

The energy distribution of cosmic-ray electrons in most synchrotron sources is roughly a power law:

$$N(E)dE \propto E^{-\delta}dE, \quad (2.1)$$

where  $n(E)dE$  is the number of electrons per unit volume with energies  $E$  to  $E+dE$ . Starting from the approximation that each electron radiates all of its average power as:

$$P = -\frac{dE}{dt} = \frac{4}{3}\sigma_T\beta^2\gamma^2cU_B, \quad (2.2)$$

where  $\sigma_T$  is the Thomson cross section,  $\beta = v/c$ ,  $\gamma = (1 - \beta^2)^{-1/2}$  is the Lorentz factor and  $U_B = B^2/8\pi$  is the magnetic energy density, the spectrum of an optically-thin synchrotron source can be calculated with good accuracy, and can be approximated as a power-law distribution in frequency as:

$$S(\nu) \propto \nu^\alpha, \quad (2.3)$$

where  $\alpha$  represents the *spectral index* and is related to the energy distribution of CRe as

$$\alpha = -\frac{\delta - 1}{2}. \quad (2.4)$$

In the case of a self absorbed source the spectrum of synchrotron radiation gets heavily modified by absorption, dividing the spectrum in two different sections, separated at the frequency in which the source changes from optically thick to optically thin. In particular, in the optically thick region the totally intensity spectrum is described by  $S(\nu) \propto \nu^{5/2}$ .

As previously stated, the observed extended synchrotron radiation coming from galaxy clusters is estimated to be produced by extremely relativistic electrons, with Lorentz factors  $\gamma > 10^3$ . Even though galaxy clusters host central active galaxies, they are not sufficient by themselves to power this kind of diffuse radio emission. Furthermore, the radiative timescale of the electrons at the required energies for the observed emission ( $\sim 10^8$  years) is much shorter than the time required for these electrons to diffuse across the cooling region ( $\gg 10^9$  years), typically known as the “slow diffusion problem” (Jaffe (1977); Brunetti, 2003). Several physical mechanisms have been proposed as possibly responsible for the radio emission: reacceleration of pre-existing, low-energy electrons in the intracluster medium (ICM) by merger or accretion shocks, reacceleration of thermal electrons

by turbulence and the generation of secondary particles via inelastic collisions between relativistic cosmic-ray protons and thermal protons. A brief overview of these processes can be outlined as follows:

- Second order Fermi acceleration (Fermi-II): this is a stochastic process where particles scatter from magnetic inhomogeneities, for example from magnetohydrodynamical (MHD) turbulence (Brunetti et al., 2001; Schlickeiser et al., 1987). Particles can either gain or lose energy when scattering. When the motions are random, the probability for a head-on collision, where energy is gained, is slightly larger. Because of its random nature, second order Fermi acceleration is an inefficient process (Brunetti and Jones, 2014).
- Adiabatic compression: a shock wave can adiabatically compress a bubble/lobe/cocoon of (old) relativistic radio plasma from an AGN. Due to the compression, the CR electrons in the cocoon re-gain energy boosting the radio synchrotron emission. This model was initially proposed as the generator of radio relics, but recent observation invalidated its use. It is still commonly used to explain the acceleration of “revived fossil plasma” in radio “phoenixes” (Enßlin and Gopal-Krishna, 2001; Brüggén et al., 2012).
- Secondary models: in these models, CR electrons are produced as secondary particles (decay products) and not because of in-situ acceleration. For example, in the hadronic model, collisions between relativistic protons and the thermal ions produce secondary CR electrons. Since CR protons have a very long lifetime ( $\sim 10^9$  yrs) compared to CR electrons, they will accumulate over the lifetime of a cluster once they are accelerated. Possible mechanisms to produce CR protons are first order Fermi acceleration at shocks, AGN activity, and galactic outflows (Dennison, 1980; Enßlin and Gopal-Krishna, 2001; Enßlin et al., 2011).
- Diffusive Shock Acceleration (DSA): also called First order Fermi acceleration, this process plays an important role in various astrophysical environments. Particles are accelerated at a shock with the acceleration taking place diffusively. In this process, particles cross back and forward across the shock front as they scatter from magnetic inhomogeneities in the shock down and upstream region. At each crossing, particles gain additional energy, forming a power-law energy distribution of CR (Blandford and Eichler, 1987). As this

process has been widely supported as the link between radio relics (see Chap. 2.2) and cluster merger shocks, a more in-depth description of this model is given in Chap. 2.2.1.

Significant work has been done in understanding the origin of this non-thermal emission in galaxy clusters. Secondary models have been invalidated by *Fermi* observations, which did not detect any  $\gamma$ -ray excess, predicted by hadronic collisions. Meanwhile, the acceleration of relativistic particles from the thermal pool in the ICM is not efficient enough to explain the observed radio luminosities in many objects (i.e. radio relics). As a consequence, studies are not focusing on re-acceleration models, proposing a turbulent acceleration for large scale, cluster-wide emission (radio halos), and shock re-acceleration for localized, extended radio sources (radio relics). Because of the synchrotron emission nature, cluster wide magnetic fields must be present in order to explain the extended emission component; observation constrained these fields to be in the order of  $0.1 - 10 \mu\text{Gauss}$  (van Weeren et al., 2019 and reference within).

In this work, we present the classification of diffuse radio emission proposed by van Weeren et al. (2019), dividing diffuse radio sources into two main classes: halos and relics.

## 2.1 Radio Halos

Radio halos are extended sources that follow the ICM gas density spatial distribution, located at the cluster center. They do not have any optical counterpart and are not localised, in the sense that particle (re-)acceleration occurs in a substantial portion of the cluster volume. According to present models, these sources should trace Fermi-II processes.

A sub-classification of radio halos can be made, based on their size and the properties of their host cluster (see Fig. 2.1).

The largest halos, called Giant radio halos, are Mpc-size radio halos (typical sizes of  $1 - 2 \text{ Mpc}$ ), mostly found in massive, dynamically disturbed clusters, with prototypical example being the Coma cluster (Willson, 1970). Their 1.4 GHz observed radio powers spans three order of magnitude, between  $10^{23}$  to  $10^{26} \text{ WHz}^{-1}$  and the emission is mostly unpolarized. The spectral properties of radio halos can provide important information about their origin, therefore, considerable amount of work has gone into measuring the spectral properties of halos (i.e. Botteon et al., 2018;

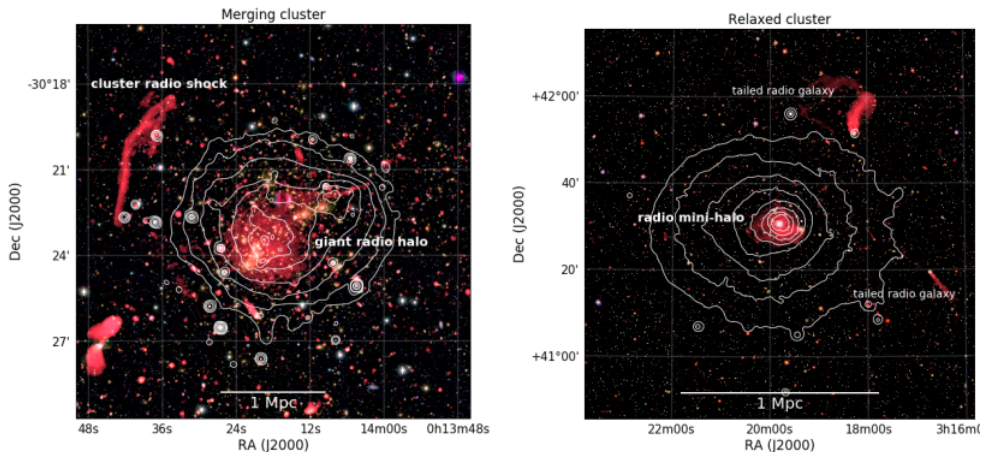


**Figure 2.1:** *Left panel:* VLA 1 – 4 GHz image of the merging galaxy cluster Abell 2744 with different source classes labeled (from Pearce et al., 2017). *Right panel:* VLA 230–470 MHz image of the relaxed cool core Perseus cluster from Gendron-Marsolais et al. (2017). XMM-Newton X-ray contours in the 0.4–1.3 keV band are overlaid in white with the same contour spacing as in the left panel.

Bonafede et al., 2018; Riseley et al., 2022). Most radio halos have integrated spectral indices in the range  $-1.4 < \alpha < -1.1$ . Secondary models of CRe production could explain radio halos emission, however they are not able to explain peculiar cases of steep radio halos ( $\alpha < -1.5$ ) and would imply  $\gamma$ -ray emission which is yet undetected. This specific kind of radio halos have been called ultra-steep spectrum radio halos (USSRH), which existence is expected if the integrated spectra of radio halos include a cut-off. Considering turbulent re-acceleration, the model predicts a break frequency which scales with the mass of the cluster ( $M \propto \nu^{4/3}$ ), implying that more sensitive observation at lower frequencies could reveal a higher number of USSRH (van Weeren et al., 2019 and reference within).

Diffuse emission is also present in non-merging, cool core clusters, namely radio mini-halos. This radio emission surrounds the central BCG, with sized of  $\sim 100\text{--}500$  kpc, comparable to the central cluster cooling regions. Although smaller than radio halos, radio mini-halos also require in-situ acceleration given the short lifetime of synchrotron emitting electrons. The radio emission from mini-halos does therefore not directly originate from the central AGN (van Weeren et al., 2019 and reference within). Their 1.4 GHz observed radio powers spans in the range of  $10^{23}$  to  $10^{25}$   $\text{WHz}^{-1}$  and, compared to giant radio halos, their synchrotron volume emissivities are generally higher. Spectral indices of radio mini-halos are similar to giant radio halos, although few detailed studies exist (Cassano et al., 2008). Radio emission from the BCG often makes their study difficult, as very high resolution and a high dynamic range are required.

## 2.2 Radio relics

Radio relics are extended diffuse sources, tracing particle (re-)acceleration due to ICM shock waves. They are an observationally defined class, of which our understanding is that in most cases they are linked to Fermi-I type acceleration. Even if both seem to generate from cluster mergers, radio relics seem to be less common than radio halos, as their observability might be biased by projection effects due to the merger angle or by the large timescales.

If we consider an idealized, head-on, binary merger we expect the presence of two sets of shocks: “equatorial” shocks forming first and moving outwards in the equatorial plane, and two “merger” shocks launch into opposite direction along the merger axis (see Fig. 2.2). Simulation showed how these shocks are mostly found in the outskirts of galaxy clusters, in agreement with observations (Vazza et al., 2012). In a collective study from Golovich et al. (2017), based on optical observations, they found that the merger axes of clusters hosting radio relics are near the plane of the sky, inducing selection biases for finding relics, based on the viewing angle. Most likely, many radio shocks are missed in observation due to this effect.

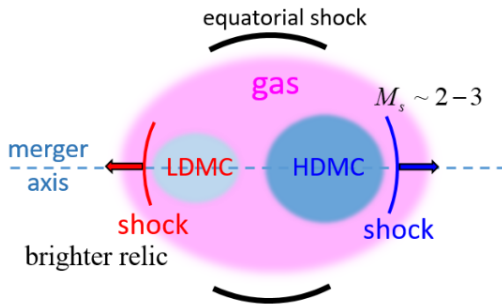


**Figure 2.2:** Schematic picture of an idealized, head-on, binary cluster merger about 1 Gyr after core passage. Equatorial shocks expand outwards in the equatorial plane perpendicular to the merger axis, while merger shocks launch in the opposite directions along the merger axis. The shock-kinetic-energy-weighted Mach number range is  $\langle M_s \rangle_\phi \simeq 2 - 3$ . Typically, the shock ahead of lighter DM core has the higher shock kinetic energy flux and becomes the brighter radio shock. From van Weeren et al. (2019)

Their shape is elongated and generally arc-shaped, as expected from sources tracing shocks, their sizes range between 0.5 – 2 Mpc, with brightness profile being higher on the side away from the cluster, and decreasing towards the center.

The integrated radio spectra of cluster radio relics display power-law shapes, with spectral indices ranging from about  $-1.0$  to  $-1.5$  and they often show a clear

gradient across their width, with the region with the flattest spectral index located on the outer side of the cluster, steepening towards the central regions (i.e. [van Weeren et al., 2010](#); [Rajpurohit et al., 2020](#)). This steepening is in agreement with synchrotron and IC losses in the shock downstream region, and the majority of single and double relics clusters show this behaviour ([van Weeren et al. \(2019\)](#) and reference therein).

Additionally, radio relics are among the most polarized sources in the sky, with polarization reaching up to  $\sim 60\%$ , higher in more elongated shocks.

The rarest of the relic phenomena are double relics that are equidistant from the cluster center, thought to form from a single merging event, providing two probes able to put tight constraints on the merger scenario.

As in the case of X-ray observations, radio emission can be used as a tool to estimate the Mach number of these shocks, starting from the assumptions of simple DSA theory, from the radio injection spectral index ( $\alpha_{inj}$ ), as

$$\mathcal{M}_{radio} = \sqrt{\frac{2\alpha_{inj} - 3}{2\alpha_{inj} + 1}}. \quad (2.5)$$

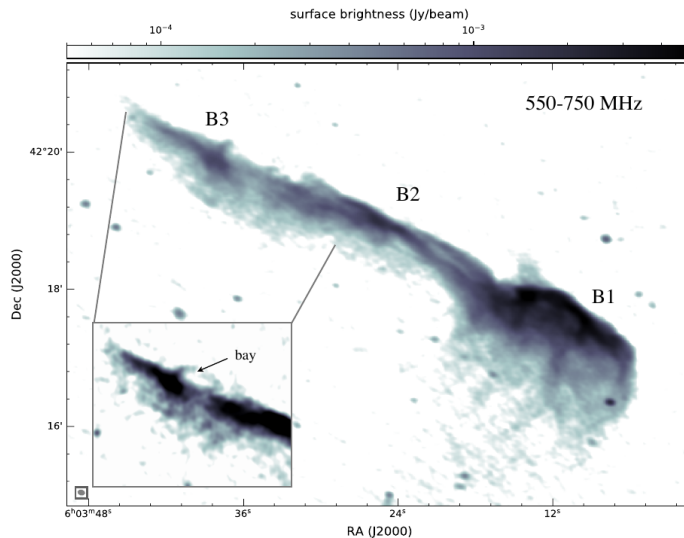


**Figure 2.3:** High resolution uGMRT image of the Toothbrush relic confirming the complex filamentary structures visible at 550-750 MHz. From [Rajpurohit et al. \(2020\)](#).

Typical Mach numbers associated with radio relics are in the units range (2 – 3) and they could be slightly higher than the hydrodynamical Mach number derived through X-ray analysis if there are Mach number variations in the shock front (due to radio luminosity strongly increasing with Mach number, i.e. [Hoeft](#)

and Brüggén, 2007). One of the most famous cases of radio relic is the so called “Toothbrush relic”, in the 1RXS J0603.3+4214 cluster (see Fig. 2.4). This well studied relic shows all of the characteristics described above, with a  $\sim 2$  Mpc size, together with a brightness profile and spectral index steepening towards the cluster center. As introduced in previous chapters, the presence of magnetic field is of fundamental importance in generating these diffuse emissions. Radio relics can be used to provide a measurement of the magnetic field in galaxy clusters. As an example, deep X-ray observations are able to provide lower-limits on the magnetic field that is generating a radio relic (Finoguenov et al., 2010; Itahana et al., 2015). Another method to constrain the magnetic field strength is to use the relic’s width, assuming it is determined by the characteristic timescale of electron energy losses and the downstream velocity. van Weeren et al. (2010) found values of  $\sim 1 - 5 \mu\text{G}$ , however, Rajpurohit et al. (2018) suggested that some external factors might influence the downstream radio brightness, for example, the presence of filamentary structures and a distribution of magnetic field strengths (see also Di Gennaro et al., 2018).

Filamentary structures have been found and studied in several radio relics, as progressively more are found with increasing resolution and signal-to-noise ratio (SNR), and their origin is still not fully known. One of the possibilities is for them to trace magnetic field variations due to the shock (Rajpurohit et al., 2020; Wittor et al., 2023).

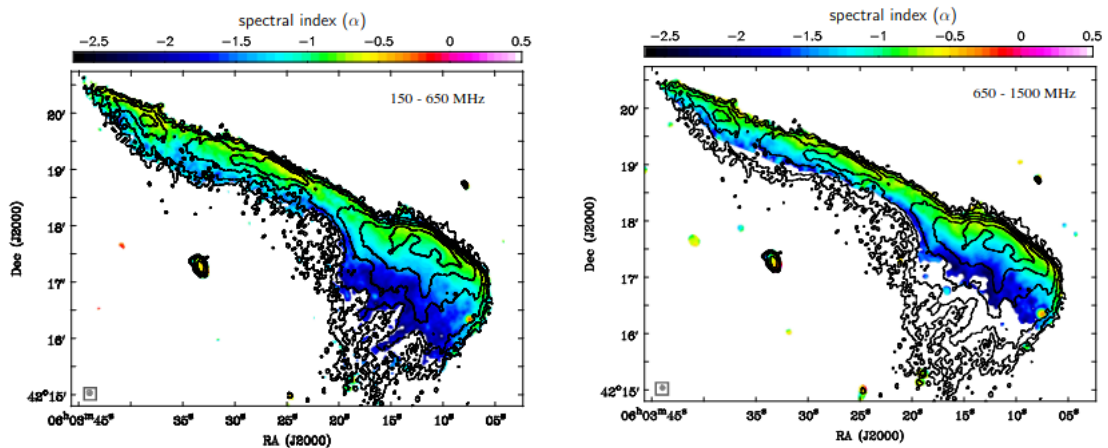


**Figure 2.4:** Spectral index maps of the Toothbrush, at  $5''.5$  resolution between 150 to 1500 MHz. The variations in the spectral index at the outer edge along the relic is clearly visible, reflecting inhomogeneities in the injection index. The color bar shows spectral index  $\alpha$  from  $-2.5$  to  $0.5$ . Contour levels are drawn at  $[1, 2, 4, 8, \dots] \times 4\sigma_{rms}$  and are from the 150 MHz LOFAR image. From Rajpurohit et al. (2020).

### 2.2.1 Diffusive Shock Acceleration as radio relic origin

Particle acceleration by shocks is conventionally described by the DSA theory. This process is based on the so-called Fermi-I mechanism (Fermi, 1949), which states that particles are scattered upstream and downstream of the shock by plasma irregularities, gaining energy at each reflection. Considering a flow defined by speeds  $u_1$  and  $u_2$  ( $< u_1$ ) on different sides of a shock (see Fig. 2.5), supposing that a particle of speed  $v_0$  starts in the upstream side of the shock ( $u_1$ ) and diffuse via “collisions” with the magnetized plasma, the particle will eventually cross the shock and enter the downstream region ( $u_2$ ). Such kind of collision tends to isotropize the angular distribution of the particles in the frame in which the upstream plasma is at rest. The particle now collides with magnetized plasma present in the downstream of the shock, moving toward the particle with speed  $\sim |u_1 - u_2|$ . The average momentum gain in a cycle (e.g. upstream to downstream and then back upstream again) for isotropic populations is

$$\langle \Delta p \rangle \approx \frac{4u_1(u_1 - u_2)p}{3u_2v}, \quad (2.6)$$

where  $p = mv$  is the momentum and  $v$  is the current particle speed. Thus, this “bouncing” between upstream and downstream regions guarantees a net increase in the average particle speed. Hence, the process is repeated, producing significant acceleration. For an in-depth description of the Fermi mechanism, see Baring (1997). As a result, radio emission in relics could be explained by thermal electrons accelerated by DSA.

The DSA theory was originally developed to explain shocks in supernova remnants (SNR), where strong shocks of Mach number  $\mathcal{M} \sim 10^3$  are able to accelerate cosmic ray protons (CRp), and a smaller fraction of cosmic ray electrons (CRE), with an efficiency of  $\eta \sim 10\%$  (Bell, 2014). In contrast, simulations on galaxy cluster mergers, and recent observations, have shown that the associated merger shocks have low Mach number (Vazza et al., 2019; Bykov et al., 2019 and reference therein) and are therefore in the weak-shock regime ( $\mathcal{M} < 5$ ). In this regime, the acceleration efficiency of CRp is much smaller (likely  $\eta < 1\%$ , see Fig. 2.6) and still poorly understood. This poses a challenge for DSA theory, which is not able to explain the large acceleration efficiencies needed to reproduce the total radio luminosity of several relics ( $\eta \sim 10\%$ ; see Botteon et al., 2020), assuming that particles are accelerated from thermal ICM. Moreover, the non-detection of expected  $\gamma$ -ray emission from galaxy clusters (Vazza and Brüggén, 2014, Wittor et al., 2017) cannot be

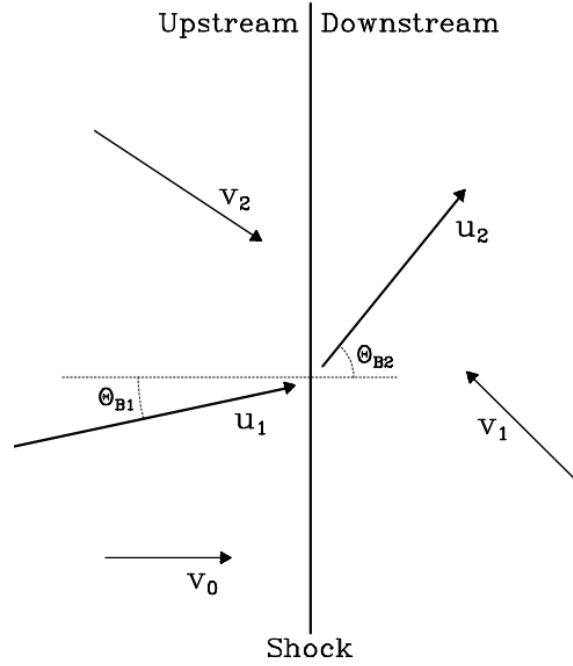


**Figure 2.5:** Schematic description of particle motion in the environment of a shock. The plasma flow speeds are  $u_1$  (upstream) and  $u_2$  (downstream), and the mean accelerated particle speeds are ordered according to  $v_0 < v_1 < v_2$ . Image from [Baring \(1997\)](#).

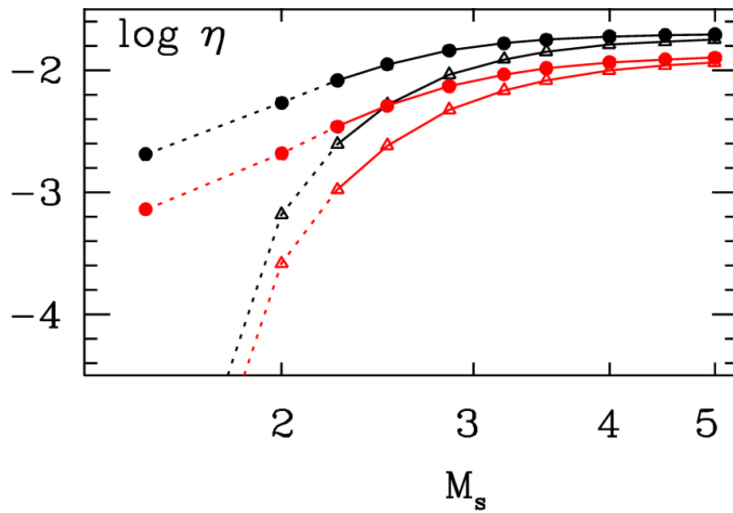


**Figure 2.6:** Cosmic-ray acceleration efficiency  $\eta$  as a function of Mach number. The red and black lines give the efficiencies for injection moments of  $p_{inj} = 3.5 \cdot p_{th}$  (red) and  $p_{inj} = 3.3 \cdot p_{th}$  (black), where  $p_{th}$  is the momentum of the thermal post-shock electrons. In this plot,  $M_S$  is the Mach number of the shock. From [Wittor, 2021](#).

explained even considering a high electron to proton acceleration fraction, as the resulting CRp acceleration should lead to  $\gamma$ -ray emission from inelastic collisions of secondary particles. Furthermore, different methods exist to calculate Mach numbers of radio relics, but they often bring to different results (see Chap. 6.2.1).

It is possible to overcome these issues by assuming a scenario in which radio relics are generated by the re-acceleration of pre-existing CRe at the merger shock, typically known as fossil plasma. This fossil plasma might be present due to ejecta from radio galaxies or prior shocks. These pre-existing high energetic particles can mitigate the minimum momentum requirement of DSA theory. Consequently, when a weak shock travels through a fossil plasma, DSA becomes more efficient ( $\sim 1\%$ ), and the resulting spectrum is similar to the flat spectrum of the seed electrons. In fact, if the fossil electron spectrum is a power law and is steeper than the one produced by the shock acceleration, the post-shock spectrum will acquire the slope of the shock. Instead, if the fossil electron spectrum is already flatter than the shock, the post-shock spectrum will retain its slope, but increase its normalization. This re-acceleration scenario is supported by several recent observations (Bonafede et al., 2014; Van Weeren et al., 2017; Rajpurohit et al., 2020). Although this mechanism mitigates the energetic problems of DSA, the CRp  $\gamma$ -ray problem is still unsolved, together with the origin of the re-accelerated fossil plasma.

# Chapter 3

## MACS J1752+4440

MACS J1752+4440 was first selected as part of the Massive Cluster Survey (MACS) carried out by [Ebeling et al. \(2001\)](#), which aimed at compiling a statistically complete cluster sample through the detection of X-ray emission coming from the hot ICM in the ROSAT All-Sky Survey (RASS, [Voges et al. \(1999\)](#)).

[Edge et al. \(2003\)](#) reported MACS J1752+4440 as a candidate for a double-relic galaxy cluster, with two moderately steep sources, 2 arcmin (corresponding to  $\sim 600$  kpc) either side from the cluster center.

A composed image of the galaxy cluster can be seen in [Fig. 3.1](#)

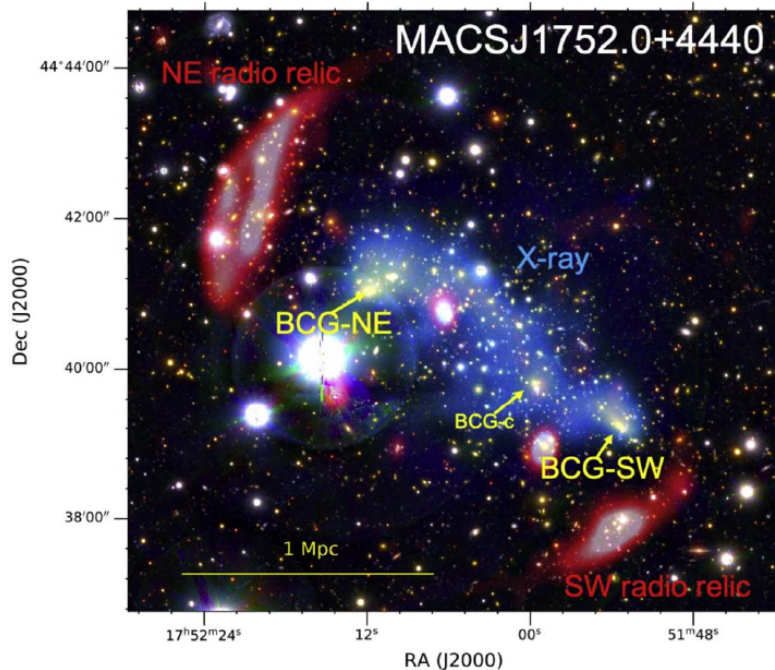


**Figure 3.1:** Image taken from Subaru, in *gri* color, of MACS1752 with 18 cm WSRT radio emission (red) from [van Weeren et al. \(2012\)](#) and 0.5 – 7 keV XMM-Newton X-ray emission (blue). Labels in yellow indicate radio cluster sources. From [Finner et al. \(2021\)](#).

van Weeren et al. (2012) studied this cluster through Westerbork Synthesis Radio Telescope (WSRT) L and S-band data (25, 21, 18 and 13 cm), together with archival B-array, L-band VLA data (1.4 GHz), observing two arc-like radio sources on opposite sides of the cluster center, identified as radio relics, plus a radio halo component.

Through the spectral analysis of the two radio relics, they fitted the integrated fluxes with two power-laws, with spectral indices  $\alpha_{NE} = -1.16 \pm 0.03$  and  $\alpha_{SW} = -1.10 \pm 0.05$  for the NE and SW relic, respectively. Using the assumptions from the DSA theory, they were able to find an injection spectral index of  $\alpha_{inj} \sim -0.6$  to  $-0.7$  which corresponds to a Mach number of  $3.5 - 4.5$ .

A further analysis was carried out by Bonafede et al. (2012) using GMRT (323 MHz), WSRT (25, 21, 18 and 13 cm) and VLA C-array (1.7 GHz) archival data to produce spectral index images of the cluster with a resolution of  $\sim 24'' \times 10''$ , highlighting the trends of the spectral index throughout the relics transversal axis.

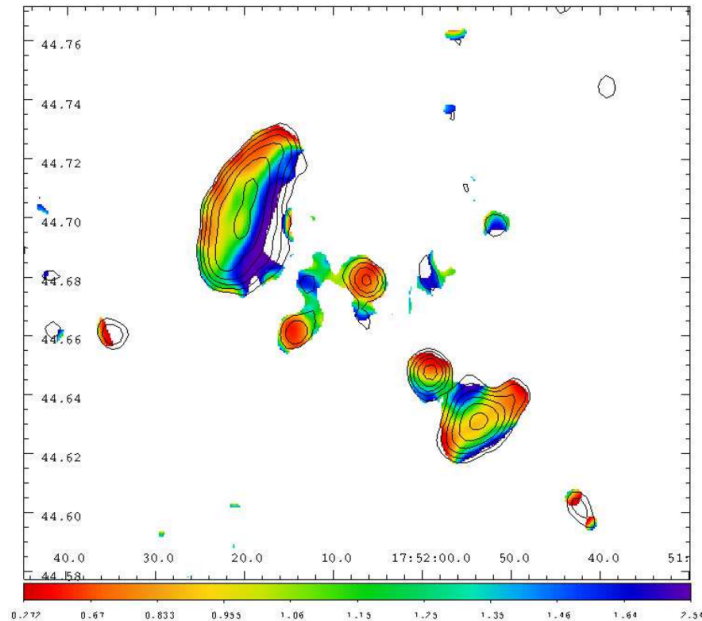


**Figure 3.2:** Spectral index map overlaid with GMRT (323 MHz) contours. The image was produced with a  $24'' \times 10''$  beam. From Bonafede et al. (2012).

In particular, as it can be seen in Fig. 3.2, the NE relic showed a clear steepening of the spectral index going from the cluster periphery toward the centre, while the SW relic showed a more complex gradient along the relics' main axis. In addition, the flattest spectral index of the SW relic is not located at the edge of the emission, but more central, which could be explained with emission observed at a slight angle with respect to the observer.

Golovich et al. (2019) studied the merging scenario of the cluster through XMM-Newton X-ray observations, highlighting the presence of two “bullets” initiating a counterclockwise orbit. The brightness of the two relics suggests a major merger, and the velocity dispersion of the two subclusters suggests a perpendicular orbital plane to the line of sight. Furthermore, the survival of the two cores suggests a non-zero impact parameter. A visualization of the scenario can be seen in Fig. 3.3.

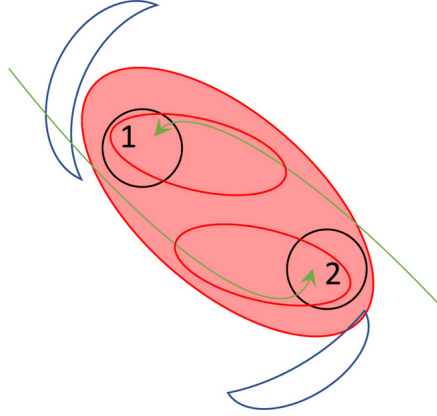


**Figure 3.3:** Possible merger scenario. The two subclusters generated a major merger, which produced two radio relics along the merger axis and a radio halo throughout the cluster. From Golovich et al. (2019).

Finner et al. (2021) conducted a weak-lensing and X-ray analysis of MACS J1752+4440. Through weak-lensing they estimate the total mass of the cluster at  $M_{200} = 14.7^{+3.8}_{-3.3} \times 10^{14} M_{\odot}$  and a dynamic of the cluster merger as an head-on collision with approximately 1:1 mass ratio, in agreement with Golovich et al. (2019). Through XMM-Newton, they attempted to detect the shock in the X-ray emission from the ICM. They produced the two surface brightness profiles, guided by the position of the two radio relics, as seen in Fig. 3.4. They detect two surface brightness drop, which are located in between the edge of the subclusters and the position of the relics, and are therefore interpreted as cold fronts.

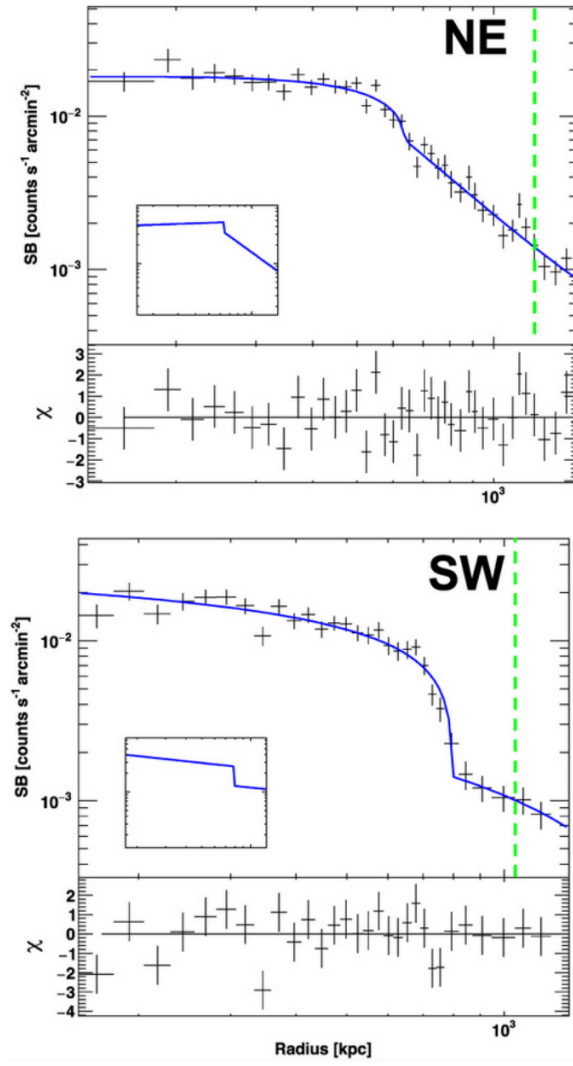


**Figure 3.4:** *Top:* X-ray surface brightness profile for the NE core. *Bottom:* X-ray surface brightness profile for the SW core. The position of the radio relic is indicated by the green dashed line.

### 3.1 This thesis

In this thesis work we use new uGMRT and JVLA observation, combined with LO-FAR public data, to perform a resolved spectral study of the double-relics galaxy cluster MACS J1752+4440. The aim of this study is to constrain the parameters of the two radio relics, observing and characterizing their substructures (Chap. 5.3). We also perform a curvature study by producing the spectral curvature map and color-color plots (Chap. 6.4), to compare with synchrotron aging models. A polarization study is produced to hint at the presence of projection effects and explain the observed substructures (Chap. 6.5). At last, we calculate the equipartition magnetic field from both radio relics (Chap. 6.6).

Throughout this work, we assume a concordance cosmological model  $\Lambda$ CDM, with  $H_0 = 72 \text{ km s}^{-1} \text{ Mpc}^{-1}$ ,  $\Omega_M = 0.27$ , and  $\Omega_\Lambda = 0.73$ .

# Chapter 4

## Observing in the Radio band

The field of radio astronomy focuses on examining the radio signals emitted by celestial objects. The range of radio frequencies and wavelengths that can be detected is limited by atmospheric opacity and quantum noise in coherent amplifiers. Typically, the boundary between radio and far-infrared astronomy is situated at a frequency of approximately 1 THz, while the Earth's ionosphere acts as a barrier for low-frequency ground-based radio astronomy, reflecting extraterrestrial radio waves with frequencies below 10 MHz, but affecting observations at  $\nu \leq 1$  GHz. Observations from the ground are limited to optical/near-IR and radio wavelengths due to the Earth's atmosphere absorbing electromagnetic radiation in most infrared, ultraviolet, X-ray, and gamma-ray wavelengths. Because the radio window

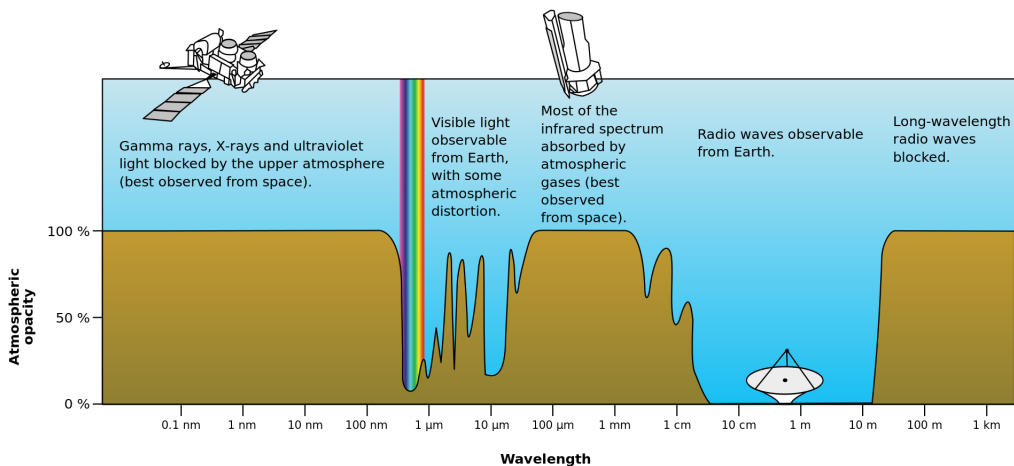


**Figure 4.1:** Plot of Earth's atmospheric opacity to various wavelengths of electromagnetic radiation. This is the surface-to-space opacity, the atmosphere is transparent to longwave radio transmissions within the troposphere but opaque to space due to the ionosphere. Credits: NASA

is so broad almost all types of astronomical sources, thermal and non-thermal

radiation mechanisms, and propagation phenomena can be observed at radio wavelength; and a wide variety of radio telescopes and observing techniques are needed to cover the radio window effectively.

Radio telescopes are receiving antennas that can be described as passive devices that convert electromagnetic radiation into electrical currents in conductors. They must have very large aperture diameters  $D$  to achieve good diffraction-limited angular resolution  $\theta \approx \lambda/D$  radians (Condon and Ransom (2016)).

A useful parameter for radio antennas is the *effective area*, defined considering an antenna whose output spectral power is  $P_\nu$  in response to an unpolarised point source of total flux density  $S_\nu$

$$A_e \equiv \frac{2P_\nu}{S_\nu}, \quad (4.1)$$

representing the antenna response to incoming radiation. This parameter can be averaged over a solid angle  $\Omega$  as

$$\langle A_e \rangle = \frac{1}{4\pi} \int_{4\pi} A_e d\Omega. \quad (4.2)$$

It can be demonstrated (Condon and Ransom (2016)) that, considering  $\lambda$  the observing wavelength:

$$\langle A_e \rangle = \frac{\lambda^2}{4\pi}. \quad (4.3)$$

It is possible to connect the effective area of a telescope to its *beam solid angle*  $\Omega_A$ , which is the angle under which an antenna receives most of its power, through the equation:

$$\Omega_A = \frac{\lambda^2}{A_0}, \quad (4.4)$$

where  $A_0$  is the maximum effective collecting area. This shows us that the higher the effective area, the smaller the beam solid angle.

## 4.1 Single dish radio telescopes and interferometry

The most common shape for radio telescopes is a paraboloid of revolution, as it can focus the plane wave from a distant point onto a single focal point, in which the feed antenna is positioned. However, the radio band is too vast to be effectively covered by a single telescope design alone, so many other designs are utilised at

different frequencies (i.e. LOFAR, [van Haarlem et al. \(2013\)](#)). A brief discussion of the utilised telescope will be given in the following chapters.

The main limitation of single dish telescopes is given by their variation of instrumental response with the angle, also called *power pattern* (Fig. 4.2). This pattern is represented by the diffraction figure of a point source and is divided into different sections, in which the most important one is the central region, called main beam. The angular size of the main beam is what sets the resolution limit of a telescope of diameter  $D$  and is commonly referred to as *half-power beamwidth* (HPBW):

$$\theta_{HPBW} \sim \frac{\lambda}{D}. \quad (4.5)$$

As the resolution depends on the diameter, increasing the resolution for single

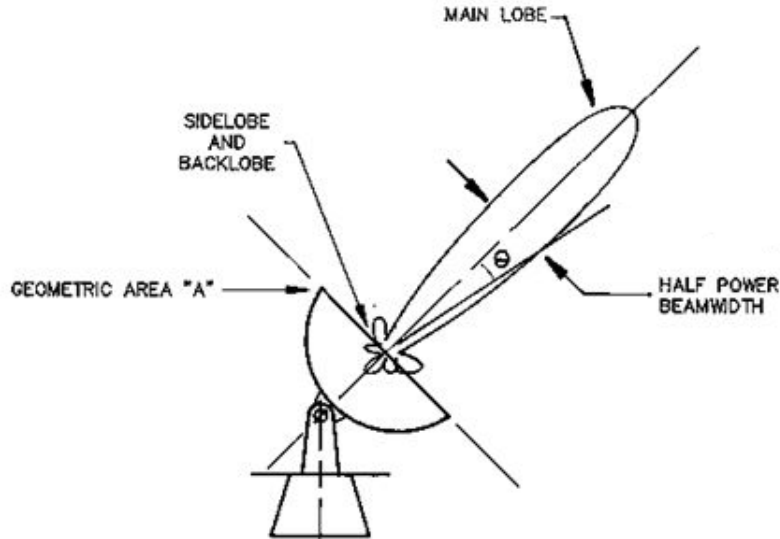


**Figure 4.2:** Example of power pattern, highlighting the presence of a main lobe and minor lobes called side lobes.

dish telescopes becomes challenging as  $\sim 100$  m antennas are highly unpractical. To atone for this problem, interferometry has been widely used and developed to combine different single dish radio antennas into multi-element arrays.

The use of aperture-synthesis interferometers, which include  $N \geq 2$  moderately small dishes, has addressed several practical issues linked to single dishes. These problems include susceptibility to changes in atmospheric emission and receiver gain, radio-frequency interference, and shifts in pointing caused by atmospheric refraction. A basic radio interferometer is a combination of two radio telescopes that correlate (multiply and average) their voltage outputs. Even the most sophisticated interferometers, consisting of  $N \gg 2$  antennas, can be viewed as  $N(N - 1)/2$  inde-

pendent two-element interferometers (Condon and Ransom (2016)). Considering,

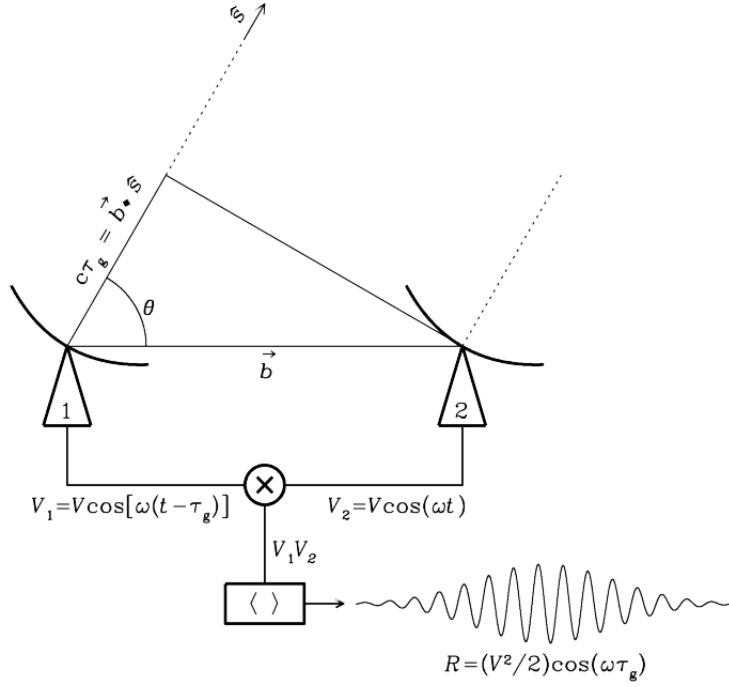


**Figure 4.3:** Diagram showing the components of a two-element interferometer, where  $\hat{s}$  is the unit vector in direction of a distant point source,  $\vec{b}$  is the separation between antennas called *baseline vector*,  $V_1$  and  $V_2$  the two output voltages, where  $V_1$  is delayed by the geometric delay  $\tau_g$ . From Condon and Ransom (2016)

for simplicity, a two element interferometer like the one in Fig. 4.3, the geometric delay can be written as the product between the baseline vector  $\vec{b}$  and the unit vector in the direction of the source  $\hat{s}$ :

$$\tau_g = \frac{\vec{b} \cdot \hat{s}}{c} \quad (4.6)$$

The output voltages of antennas 1 and 2 can be written a

$$V_1 = V \cos[\omega(t - \tau_g)] \quad \text{and} \quad V_2 = V \cos[\omega t]. \quad (4.7)$$

These two voltages are fed to a *correlator*, which multiplies the two voltages and averages them over time to obtain the *correlator response*, which defines the *fringe pattern*

$$R = \langle V_1 V_2 \rangle = \left( \frac{V^2}{2} \right) \cos(\omega \tau_g). \quad (4.8)$$

Combining the response from both cosine and sine correlators it is possible to obtain complex functions called *visibilities*, Fourier transform of the Sky Brightness  $I_\nu$

$$\mathcal{V}_\nu(u, v, w) = \int \int \frac{I_\nu(l, m)}{(1 - l^2 - m^2)^{1/2}} \exp[-i2\pi(ul + vm + wn)] dldm \quad (4.9)$$

where  $(u, v, w)$  is a coordinate system used to describe any baseline vector  $\vec{b}$  in three dimension and  $l, m$  are the cosine sky coordinates, obtained from  $\hat{s}$ . In case of small field of view (FoV) the  $w$  component can be neglected and the visibility becomes a simple two-dimensional Fourier transform, while for higher FoV (i.e. lower frequencies) other techniques have been developed (See Chap. 4.2).

In a more realistic case, visibilities can be written as

$$\mathcal{V}^{ij} = A^{ij} e^{-i\phi^{ij}} \quad (4.10)$$

where  $A^{ij}$  is the visibility amplitude and  $\phi^{ij}$  is the visibility phase, written considering a single pair of antennas  $(i, j)$ . The actual source visibilities are corrupted by many factors while reaching the receiver

$$\mathcal{V}_{obs}^{ij} = G^{ij} \cdot \mathcal{V}_{true}^{ij} \quad (4.11)$$

where  $G^{ij}$  are called *complex gains*. Equation 4.11 is called *Measurement Equation* and the process of correcting the observed visibilities by the effect of the complex gains is called *calibration*. The causes for these corruptions can be of various kind: phase fluctuations due to the effect of the atmosphere, acting at all frequencies, amplitude variation due to the electronics of the instrument, etc.

Following the calibration process, visibilities can be Fourier transformed to obtain the sky brightness distribution. Assuming a small FoV (hence  $w = 0$ , as described above), the imaging process follows a simple 2D Fourier transform described by the equation

$$I_\nu(l, m) = \int \int \mathcal{V}_\nu(u, v) \exp[i2\pi(ul + vm)] dldm. \quad (4.12)$$

The observed  $\mathcal{V}_\nu(u, v)$  are a discrete set of points, sampled in certain points of the  $(u, v)$  plane. Therefore, the observed visibilities are not the theoretical continuous function, but a product of the true visibilities  $\mathcal{V}_\nu$  and the *sampling function*  $S_\nu(u, v)$ , which dictates in which points of the  $(u, v)$  plane we are selecting the visibilities. The Fourier transform of the product  $\mathcal{V}_\nu(u, v)S_\nu(u, v)$  is called the *dirty image*

$$I_\nu^D(l, m) = \int \int \mathcal{V}_\nu(u, v) S_\nu(u, v) \exp[i2\pi(ul + vm)] dl dm \quad (4.13)$$

which is represented by the sky brightness distribution multiplied for the *dirty beam*  $B_D$  (point spread function of the image)

$$I_D = I \cdot B_D. \quad (4.14)$$

The dirty beam is the Fourier transform of the sampling function

$$B = \int \int S(u, v) \exp[i2\pi(ul + vm)] dudv. \quad (4.15)$$

thus, to obtain the real sky brightness distribution, one need to deconvolve the dirty image by the instrumental response.

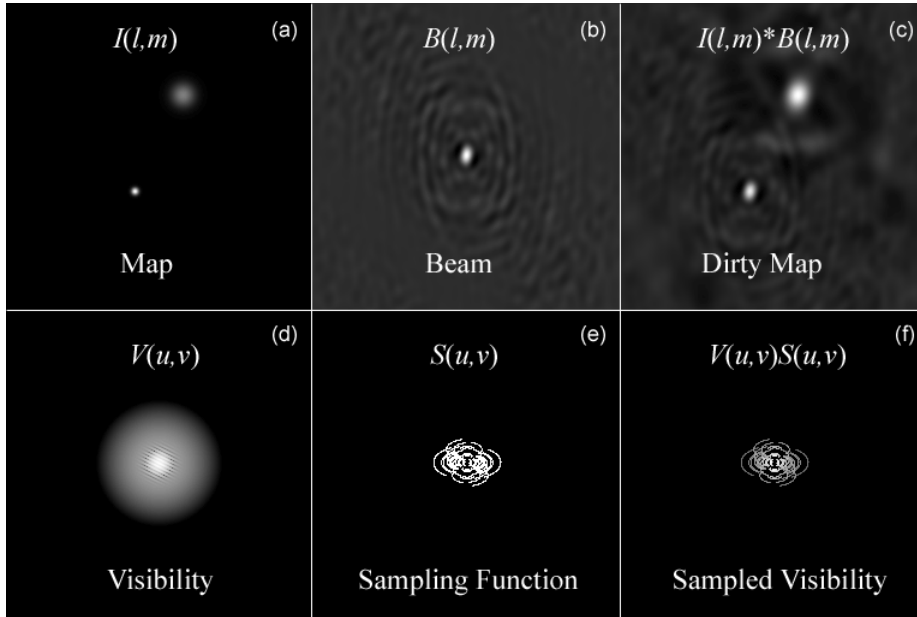


**Figure 4.4:** a) An example (model) sky map. d) The corresponding visibilities (Fourier Transform of the map). c) The synthesized beam, or point-spread-function, of a model antenna array. e) The sampling function of the array, whose Fourier Transform gives the beam in (b). f) The product of panels (d) and (e), representing the sampled visibilities. These are the actual measurements from the array. c) The dirty map that results from the Fourier Transform of the sampled visibilities. This is the same as the convolution of the map in (a) and the synthesized beam in (b). From: NJIT lecture 6

Deconvolving refers to the process of reconstructing a model of the sky brightness distribution, given a dirty image and the PSF of the instrument. There are several deconvolution algorithms based on the CLEAN algorithm from Högbom (1974),

which starts from the assumption that the sky brightness  $I(l, m)$  can be considered as an ensemble of point sources. The algorithm searches in the dirty image for the highest brightness pixel  $I_{max}$  and copies it into a model image  $I^M$ , applying the PSF and scaling it by a factor called the *loop gain*  $\gamma \sim 0.1 - 0.2$ . The algorithms then subtracts from the dirty image the saved pixel, with the PSF applied. This process is iterated, subtracting peaks of intensity from the dirty image until a threshold is reached. The end products of the CLEAN algorithm are the model image  $I^M$  containing all the removed peaks and the residual image  $I^R$  containing what is left of the dirty image. A visual representation of the various components can be seen in Fig. 4.4. The final step of the algorithm is called the *restoring* process, in which each point of the model image is convolved with the *clean beam*, which is a gaussian function with the same Full Width at Half Maximum (FWHM) of the dirty beam, and then added with the residual image to produce the final image.

## 4.2 WSCLEAN

As described in sec. 4.1, in the case of small FoV the  $w$  component of the visibilities can be approximated to zero. However, when the field of view is sufficiently large, this approximation is no longer valid and the three-dimensional nature of the sky brightness distribution needs to be accounted for. In this thesis, we will describe the  $w$ -stacking technique implemented in the WSClean software package (Offringa et al. (2014)).

To derive this technique, the first step is to rewrite Eq. 4.9 as an ordinary two-dimensional Fourier transform

$$\mathcal{V}(u, v, w) = \int \int \frac{I(l, m) e^{-i2\pi w(\sqrt{1-l^2-m^2}-1)}}{\sqrt{1-l^2-m^2}} \times e^{-i2\pi(ul+vm)} dl dm \quad (4.16)$$

which can then be inverted to get

$$\frac{I(l, m)}{\sqrt{1-l^2-m^2}} = e^{i2\pi w(\sqrt{1-l^2-m^2}-1)} \int \int \mathcal{V}(u, v, w) \times e^{i2\pi(ul+vm)} dudv \quad (4.17)$$

This equation is then integrated on both sides between  $w_{min}$  and  $w_{max}$  (the minimum and maximum value of  $w$ ) in order to reconstruct the sky brightness distribu-

tion in every direction

$$\frac{I(l, m)(w_{max} - w_{min})}{\sqrt{1 - l^2 - m^2}} = \int_{w_{min}}^{w_{max}} dw e^{i2\pi w(\sqrt{1-l^2-m^2}-1)} \int \int \mathcal{V}(u, v, w) \times e^{i2\pi(ul+vm)} dudv \quad (4.18)$$

Finally, the  $(u, v, w)$  parameters are discretised, so that the integration over  $u$  and  $v$  become an inverse Fourier transform and the integral on  $w$  becomes a sum. To resume the basic principle of the  $w$ -stacking, it calculates the 2D Fourier transform for fixed  $w$  values and then sums over all of the possible  $w$ . In this way,  $I(l, m)$  is easily recovered and the correction for large FoVs is applied.

In this work, the imaging process was carried out using WSCLEAN version 3.1.

# Chapter 5

## Data reduction and imaging of MACS J1752+4440

In this thesis work, we studied MACS J1752+4440, focusing on its double relic system and its spectral properties. We started from calibrated radio observations obtained from LOFAR (120 – 168 MHz), new uGMRT band 3 (300 – 500 MHz) and band 4 (550 – 850 MHz) and JVLA band L (1 – 2 GHz).

In this Chapter, we will describe the data reduction and imaging procedure. A summary of the produced images parameters is reported in Tab. 5.1.

### 5.1 Observations and data reduction

#### 5.1.1 LOFAR

MACSJ 1752+4440 was observed in three pointings (P265+45, P269+43, P269+45) of the LOw Frequency ARray (LOFAR) Two-meter Sky Survey (LoTSS; [Shimwell et al., 2017](#); [Shimwell et al., 2019](#); [Shimwell et al., 2022](#)), an ongoing deep imaging survey at 120 – 168 MHz that aims to cover the whole northern sky. The survey has a nominal sensitivity of  $0.1 \text{ mJy beam}^{-1}$  at a  $6''$  resolution. Each pointing observed the target using LOFAR High Band Antennas (HBA) in the 120 – 168 MHz frequency range, with a total time of eight hours per pointing, book-ended by ten-minute calibrator scans.

We use data from the Second LoTSS Data Release (LoTSS-DR2; [Shimwell et al., 2022](#)), which provides additional improvements to image fidelity, particularly for faint diffuse structures. MACS J1752+4440 is part of the second Planck catalog of Sunyaev-Zeldovich sources (namely PSZ2 G071.21+28.86; [Planck Collaboration](#)

et al., 2016), presented by Botteon et al. (2022).

The calibration of LOFAR data was executed by the survey team, by processing each of the three individual pointings with the pipelines developed by the LOFAR Survey Key Science Project. This first calibration aims to correct for both direction-independent and direction-dependent effects, producing  $\sim 6''$  resolution images of the entire LOFAR FoV, with  $\sim 0.1 \text{ mJy beam}^{-1}$  noise levels (Shimwell et al., 2019; Tasse et al., 2021). Moreover, in order to further improve the image quality toward the target, the team adopted the “extraction + recalibration” scheme described by van Weeren et al. (2021), which consists of the subtraction of the sources outside a small square region of the sky (in this case,  $25' \times 25'$ ) containing the target, from the uv data. These data sets are then phase-shifted to the center of the region, averaged in time and frequency and corrected for the LOFAR primary beam in that direction. Then, the calibration of the data is refined by performing a series of phase and amplitude calibration loops and, finally, the extracted data are self-calibrated.

Starting from already calibrated data, we jointly imaged the three observations using WSCLEAN v3.1 (Offringa et al., 2014) with the “wideband deconvolution” algorithm. We produced images at different resolutions, centered at 144 MHz, using the multiscale and multifrequency synthesis deconvolution scheme described by Offringa and Smirnov (2017), dividing the band into six 8 MHz channels. Using two different sets of parameters, we derived final images at two different resolutions. In particular, to obtain the high-resolution image ( $4.8'' \times 3.2''$ ) we imaged the data using the Briggs weighting scheme, (Briggs, 1995) with ROBUST =  $-1$ , while for low-resolution images ( $13.4'' \times 6.8''$ ) we used a ROBUST =  $+0.25$  and a Gaussian taper with TAPER =  $10''$ .

To avoid the cleaning of calibration artifacts, we applied an external mask that selects whether a pixel is considered or not during the deconvolution process. We generated external masks at the two different resolutions using images with shallow deconvolution (fewer iterations) using the BREIZORRO<sup>1</sup> tool, which creates a binary image assigning a value of 1 to every pixel brighter than  $n\sigma_{rms}$ , where  $\sigma_{rms}$  is the noise level, and values of 0 elsewhere. After testing different thresholds, we concluded that the ideal masks were generated adopting a  $4\sigma_{rms}$  and  $6\sigma_{rms}$  threshold

---

<sup>1</sup><https://github.com/ratt-ru/breizorro>

for high and low-resolution, respectively.

The LOFAR flux density scale (LoTSS; [Scaife and Heald, 2012](#)) show systematic offsets ([Hardcastle et al., 2016](#)), which can be corrected by applying an observation specific correction factor, as described in [Shimwell et al. \(2022\)](#). This correction factor — calculated by [Botteon et al. \(2022\)](#) — was computed by cross-matching the LOFAR data with known surveys (NVSS [Condon et al., 1998](#); 6C catalog [Hales et al., 1990](#)), comparing the LOFAR flux densities with catalogs of sources detected in all surveys to derive the scaling factors. For these observations, a multiplicative correction factor of 0.86 was applied to the produced LOFAR images, using the task `IMMATH` in the Common Astronomy Software Applications (`CASA`) package.

### 5.1.2 uGMRT

[van Weeren et al. \(2012\)](#) and [Bonafede et al. \(2012\)](#) studied MACS J1752+4440 using the “old” GMRT, which was later on updated to the upgraded Giant Metre-wave Radio Telescope (uGMRT). The major upgrade of the observatory increased its sensitivity by up to three times by increasing its wide-band capabilities from 50 to 1500 MHz ([Gupta et al., 2017](#)).

MACS J1752+4440 was observed, in June 2021, in band 3 (300 – 500 MHz) and band 4 (550 – 750 MHz) for a total of 5 hours, book-ended by ten-minute calibrator scans, as part of an observing campaign dedicated to the follow-up of double radio relics detected in PSZ2 in LoTSS-DR2 (Project code: 40\_025; PI: A. Botteon), employing the [Scaife and Heald \(2012\)](#) flux density scale. The dataset from band 3 was split into six frequency slices, with a total bandwidth of 200 MHz, while band 4 was split into four 50 MHz slices. Firstly, these slices were independently processed using the Source Peeling and Atmospheric Modeling (SPAM; [Intema et al., 2009](#)) pipeline, which measures the ionospheric phase errors toward the strongest sources in the field of view, allowing to derive direction-dependent gains and fitting a phase screen over the entire field of view.

Following a similar process as described in the LOFAR section, starting from pre-calibrated data, we jointly deconvolved the six slices of uGMRT band 3 data with a central frequency of 416 MHz and created high and low-resolution images. The lowest frequency slice was removed as it degraded the image quality due to high noise, reducing the overall S/N ratio. This is a known issue at the GMRT site that is likely due to the radio frequency interference (RFI) effect, which typically affects the lower frequency part of the band. Therefore, the imaging was carried out

employing the multiscale/multifrequency scheme, on five out of six slices of 33 MHz each (for a total band of 167 MHz), using the Briggs weighting scheme, with `ROBUST` =  $-1$  for the high-resolution image ( $5.1'' \times 4.3''$ ) and `ROBUST` =  $+0.25$  together with a Gaussian taper of `TAPER` =  $10''$  for the low-resolution image ( $14.6'' \times 11.4''$ ). The same procedure was followed for the four slices of uGMRT band 4 data, centered on 650 MHz. External masks were produced using the same scheme as in the LOFAR case, with a threshold of  $4\sigma_{rms}$ .

uGMRT data needs to be corrected by the effect of the primary beam, which mimics the PSF response of the instrument in the observed data. To apply the primary beam correction, data from both bands needed to be divided by their respective primary beam images. We applied such correction by generating the primary beam image through the `TCLEAN` tasks in `CASA`, by running a shallow deconvolution process with few iterations, and then dividing the produced image by the primary beam image through the `IMMATH` task in `CASA`.

### 5.1.3 JVLA

The JVLA observations of MACS J1752+4440 were carried out in the JVLA L band ( $1 - 2$  GHz) in three different configurations: D, C and B, respectively in December 2011, February 2012 and June 2012, for a total of 15 hours, book-ended by ten-minute calibrators scans, employing the [Perley and Butler \(2013\)](#) flux density scale. Each observation was executed using eleven spectral windows — divided in 64 channels each — and in full polarization, for a final bandwidth of 600 MHz, reduced from the nominal band due to flagging. All four polarizations (RR, RL, LR and LL) were recorded. The data were pre-calibrated performing a self-calibration in `CASA`, flagging through `AOFlagger` and proceeding with the standard flux and bandpass calibration. Data/Observations were corrected for the polarization leakage using a phase calibrator, observed for a wide parallactic-angle range. Finally, the polarization angle offset was corrected using a polarized calibrator (3C286). A self-calibration process was attempted, without increasing the quality of the images. As a result, data was not self-calibrated.

As for the previous cases, images were produced following a multi-scale/multifrequency scheme, joining the three different configurations in the same deconvolution process, dividing the band in 6 channels of 93 MHz each, using a Briggs weighting scheme with `ROBUST` =  $-0.5$  for the high-resolution image, together with a Gaussian taper of `TAPER` =  $15''$  for the low-resolution image. Ex-

**Table 5.1:** Observations and imaging parameters.

	LOFAR	uGMRT Band 3	uGMRT Band 4	JVLA
Bandwidth, # chan. per sub-band	48 MHz, 1	200 MHz, 31	200 MHz, 32	1 GHz, 54
Observation dates	June 16, 2019	June 14, 2021	August 1, 2021	June 19, 2012
Total on-source time	8 hr	5 hr	5 hr	15 hr
Beam size	4.9" $\times$ 3.2", 13.4" $\times$ 6.8"	5.1" $\times$ 4.3", 14.6" $\times$ 11.4"	3.3" $\times$ 2.6", 13.0" $\times$ 12.2"	5.0" $\times$ 4.6", 14.8" $\times$ 14.5"
Rms noise ( $\sigma_{rms}$ )	280 $\mu$ Jy beam <sup>-1</sup> , 350 $\mu$ Jy beam <sup>-1</sup>	70 $\mu$ Jy beam <sup>-1</sup> , 138 $\mu$ Jy beam <sup>-1</sup>	23 $\mu$ Jy beam <sup>-1</sup> , 50 $\mu$ Jy beam <sup>-1</sup>	15 $\mu$ Jy beam <sup>-1</sup> , 50 $\mu$ Jy beam <sup>-1</sup>
Robust weighting	-1, +0.25	-1, +0.25	-1, +0.25	-0.25

ternal masks were produced using the same scheme as in the LOFAR case, with a threshold of  $4\sigma_{rms}$ .

The polarization images were produced by using the polarimetric deconvolution scheme of `WSClean`, which, similarly to the wideband deconvolution scheme, creates a single image for each Stokes parameter (I, Q, U, V) together with the final Stokes I, Q, U, and V images. Additionally, the polarimetric deconvolution scheme was used, which, like for the wideband deconvolution scheme case, implies that peak finding is performed in the integrated values over the selected polarizations, but the components strengths are determined from each polarization individually. The same external masks, generated on the Stokes I image, were applied also in this procedure.

## 5.2 Imaging

As the spectral analysis depends on comparison between images at different frequencies, it is of fundamental importance that images obtained from different interferometers sample the same range of angular scales. Each instrument has a different shortest, well sampled baseline. In our case, the minimum common baseline was defined by the uGMRT band 4 observation, with a minimum *uv-cut* of  $150\lambda$ . Since LOFAR and JVLA both comprehended smaller baselines, we imaged our data with a common lower *uv-cut* at  $150\lambda$ . This ensures that we are comparing images in a self-consistent manner.

A known effect present in radio astronomy is a small misalignment ( $\lesssim 1''$ ) between sources in the sky in images at different frequencies, introduced by the self-calibration and the deconvolution processes. To correct for this effect, which would generate spurious trends in the spectral maps, we performed an alignment of the images, using the LOFAR image as a reference template. Using *CASA*, we measured the offset between the peak flux of five point sources, spread across the images, by performing a Gaussian fit for each point source. The average shift of the peak flux of the five selected sources allowed us to obtain the correction for said offset ( $\sim 1 \pm 0.1$  pixel in the x and y direction, corresponding to  $1.5''$ ), which was applied shifting the position of the reference pixel of uGMRT and JVLA images through the *IMHEAD* task in *CASA*.

To ensure that each pixel corresponds to the same region in the sky we forced each image to the same pixel size, choosing LOFAR high and low-resolution images as a reference, by regridding the uGMRT and JVLA images with the *IMREGRID* task in *CASA*.

At last, to proceed with the spectral analysis, LOFAR, uGMRT and JVLA high and low-resolution images needed to have the same restoring beam. This was ensured by using the *IMSMOOTH* task in *CASA*, generating images with the same beam size of  $7'' \times 7''$  for high-resolution and  $20'' \times 20''$  for low-resolution.

This procedure allowed us to conduct the spectral analysis, starting from images at different frequencies with identical pixelation, a common minimum *uv-cut*, the same restoring beam and correction for positional offsets.

### 5.3 Radio Images

We produced deep radio continuum images at different resolutions. In Fig. 5.1, we show the highest resolution image we obtained from uGMRT band 4 data at  $3.3'' \times 2.6''$ , the highest level of detail ever achieved for this cluster. In addition, to perform the spectral analysis, we produced images with a common high-resolution of  $7'' \times 7''$  and common low-resolution of  $20'' \times 20''$ . In Fig. 5.2 and 5.3, we show the resulting images for LOFAR 144 MHz, uGMRT 416 MHz, uGMRT 650 MHz and JVLA 1.6 GHz in both high and low-resolution.

We detect two radio relics, respectively North East (NE) and South West (SW) of the cluster center, and a faint radio halo component, better observed in the low-resolution images, which is not considered in this work. Fig. 5.1 shows how the high resolution made it possible to clearly distinguish substructures along the NE relic main axis, resembling a double shock front. We divide the NE relic into three components: an “outer edge” at the expected position of the shock that generated the relic, a “bright bar” in the middle of the relic and the downstream region.

The same components are also visible in Fig. 5.2 from the high-resolution ( $7''$ ) images, in each band, generated for the spectral analysis. The two radio relics have a similar extension and morphology throughout the frequency band.

On the other hand, low-resolution images enhance the sensitivity of extended emission, showing a more extended downstream region for both radio relics, but missing the separation between the substructure components.

The first radio contour in Fig. 5.2 and Fig. 5.3 show radio emission above a  $3\sigma_{rms}$  threshold, where  $\sigma_{rms}$  is the *rms* noise, which was calculated in each image using CASA. A  $2\sigma_{rms}$  threshold, on low-resolution images, would display more extended emission, highlighting downstream regions and the radio halo component.

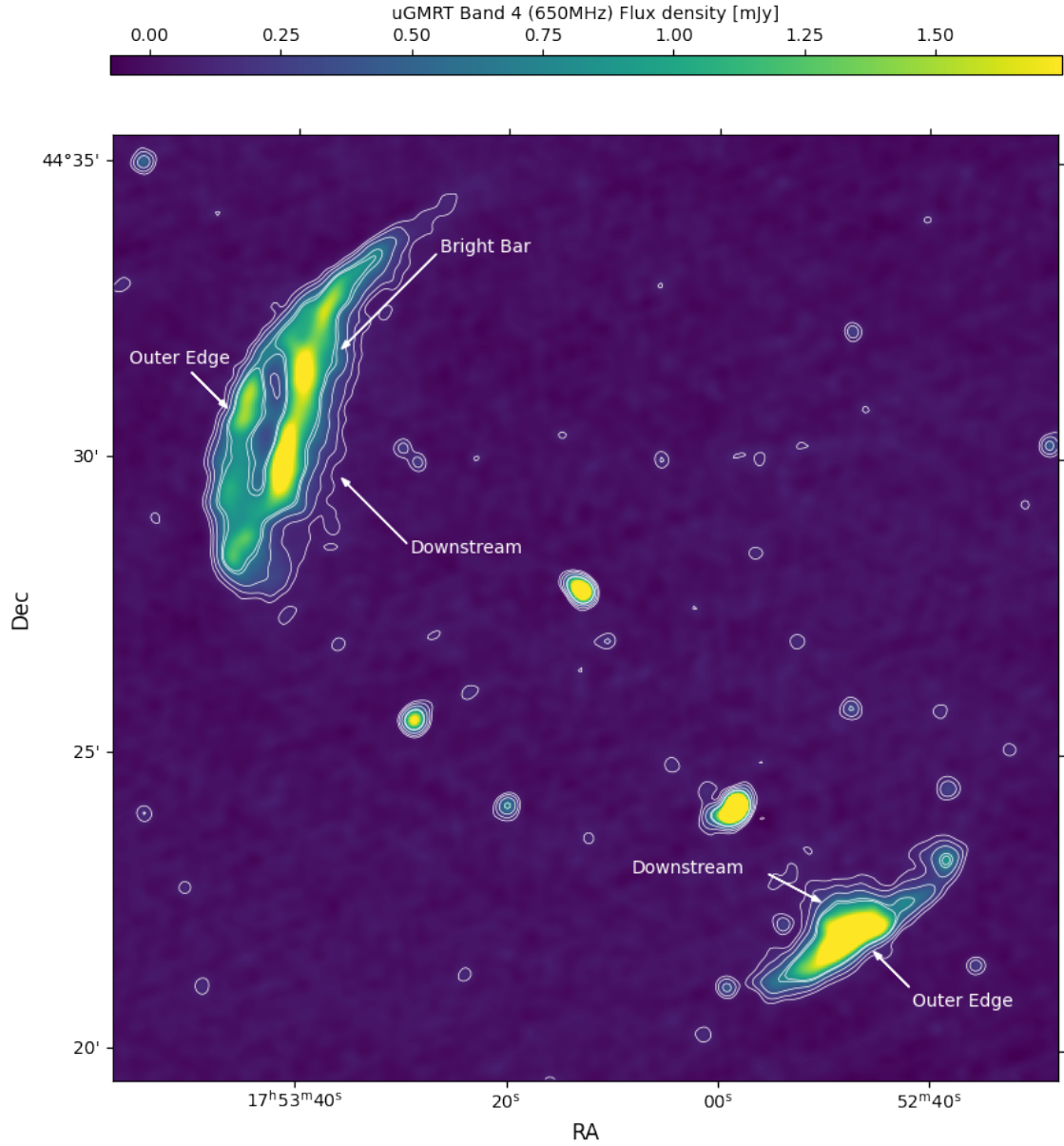


**Figure 5.1:** uGMRT Band 4 (650 MHz) image of MACS J1752+4440. This image, at a resolution of  $3.3'' \times 2.6''$ , is the highest resolution image ever obtained for this cluster. In white, the different structures that make up for the cluster are labelled. The *outer edge* component follows the position of the merger shock that generated the NE relic, the *bright bar* is a substructure present in the downstream region of the first component. The SW relic shows no substructures. Contours are drawn starting at  $3\sigma_{rms}$  and are separated by powers of 2.

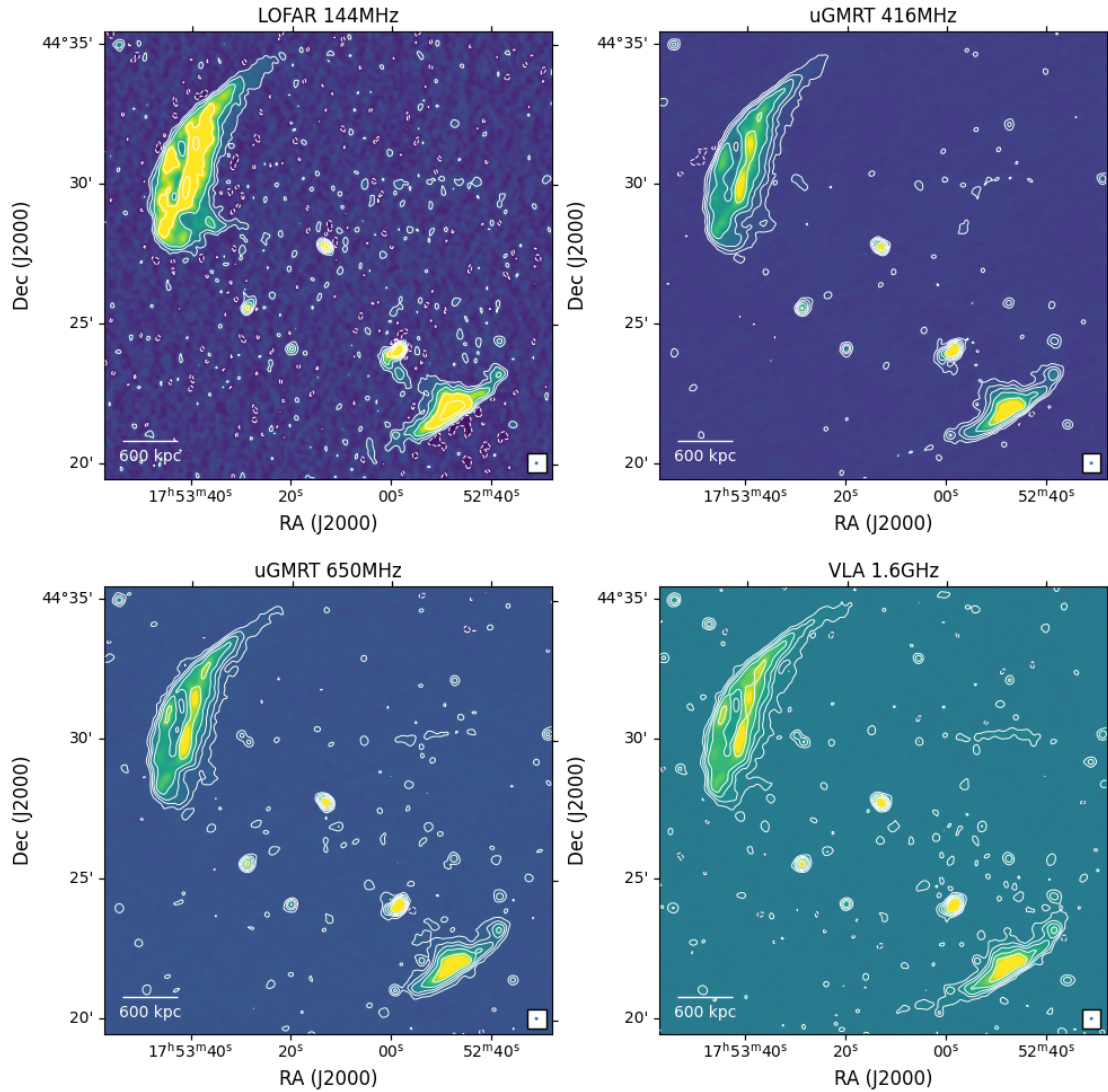


**Figure 5.2:** High-resolution radio images for the MACS J1752+4440 cluster. *Top Left:* LOFAR image at 144 MHz with noise of  $\sigma_{rms,144} = 280 \mu\text{Jy beam}^{-1}$ . *Top Right:* uGMRT image at 416 MHz with noise of  $\sigma_{rms,416} = 70 \mu\text{Jy beam}^{-1}$ . *Bottom Left:* uGMRT image at 650 MHz with noise of  $\sigma_{rms,650} = 23 \mu\text{Jy beam}^{-1}$ . *Bottom Right:* JVLA image at 1.6 GHz with noise of  $\sigma_{rms,1600} = 15 \mu\text{Jy beam}^{-1}$ . Images have a common angular resolution of  $7'' \times 7''$  and contour levels are drawn at  $[-3, 3, 9, 18, 36, 72] \times \sigma_{rms}$  (the negative contour is in dashed). The color scale is logarithmic and beam and scalebar are found at the bottom of the images.

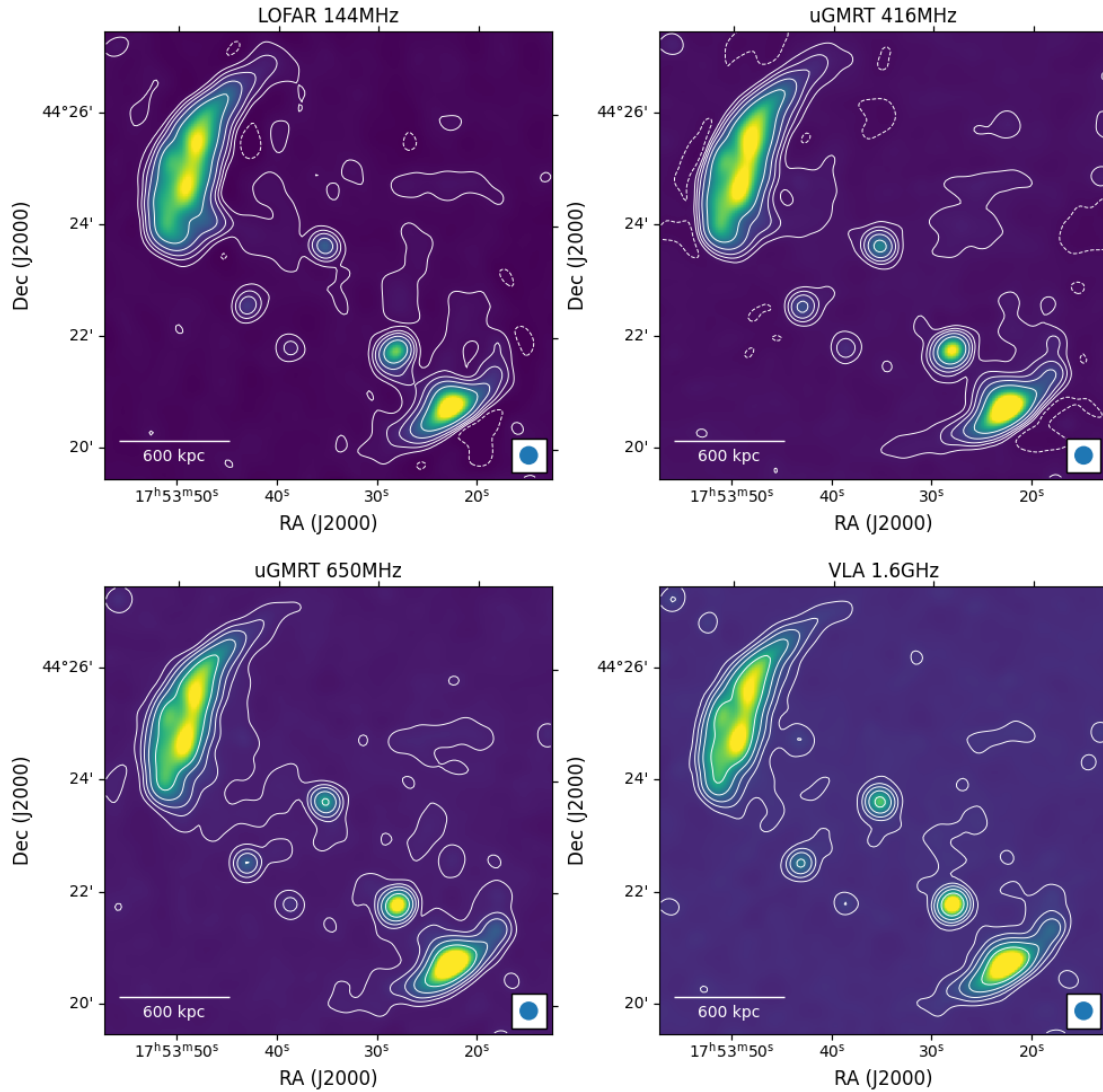


**Figure 5.3:** Low-resolution radio images for the MACS J1752+4440 cluster. *Top Left:* LOFAR image at 144 MHz with noise of  $\sigma_{rms,144} = 350 \mu\text{Jy beam}^{-1}$ . *Top Right:* uGMRT image at 416 MHz with noise of  $\sigma_{rms,416} = 138 \mu\text{Jy beam}^{-1}$ . *Bottom Left:* uGMRT image at 650 MHz with noise of  $\sigma_{rms,650} = 50 \mu\text{Jy beam}^{-1}$ . *Bottom Right:* JVLA image at 1.6 GHz with noise of  $\sigma_{rms,1600} = 50 \mu\text{Jy beam}^{-1}$ . Images have a common angular resolution of  $20'' \times 20''$  and contour levels are drawn at  $[-3, 3, 9, 18, 36, 72] \times \sigma_{rms}$  (the negative contour is in dashed). The color scale is logarithmic and beam and scalebar are found at the bottom of the images.

# Chapter 6

## Discussion

In this Chapter, we discuss the features observed from the spectral index analysis of both relics and we derive the Mach numbers under the DSA assumptions. Furthermore, we discuss the results of the spectral curvature study, making use of the spectral curvature map and the color-color plot diagrams technique, comparing the results with spectral aging models. We propose the possibility of a second shock surface scenario, and analyze our results to verify that option. Using polarization images, we test for projection effects, or the possible action of the complex magnetic field structure, by calculating the polarization fraction and comparing it with the spectral curvature along the NE relic. Finally, we compute the equipartition magnetic field.

### 6.1 Integrated fluxes and spectrum

DSA predicts particle acceleration, and thus synchrotron radio emission, to be dominant at the shock surface and be represented by a power-law spectrum in both particle energy and radio emission. After the shock passage, particles are subject to “aging”, radiating energy through synchrotron and inverse Compton processes, with higher energy particles (responsible for higher frequency emission) aging faster, creating a steepening effect in the power-law, at high frequency, in the radio spectrum. A simplistic model like the one just described would imply that radio relics should be simple structures, with peak emission near the shock front and a progressive decrease of radio emission going into downstream regions. Moreover, as described in Chap. 2.2.1, while the shock acceleration is a widely accepted scenario as the origin of radio relics, some open questions remain for the

feasibility of the DSA mechanism. As an example, the non-detection of any  $\gamma$ -ray signal from accelerated CR protons, or the low acceleration efficiency, not able to explain the observed radio power of most relics (i.e. [Botteon et al., 2020](#)).

MACS J1752+4440 radio relics present a complex structure, which cannot be explained by simple models. Other examples are known in the literature, e.g. the *Toothbrush* relic ([Rajpurohit et al., 2018](#); [Rajpurohit et al., 2020](#)) is a widely studied relic which is composed by several substructures, the “chair”-shaped relic in MACS J0717.5+3745 ([Rajpurohit et al., 2021](#)) and the “ring”-like relic in Abell 3376 ([Chibueze et al., 2023](#)). While the origins of these complex structures in relics are yet unknown, simulations have shown how they could reflect the pre-shock plasma conditions and the shock’s properties. [Wittor et al. \(2023\)](#) and [Hoeft et al. \(2022\)](#) studied filamentary substructures in radio relics using observations and simulations. What they found is that relics are composed of several filamentary structures and, studying the configuration of the magnetic fields and Mach numbers, they found that they consist of similar structures as the relics radio emission. These studies indicate that substructures in radio relics could reflect pre-shock plasma conditions and the shock surface properties. Therefore studying the features and properties of observed radio relics is of crucial importance in understanding their origin.

In order to compare the properties of the relics in MACS J1752+4440 with the predictions from DSA, we analyze here the surface brightness and spectral index properties. From the low-resolution image, we selected two regions enclosing the two radio relics, guided by the  $3\sigma_{rms}$  contours, as shown in the bottom picture of [Fig. 6.1](#). After checking that no contaminating radio sources were present, we measured the two relics’ integrated flux densities, at each frequency, in both high and low-resolution images. Since we obtained consistent results, we conclude that no low surface brightness relic emission is missed in the high-resolution map, so we report the results obtained from high resolution only.

The error on the measured flux density was calculated as:

$$\Delta S = \sqrt{(\sigma_{rms} \cdot \sqrt{N_{beam}})^2 + (f \cdot S_\nu)^2}, \quad (6.1)$$

where  $N_{beam}$  is the number of beams in the region used to evaluate the flux density and  $f$  is the uncertainty of the flux density scale. We used 10% for LOFAR and uGMRT Band 3 ([Shimwell et al., 2019](#), [Shimwell et al., 2022](#)), while uGMRT Band

4 and JVLA have a lower uncertainty of 5% (Chandra et al., 2004; Perley and Butler, 2013).

From the LOFAR high-resolution image, we measure an integrated flux density of  $S_{144}^{NE} = 530 \pm 50$  mJy for the NE relic and  $S_{144}^{SW} = 177 \pm 18$  mJy for the SW relic. The integrated spectra for both radio relics are displayed on top of Fig. 6.1. The spectra provide useful information to discriminate between particle acceleration models proposed for radio relics. In the considered frequency range, the observed radio spectra appears to be straight and perfectly represented by a power-law fit, in line DSA model predictions.

**Table 6.1:** Measured flux densities at each of the four frequencies for the NE and SW relic, integrated spectral index and radio power at 144 MHz.

	Frequency [MHz]	Flux density [mJy]	$\alpha_{int}$	$P_{144}$ [WHz <sup>-1</sup> ]
NE relic	144	530 ± 50	−0.91 ± 0.06	2.40 × 10 <sup>26</sup>
	416	203 ± 20		
	650	130 ± 10		
	1600	62 ± 30		
SW relic	144	177 ± 18	−0.83 ± 0.05	7.90 × 10 <sup>25</sup>
	416	79 ± 6		
	650	56 ± 4		
	1600	26 ± 1		

Surprisingly, this fit gives two integrated spectral indices  $\alpha_{int}^{NE} = -0.91 \pm 0.06$  and  $\alpha_{int}^{SW} = -0.83 \pm 0.05$ , different from previous studies, as cited in Chap. 3, which obtained steeper integrated spectral indices. A detailed summary of these results is listed in Table 6.1. Furthermore, in the considered frequency range, the spectrum shows no sign of steepening at higher frequencies and is perfectly represented by the single power-law. The two relics have a largest-linear size (LLS) of  $\mathcal{L}_{NE} = 1.3$  Mpc and  $\mathcal{L}_{SW} = 0.7$  Mpc.

The radio luminosity is related to the measured integrated flux density  $S_\nu$  by

$$P_\nu = 4\pi D_L^2(z)(1+z)^{-(1+\alpha_{int})} S_\nu, \quad (6.2)$$

where  $D_L$  is the luminosity distance and the scaling by  $(1+z)^{-(1+\alpha_{int})}$  is commonly referred to as the *k-correction*. We found a radio power of  $P_{144\text{MHz}}^{NE} = 2.40 \times 10^{26}$  WHz<sup>-1</sup> and  $P_{144\text{MHz}}^{SW} = 7.90 \times 10^{25}$  WHz<sup>-1</sup> for the NE and SW relic, respectively. These radio luminosity are in agreement with literature studies about the cluster and are comparable with commonly observed radio luminosity in radio relics. In addition, the radio powers of simulated radio relics match with our observation (Wittor et al., 2021).

Under the assumption that particles are accelerated at the shock front, generating the radio relics, we expect a steepening of the spectral index going towards cluster center, with the flattest spectral index along the merger shock. As we detected multiple components along the NE relic, we investigated the influence of the structure on the spatial variation of the spectral index, across the two relics, by producing integrated spectral index maps, and corresponding error maps, for both high and low-resolution images. This was done by performing a power-law fit between the measurements in each pixel, using all four frequencies, through the `polyfit` method of the `Numpy` package in Python. The uncertainty on this spectral index is obtained by calculating the uncertainty of the `polyfit` method, calculated as the square root of the diagonal of the covariance matrix, generated by the numerical method (Richter, 1995).

On the contrary to what is predicted by a simple aging model, Fig. 6.3 shows a spectral index distribution of  $\alpha \sim -0.6$  to  $-0.8$ , with associated errors of  $\Delta\alpha \sim 0.02$ , which follows the same spatial distribution of the flux densities, clearly showing the same substructures, as previously defined. In fact, despite the SW relic shows a uniform sign of steepening along its minor axis, the NE relic reflects the “outer edge” + “bright bar” composition, showing steepening between the main shock and the filament, followed by a flattening of the spectral index along the filament. This behavior resembles the one of another shock surface, providing us with hints about the relic’s origin.

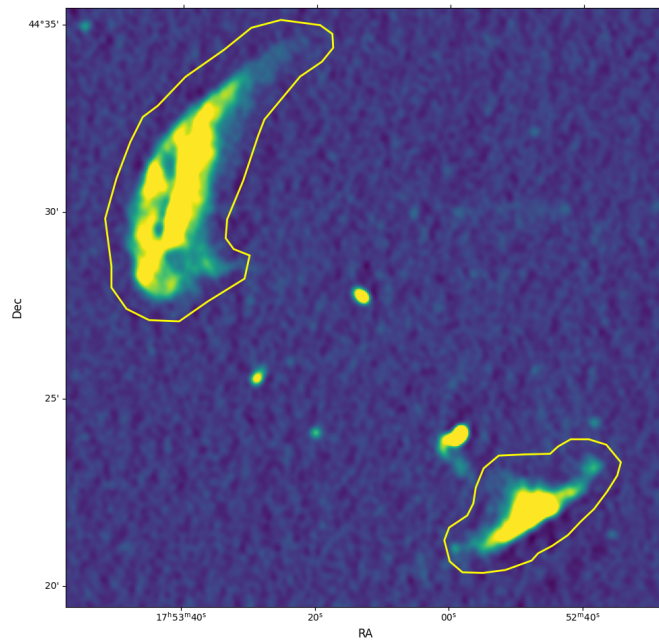
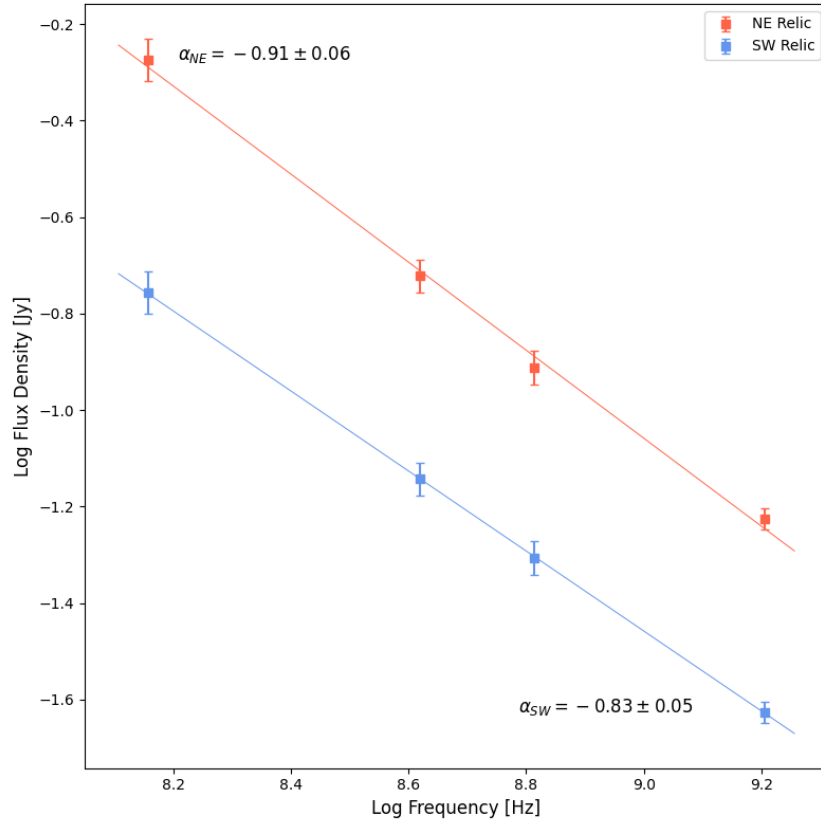


**Figure 6.1:** *Top:* Spectra for NE (red) and SW (blue) relic, fitted by two power-laws. *Bottom:* LOFAR high-resolution continuum image at 144 MHz with the regions used to estimate the flux density of the two relics over-imposed in yellow.

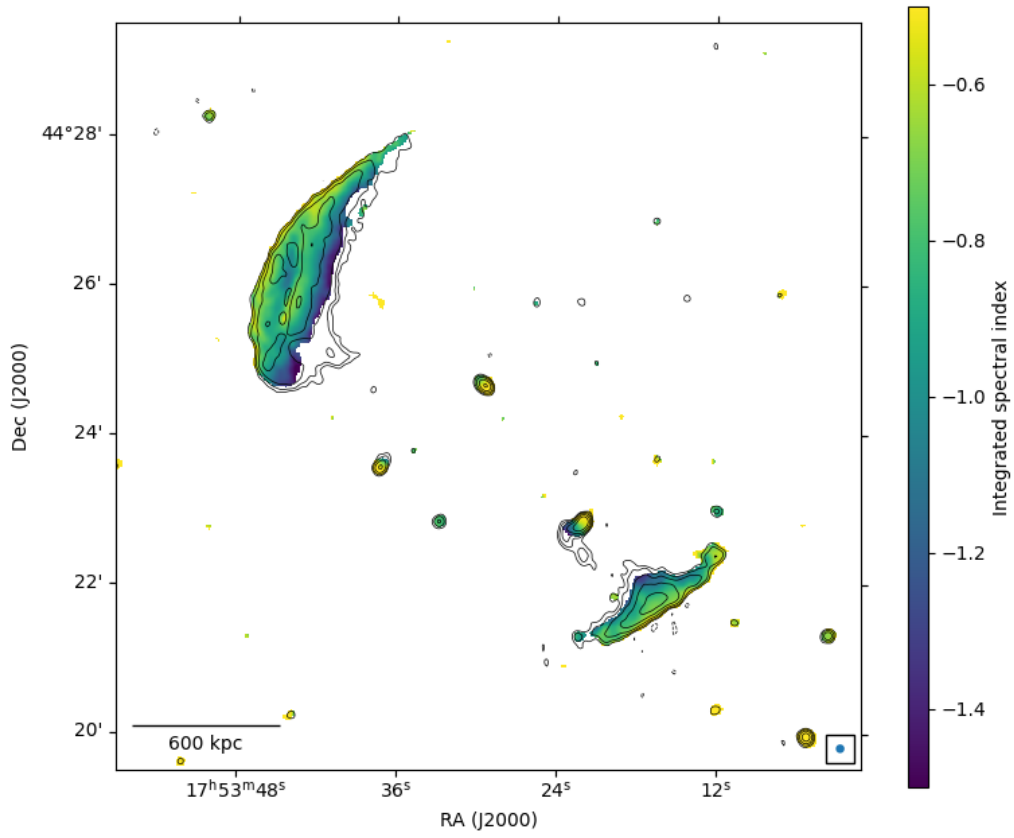


**Figure 6.2:** Integrated spectral index map, obtained by fitting the four measurements in each pixel above a  $3\sigma_{rms}$  level. Contours are drawn from the LOFAR 144 MHz image, starting from a  $3\sigma_{rms}$  level and spaced by powers of 2.

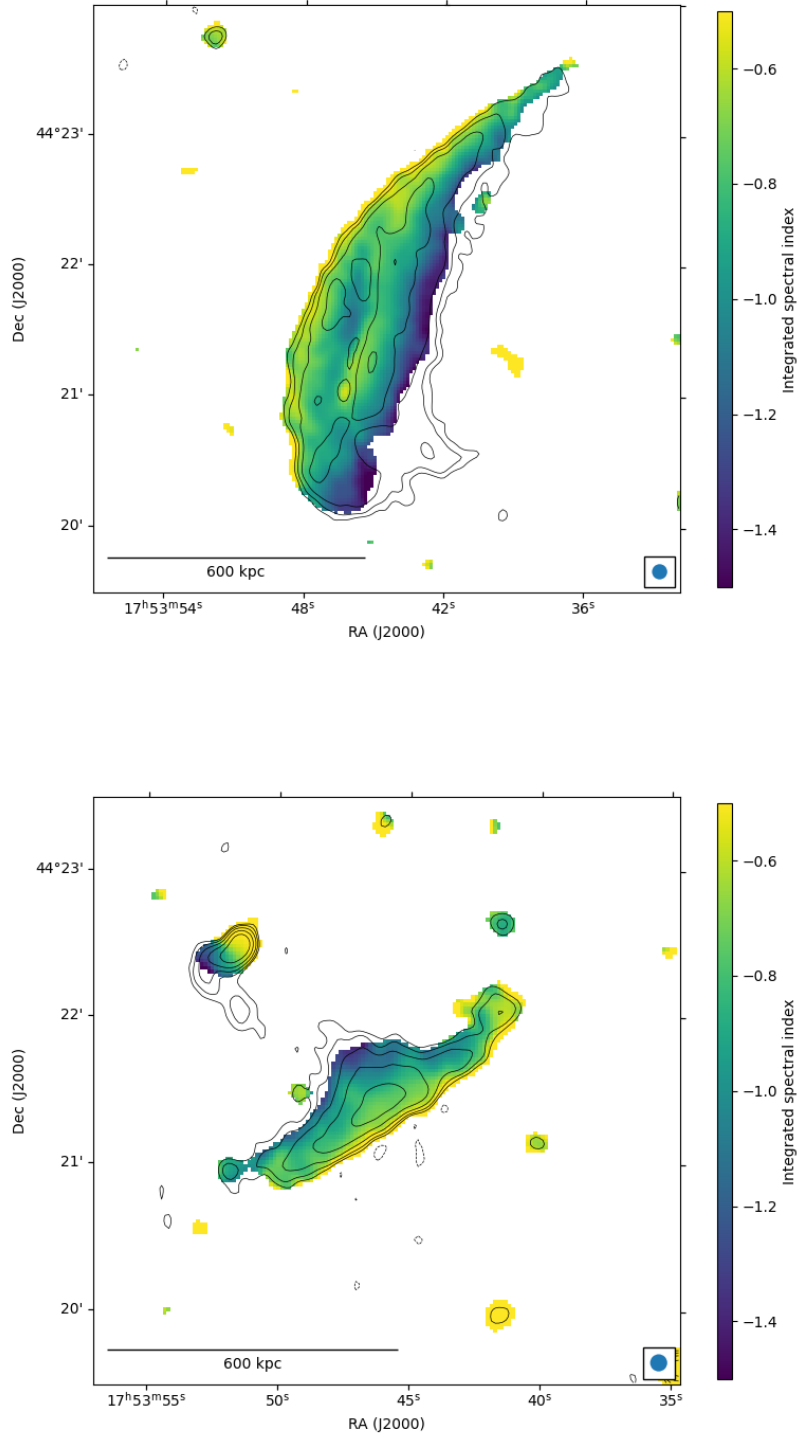


**Figure 6.3:** *Top:* Zoom in view of the NE relic in the integrated spectral index map. *Bottom:* Zoom in view of the SW relic in the integrated spectral index map. Contours are drawn from the LOFAR 144 MHz image, starting from a  $3\sigma_{rms}$  level and spaced by powers of 2. The spectral index error map is present in [APPENDIX A](#).

## 6.2 Surface brightness and spectral index profiles

Numerical simulations, such as [van Weeren et al. \(2011\)](#), have shown that a merger-driven bow shock, with electrons injected at the shock, would generate a radio relic with a surface brightness profile that peaks at the shock front and decreases along the length of the relic. To verify this, in this thesis, we produced surface brightness profiles, by calculating the surface brightness on regions selected along the relics major axis. These regions (see top of [Fig. 6.4](#)) were drawn using elliptical arcs, with the width equal to the beam size (7").

[Fig. 6.5](#) shows the brightness profile at high-resolution for the NE and SW relics. These show that the peak emission for the NE relic happens in region 4-5, approximately overlaid to the position of the *bright bar*, with a secondary peak in region 2, close to the *outer edge* and a sharp drop toward cluster center. This profile highlights the presence of two main substructures. On the contrary, the SW relic displays a much simpler profile, with peak brightness in region 2, followed by a linear decrease toward downstream regions. Both the profiles are in agreement with literature studies on this cluster, that observed the peak flux to not be in the outermost position of the two relics, but slightly centered in their structure, without being able to resolve the NE substructures. It is notable how the same profile shape is kept between the four observed frequencies.

As we mentioned in the previous chapter, considering a single shock scenario producing particle (re-)acceleration, the expected spectral index profile for a radio relic would be a linear decrease of the spectral index, with the flattest spectra at the position of the merger shock, further out in cluster outskirts, steepening toward cluster center.

To study the origin and infer the spectral properties of the radio emission of the two relics, we produced spectral index profiles at high and low-resolution by calculating the spectral index on the same elliptical regions generated for the high-resolution brightness profiles, together with low-resolution elliptical regions of 20" width (see bottom of [Fig. 6.4](#)).

The spectral index was computed using the general equation:

$$\alpha = \frac{\log\left(\frac{S_1}{S_2}\right)}{\log\left(\frac{\nu_1}{\nu_2}\right)}, \quad (6.3)$$

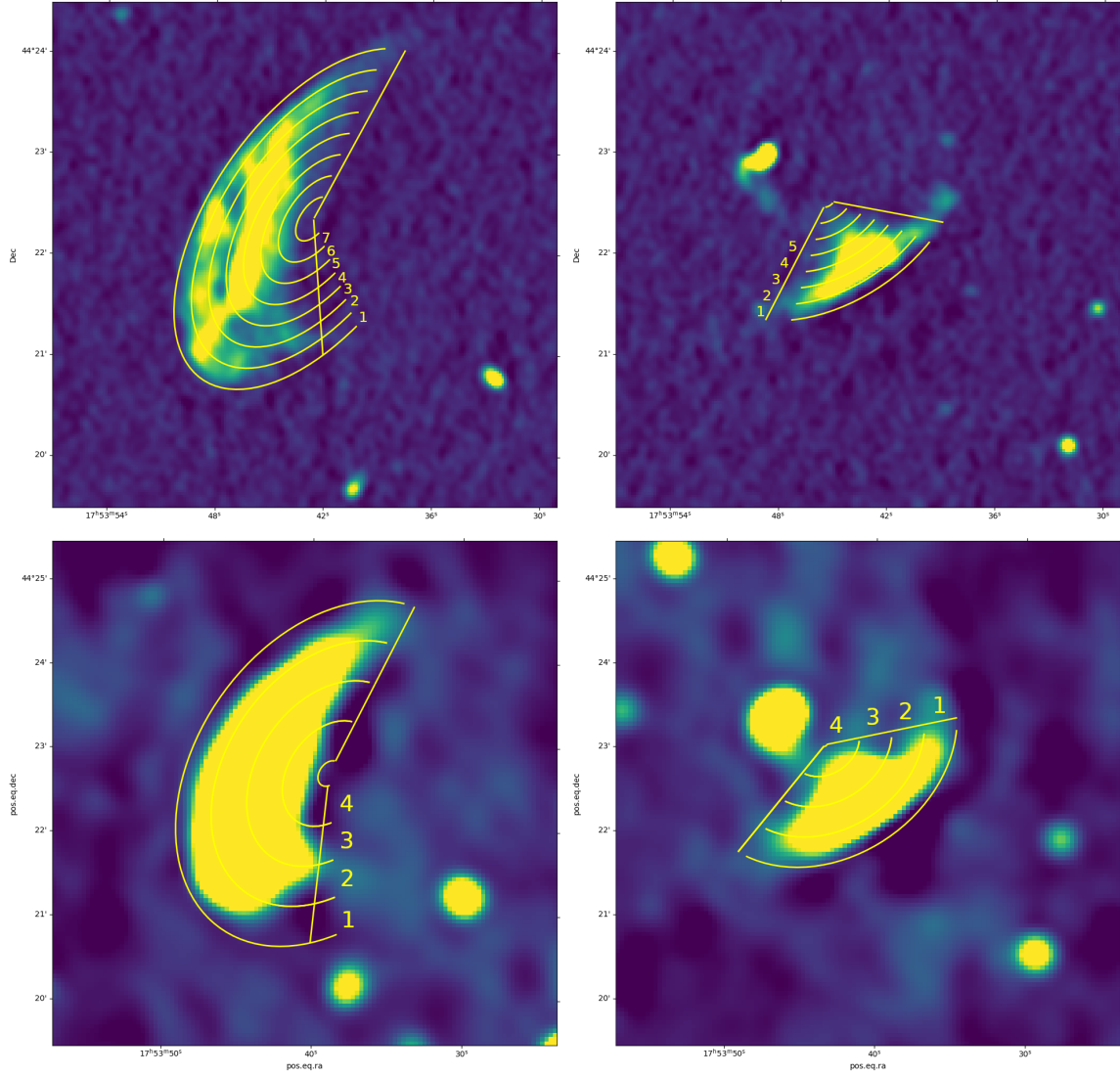


**Figure 6.4:** *Top:* High-resolution LOFAR image, with Epana regions overlying on the two radio relics. *Bottom:* Low-resolution LOFAR image, with Epana regions overlying on the two radio relics. Regions are numbered from 1 starting from the outer one, laying on the position of the merger shock, to the center of the cluster.

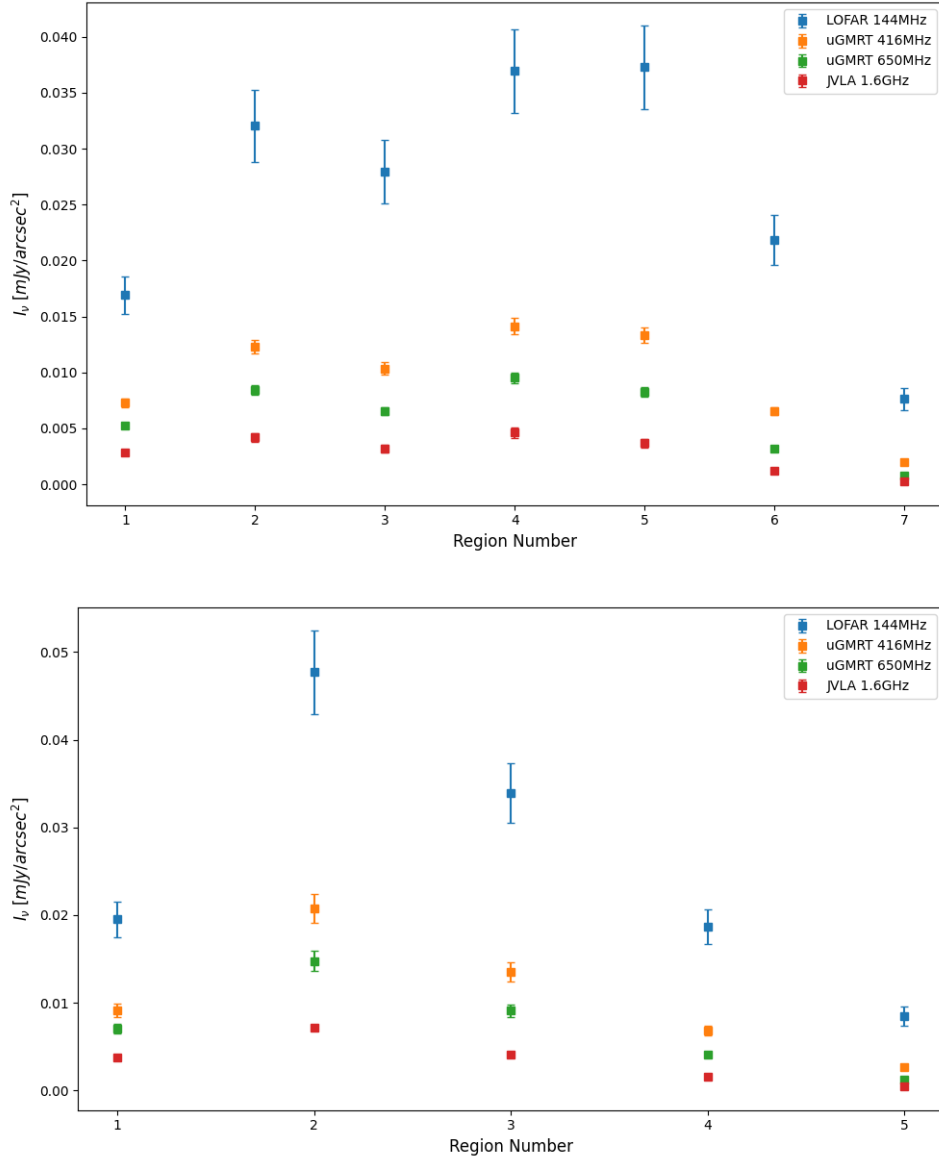


**Figure 6.5:** Surface brightness profiles for both radio relics. *Top:* Profile of the NE relic. The profile presents the peak brightness in region 4 and 5, with a second peak in region 2. This profile is consistent with what can be seen in the spectral index profiles, with two peaks in the position of the two substructures of the relic. *Bottom:* Profile of the SW relic. The profile shows the peak brightness in region 2, followed by a fast decline in the downstream region.

where  $S_1$  and  $S_2$  are the measured flux densities at  $\nu_1$  and  $\nu_2$  frequencies. The uncertainty on the spectral index is calculated as:

$$\Delta\alpha = \left| \frac{1}{\log \frac{\nu_1}{\nu_2}} \right| \sqrt{\left( \frac{\Delta S_1}{S_1} \right)^2 + \left( \frac{\Delta S_2}{S_2} \right)^2}, \quad (6.4)$$

where  $\Delta S_1$  and  $\Delta S_2$  are the corresponding flux density uncertainties, calculated as in Eq. 6.1.

In Fig. 6.6 and 6.7, we compare the spectral indices calculated between LOFAR (144 MHz) and uGMRT Band 3 (416 MHz) along with uGMRT Band 4 (650 MHz) and JVLA (1.6 GHz). The NE relic profiles, shown on top in Fig. 6.6, reveal a non-linear trend, with flattest spectral index in region 1 at  $\alpha_{416MHz}^{144MHz} = -0.79 \pm 0.10$  and  $\alpha_{1.6GHz}^{650MHz} = -0.67 \pm 0.12$ , which coincides with the position of the *outer edge*, and a flattening in region 3-4, possibly highlighting a re-accelerated region (approximately at the position of the *bright bar*) instead of a linear decrease of the spectral index. The feature observed in the high resolution profile was not detected by previous literature about the cluster, which, being at much lower resolutions, were not able to resolve the substructures of the NE relic and to observe the flattening along the *bright bar*.

Although the spectral indices at higher frequencies are consistently flatter, they do not show a clear second peak in region 4 as in the low frequency case, but actually a flat behaviour between regions 2 and 4. Nonetheless, the profile is consistent within the uncertainties. This kind of profile is compatible with the observations of two substructures, and in line with the assumption of further (re-)acceleration along the downstream region of the merger shock. In contrast, the high-resolution profile for the SW relic shows a linear decrease of the spectral index, with a similar profile between the two frequency ranges. This profile resembles the behaviour of a simple, single merger shock model.

The distance between the *outer edge* and the *bright bar* is roughly 150 kpc. The radiative lifetime of relativistic electrons undergoing synchrotron and inverse Compton losses is given by (Kang et al., 2012):

$$t_{rad} = 1590 \frac{B^{0.5}}{(B^2 + B_{CMB}^2) \sqrt{\nu(1+z)}} \text{ Myr}, \quad (6.5)$$

where  $B$  and  $B_{CMB} = 3.25 \cdot (1+z)^2$  are the magnetic field and inverse-Compton equivalent field in  $\mu\text{G}$ ,  $\nu$  is the observing frequency in GHz and  $z$  the redshift. If we

assume the equipartition magnetic field for the NE relic ( $B \sim 1\mu\text{G}$ , see Chap. 6.6), and calculate the radiative age at a frequency of 144 MHz, we obtain a radiative age of  $t_{rad} \sim 94\text{Myr}$ . This timescale, assuming a typical downstream velocity of  $v \sim 1000\text{ km s}^{-1}$ , corresponds to a cooling length behind the shock of  $L_{rad} \sim 100\text{ kpc}$ . By comparing this cooling length with the observed distance between the *outer edge* and the *bright bar*, we notice that the two distances are comparable. This could explain the drop in the brightness profile in region 3, however, further particle acceleration must be present to reproduce the relic structure at larger distances.

At low-resolution (see Fig. 6.7), the NE relic profiles show a linear decrease of the spectral index, in line with a scenario in which particles progressively age in the downstream region of the shock. The peak of the spectral index is in region 1 with values  $\alpha_{416\text{MHz}}^{144\text{MHz}} = -0.71 \pm 0.12$  and  $\alpha_{1.6\text{GHz}}^{650\text{MHz}} = -0.68 \pm 0.11$ . The profile appears different between the two frequency bands, with the high frequency profile decreasing faster — as expected from aging models — despite having flatter indices closer to the position of the shock. The steepening of the spectral index happens in regions representing the downstream, making the plot consistent with the one at high-resolution. Clearly, at low-resolution it is not possible to resolve the fine details of the *outer edge+bright bar* substructures and the profile is in agreement with literature studies.

The profiles obtained from low-resolution images of the SW relic show a peculiar feature, in which at high frequency we observe steeper spectral indices and a sharp drop in region 4, while at low frequency the spectral index has a slow decrease and a hint of flattening at the downstream. This profile is likely contaminated by a radio source in the vicinity of the SW relic (cluster member source at  $z \sim 0.37$ ; Finner et al., 2021), as seen in Fig. 6.8, generating a sort of “bridge” emission that can be detected only at low frequency and at  $\sim 20''$  resolution. In each high frequency profile, the most downstream region shows large error bars. This is due to the low JVLA flux density, with respect to uGMRT band 4, on said regions. Considering the simple scenario in which two opposite shocks are generating the two radio relics, the constantly flatter spectral profile at higher frequency shown in the NE relic profile is unexpected, as particles, being accelerated, will radiate and lose energy faster at higher frequency. This could be a sign of a complex shock surface, paired with projection effects. Moreover, as observed from Fig. 6.5 and Fig. 6.6, the cluster presents a “feature” in which the region with flattest spectral index (region 1) is not the region of highest surface brightness (region 4-5),

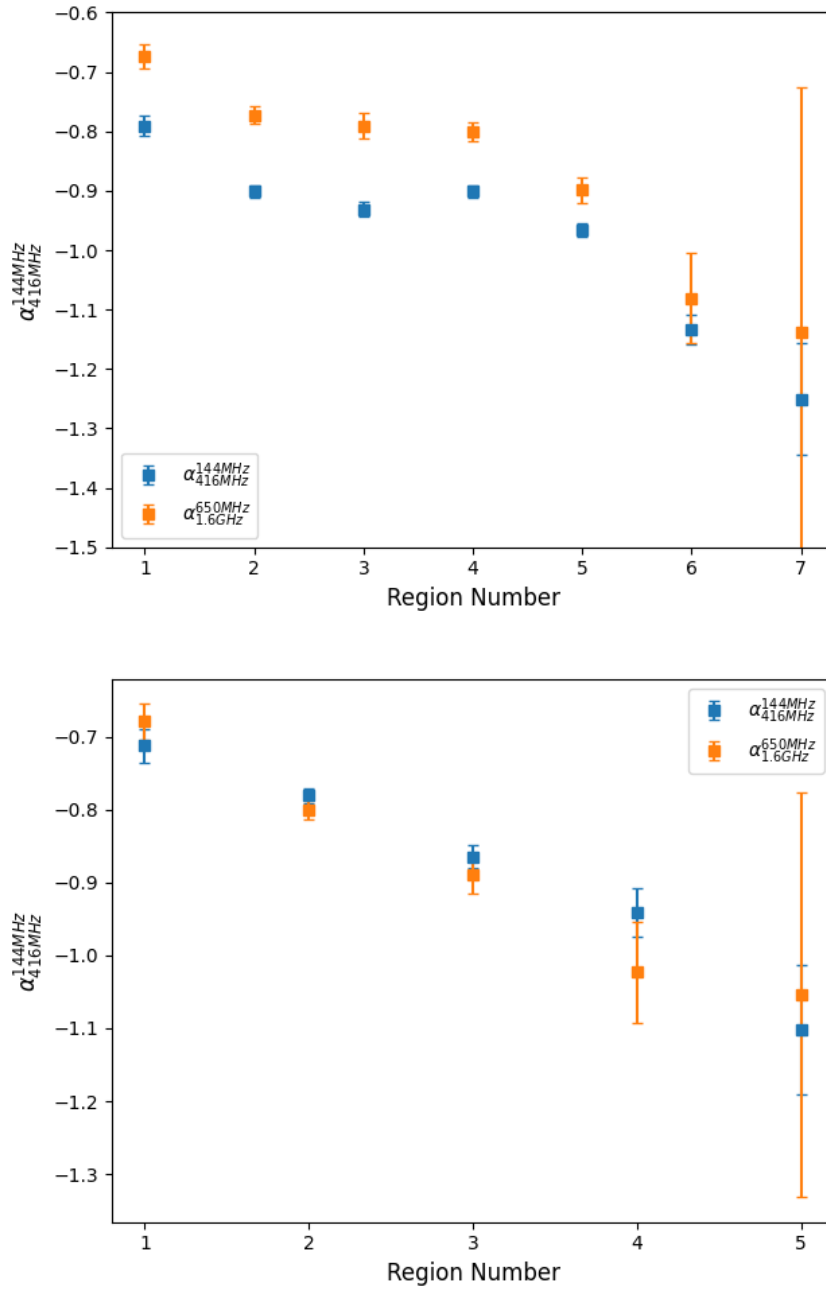


**Figure 6.6:** Spectral index profiles, calculated in the two frequency ranges, at high-resolution. *Top:* Profiles for the NE relic. The low-frequency profile shows two peak of spectral index, one at the position of the merger shock and one at the position of the substructure. The profile at high frequency is different, displaying a flat behaviour along the regions overlaid to the *bright bar* substructure. Both profiles show a sharp drop of spectral index into downstream regions. *Bottom:* Profiles for the SW relic. Both profile show a similar trend, decreasing toward cluster center.

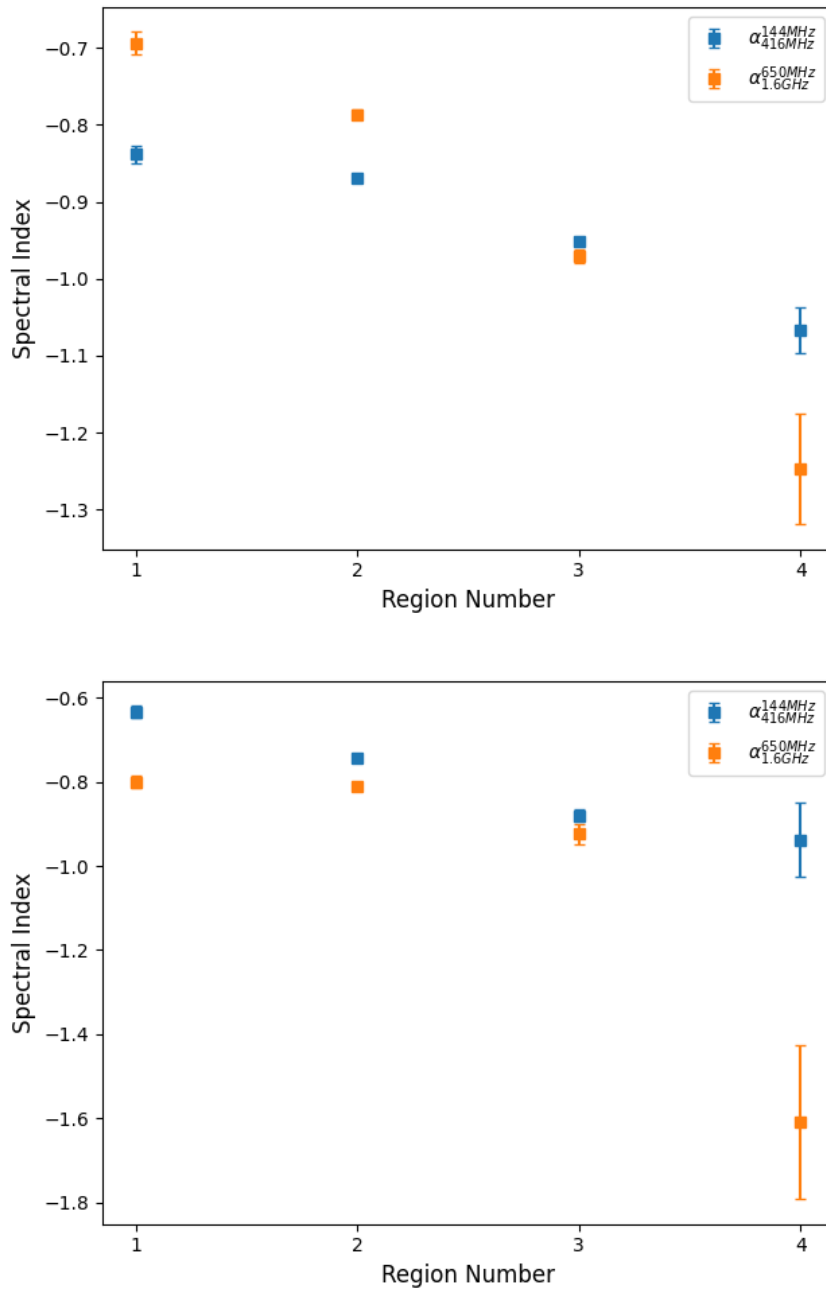


**Figure 6.7:** Spectral index profiles, calculated in the two frequency ranges, at low-resolution. *Top:* Profiles for the NE relic. Both profiles show a linear decreasing trend, with the high-frequency profile starting from flatter spectral indices but steepening faster, while the low-frequency profile shows a slower decreasing trend. *Bottom:* Profiles for the SW relic. The peculiar shape for the low-frequency profile, which starts as decreasing and seem to flatten at the downstream, might be connected to the presence of a nearby radio source. As the emission is not observed at high frequency, the high-frequency profile sharply drops at the downstream region.

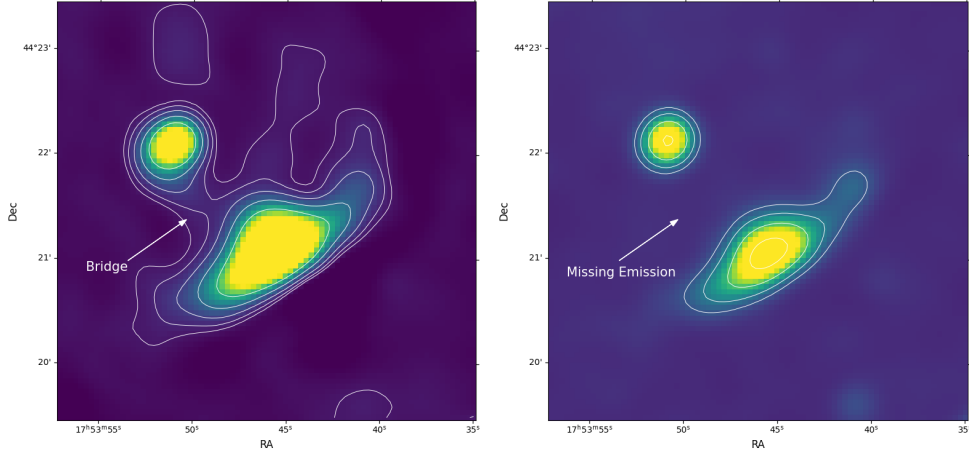


**Figure 6.8:** Zoom view of the SW relic. *Left:* LOFAR 144 MHz image, that highlights the presence of radio emission coming from the region in between the SW relic and the close radio source, here called “bridge”. *Right:* JVLA 1.6 GHz image of the same region of space. The missing emission is highlighted. Contours are drawn at a  $3\sigma_{rms}$  level and spaced by powers of 2.

which actually coincide with the regions overlaying the *bright bar* substructure, which show a flattening of the spectral index in the spectral profile. To visualize this “feature”, we plotted the radio brightness measurement along each region, fitted with a power-law line, in Fig. 6.9, for both resolutions. As expected from synchrotron models, the measurements are perfectly reproduced by power-law emission. Additionally, the region along the merger shock presents the flattest spectrum, as expected from the spectral profile, but the regions containing the inner components is at the highest brightness. The observed filament and its imprint in the surface brightness profile and the spectral index profile could be due to projection of substructures from a complex shock front, in opposition with models of a simple spherical bow shock. On top of that, the same structures could be generated by a fluctuating Mach number distribution inside the relic structure, as predicted by Wittor et al. (2017), or by changes in the electron acceleration efficiency. Finally, the same structure could also reflect a complex magnetic field structure, in which magnetic reconnection is induced by the merger shock (Owen et al., 2014).

In summary, our analysis indicates that the features observed in the brightness and spectral index profiles cannot be produced by a single shock surface passing through the ICM, but instead, considering the double peak on the brightness profile and the flattening of the spectral index profile of the NE relic, we are likely observing the fine details of a complex shock surface and magnetic field structure.

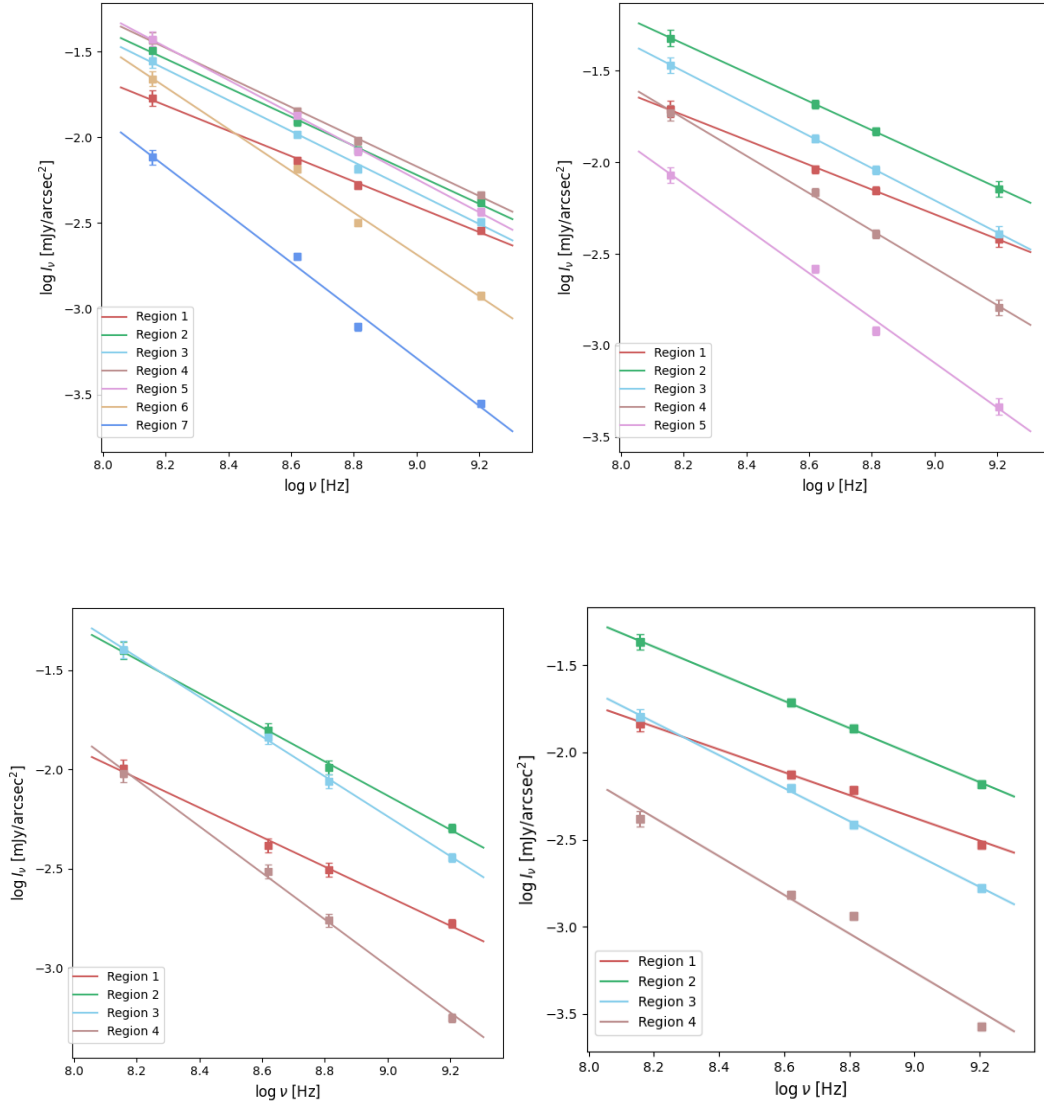


**Figure 6.9:** Spectra for the NE and SW relic at high and low-resolution. *Top:* High-resolution plot of the brightness measurements for both radio relics. *Bottom:* Low-resolution plot of the brightness measurements for both radio relics. It is notable how in each plot the brightness measured in region 1 is lower with respect to the one central to the relic, but the spectrum is flatter. Going toward the center of the cluster, we observe a lowering of the brightness, together with a steepening of the spectrum.

### 6.2.1 Mach Numbers

As previously described, the DSA model for particle acceleration (see Chap. 2) is ordinarily used to describe particle acceleration in astrophysical shocks, which are believed to generate radio relics. In this scenario, considering a power-law energy distribution of relativistic electrons  $n_E \propto E^{-\delta}$ , the slope  $\delta$  is related only to the shock's strength as:

$$\delta_{inj} = 2 \frac{\mathcal{M}^2 + 1}{\mathcal{M}^2 - 1}. \quad (6.6)$$

Under stationary conditions, assuming that the physical conditions in downstream regions do not change significantly with distance from the shock front, the integrated electron spectrum follows a power-law with slope  $\delta = \delta_{inj} + 1$ . The synchrotron emission theory tells us that this population produces radio emission that is also described by a power-law. Therefore, in the model for radio relics (e.g. [Hoeft and Brüggén, 2007](#)), the radio Mach number can be estimated from the integrated radio spectrum, that follows a power-law which depends only on the Mach number, as:

$$\alpha_{int} = - \frac{\mathcal{M}^2 + 1}{\mathcal{M}^2 - 1}. \quad (6.7)$$

This derivation depends on specific assumptions about the properties of the shock. At first, the shock has to be planar on the plane of the sky, and both the downstream velocity and magnetic field are assumed to be uniform. Then, the model assumes that all the observed frequencies are below the critical synchrotron frequency (hence below the maximum energy electrons injected by DSA). At last, the model considers radiative energy losses only. Considering the strong assumptions, if the scenario is more complicated, as in the case of a complex shock surface or complex magnetic field structure, Eq. 6.7 does not strictly hold and other results are possible.

Another useful relation coming from DSA relates the Mach number  $\mathcal{M}$  of a shock to the injection radio spectral index ( $\alpha_{inj}$ ) as

$$\alpha_{inj} = \frac{1}{2} - \frac{\mathcal{M}^2 + 1}{\mathcal{M}^2 - 1} = \frac{1}{2} + \alpha_{int}. \quad (6.8)$$

Using Eq. 6.7 it is possible to calculate the Mach number of the shock starting from the observed spectral index as

$$\mathcal{M} = \sqrt{\frac{\alpha_{int} - 1}{\alpha_{int} + 1}}. \quad (6.9)$$

As a consequence, DSA predicts that for strong shocks ( $\mathcal{M} \rightarrow \infty$ ),  $\alpha_{int} \rightarrow -1$ , while for weak shocks ( $\mathcal{M} < 5$ ),  $\alpha_{int} < -1$ . In the case of merger shocks, observations and simulations have shown that the Mach numbers are always in the weak shock regime (i.e. [Skillman et al., 2013](#)), therefore the expected value for the integrated spectral index is  $\alpha_{int} < -1$ . As the integrated spectral index for either relics of MACS J1752+4440 is  $\alpha_{int} > -1$ , the Mach number cannot be calculated through [Eq. 6.7](#).

As a consequence, using [Eq. 6.8](#), we calculated the Mach number related to the injection spectral index of the shock  $\alpha_{inj}$ , where the injection spectral index was assumed as the spectral index calculated in the regions along the merger shock (region 1), that we reported in the previous section. The results obtained for both radio relics and both resolutions are shown in [Tab. 6.2](#).

As described in [Eq. 6.8](#), DSA predicts a steepening of the electron spectrum, while [Table 6.2](#) shows how in this case the integrated spectral index is smaller than the injection spectral index by  $\sim -0.2$  only, meanwhile remaining  $> -1$ .

As described in [Chap. 1.1](#), Mach numbers related to cluster merger shocks can be calculated from X-ray observations from deprojected temperature or density jumps. However, it is now known that the Mach number derived using X-ray observation differs from the one derived from radio data. This could be due to biases in the observations, pre-shock properties of the ICM or the acceleration mechanism. For example, in the cases in which the X-ray Mach number can be calculated from both the temperature and density jump, the temperature based measurement yields for larger values, indicating a possible systematic effect. Many technical difficulties can arise in X-ray observations of pre and post-shock temperature, as described by [Akamatsu et al. \(2017\)](#) and references therein. In radio observations, the integrated spectrum and radio Mach number can be difficult to measure, as several radio measurement are based on a small frequency range.

In general, the X-ray derived Mach numbers for cluster merger shocks are low, with values of  $M_{X-ray} \approx 1.5 - 2.5$ , while radio observations yield for larger corresponding radio Mach numbers of  $M_{radio} \approx 2 - 5$  ([Wittor et al., 2021](#)). [Stuardi et al. \(2022\)](#) conducted a study on a sample of observed radio relics, which we can use to compare our results with literature studies. Comparing our results with the relics listed in this work, we can conclude that the injection Mach number that we obtained for the NE relic, at  $\mathcal{M} = 3.12^{+0.82}_{-0.42}$ , is in agreement with other observations, while the Mach number we obtained for the SW relic, at  $\mathcal{M} = 4.19^{+0.94}_{-0.50}$  is the highest of the

**Table 6.2:** Spectral indices and Mach numbers of both radio relics. Numbers between parenthesis are referred to 20" resolution. Integrated Mach numbers cannot be calculated and so are not present.

	$\alpha_{inj}$	$\mathcal{M}_{inj}$	$\alpha_{int}$	$\mathcal{M}_{int}$
NE	$-0.72 \pm 0.1$ ( $-0.74 \pm 0.04$ )	$3.12^{+0.82}_{-0.42}$ ( $3.03^{+0.25}_{-0.20}$ )	$-0.91 \pm 0.06$	...
SW	$-0.67 \pm 0.07$ ( $-0.65 \pm 0.14$ )	$4.19^{+0.94}_{-0.50}$ ( $4.18^{+1.03}_{-0.92}$ )	$-0.83 \pm 0.05$	...

sample.

Cosmological simulations (Vazza et al., 2019; Bykov et al., 2019 and reference therein) show that shocks with these Mach numbers are very rare events and that the Mach number can vary greatly along the shock front. If this is the case, the Mach number derived from the radio spectral index would be biased to higher values, as the synchrotron luminosity strongly increases with the Mach number. Therefore, Mach numbers derived from X-ray observations could end up being smaller with respect to their radio counterpart. A comparison on Mach numbers calculated from X-ray observations of MACS J1752+4440 double-relics system could help understand the origin of the radio–X-rays Mach number discrepancy and the origin of the relics.

### 6.3 Evidence of a second shock surface?

From the previous sections analysis on the brightness and spectral index, the *bright bar* substructure can be interpreted as a second shock surface traveling through the downstream region of the NE relic, generated by the merger. In this scenario, further particle (re-)acceleration would generate a second population of radio emitting relativistic electrons.

Under this assumptions, if we consider the spectral index profile for the NE relic in Fig. 6.6, the secondary peak — and the flattening at high frequencies — along the regions of the *bright bar*, could be explained. In the same manner, considering the observed brightness profiles in Fig. 6.5, the bump in brightness along the same regions suggests that a second shock scenario could explain the misalignment between the peak brightness and the position of the merger shock.

Assuming particle re-acceleration due to a second shock, Markevitch et al. (2005) have shown that if the slope of the fossil plasma is steep (as it should due to radiative cooling), shock re-acceleration should create a spectrum with slope similar to the one produced by Fermi re-acceleration. Therefore, this further particle acceleration would change the steepening of the downstream region of the first shock, making the integrated spectral index, calculated on the whole relic structure, appear flatter than in the case of one shock only. This can be a possible explanation of the shallower steepening observed with respect to the one predicted by DSA in Eq. 6.8 on the integrated spectral index and the reason for which DSA equations cannot be applied, as discussed in Chap. 6.2.1.

To better understand the origin of the *bright bar*, we calculated the injection Mach number, using as injection spectral index the integrated spectral index calculated in region 4, in which we see the secondary peak in Fig. 6.6. The spectral index of said region is  $\alpha_{sub} = -0.86 \pm 0.02$  which corresponds to a Mach number of  $\mathcal{M}_{sub} = 2.54_{-0.06}^{+0.07}$ . This Mach number is smaller with respect to the one calculated along the *outer edge*, on the position of the merger shock. This implies that, if a second shock surface is responsible for the origin of the substructure, it was weaker than the merger shock that generated the relic, or that we are observing a combination of downstream from the first shock surface and a second injection.

As a result of this assumption, it was interesting to check the presence of more than one particle population with different radiative ages along the NE relic structure. To accomplish this, we generated a grid of boxes of the beam size (7'') covering the

two radio relics, coloring the boxes based on their location across their size (see Fig. 6.10). Using these boxes, we plotted the spectral index calculated between LOFAR 144 MHz and JVLA 1.6 GHz against the LOFAR 144 MHz flux density, color coding the points based on the position of the box along the relic. Fig. 6.11 shows that the *outer edge* spans more or less one order of magnitude in flux density, having the flattest spectral indices, as observed in the previous profiles. The points regarding the *bright bar* are the points at higher flux density, as observed in the flux density profiles, and they are at steeper spectral indices. To quantify the change in spectral index between the two regions, we calculated the average spectral index between the *outer edge* and *bright bar* points. We obtained  $\langle \alpha_{edge} \rangle = -0.76 \pm 0.02$  and  $\langle \alpha_{bar} \rangle = -0.94 \pm 0.02$ , so the average spectral index is reduced by  $-0.18$ . The downstream region shows a lower flux density and spectral index than both the main shock and the filament.

Fig. 6.11 highlights the presence of two distinct synchrotron emitting structures, in agreement with a second shock surface model. The substructure could also be due to the adiabatic compression induced by a secondary shock, which increases the maximum synchrotron frequency emitted by a population of fossil electrons by a multiple of the compression factor, although the boosting which is usually observed in this case is moderate (factor of  $\sim 2$ ), and the scenario has been ruled out for most cases of shocks (Hoang et al., 2018).

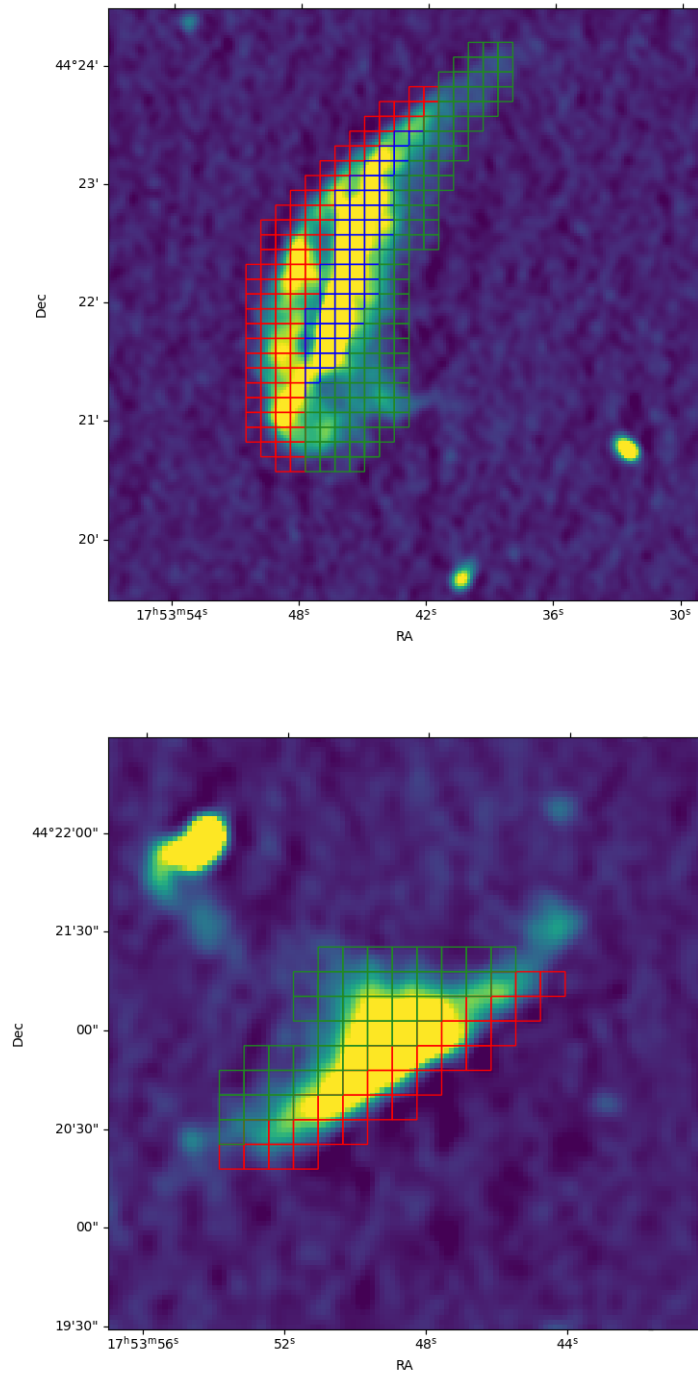


**Figure 6.10:** Zoom in view on the NE and SW radio relic, with selected regions for the curvature study overlaid in different colors. The three components of the NE relic were divided as follows: in *red* we outlined the position of the *outer edge*, in *blue* we followed the *bright bar*, while in *green* we selected the downstream regions. In a similar manner, the shock front and the downstream regions were selected along the SW relic. The same colors are used to represent the structures in the following plots.

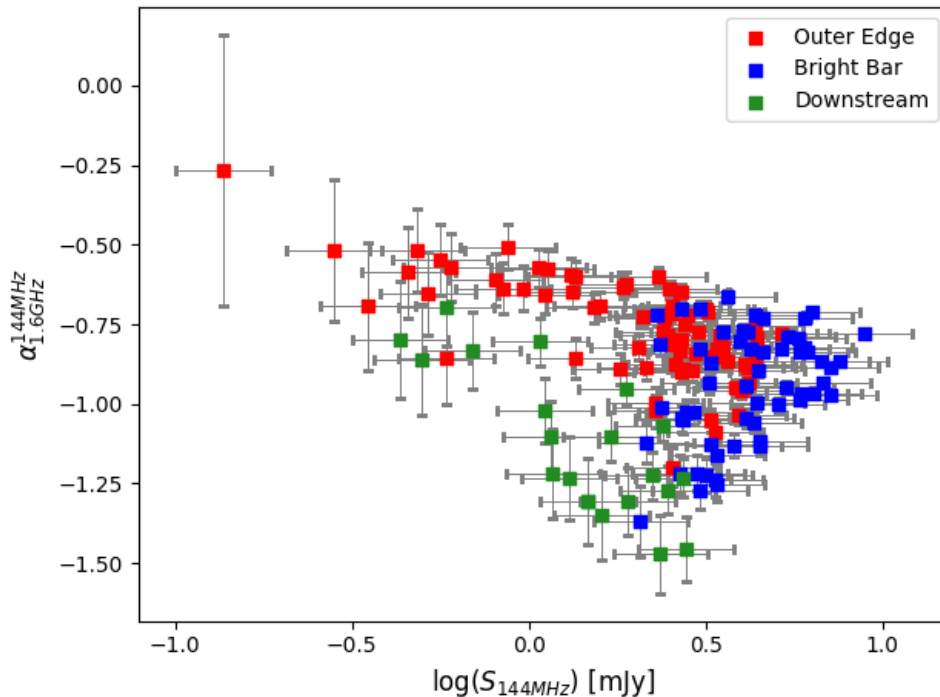


**Figure 6.11:** Spectral index against LOFAR 144 MHz flux density plot. The spectral index was calculated between LOFAR 144 MHz and JVLA 1.6 GHz data to leverage on the broadest available frequency range. The two substructures of the NE relic can be recognized in the plot thanks to the high resolution of the images.

## 6.4 Spectral curvature

As merger-shock models predict increasing spectral curvature in post-shock regions, considering the peculiar structure of the relics of MACS J1752+4440, we have analyzed the curvature of the relics spectra.

We employed the color-color diagram technique (Rudnick et al., 1994; van Weeren et al., 2012) which consists in comparing the spectral index calculated between a low (LOFAR 144 MHz - uGMRT Band 3 416 MHz) and high (uGMRT Band 4 650 MHz - JVLA 1.6 GHz) frequency range, calculated in the same regions. Color-color diagrams provide information about the curvature of the spectrum, and thus on particle ageing, by comparing the position of the points with respect to a perfect power-law line (i.e. injection spectrum), which corresponds to  $\alpha_{\nu_2}^{\nu_1} = \alpha_{\nu_4}^{\nu_3}$ .

Using the same boxes generated in Fig. 6.10, we calculated the spectral index and its uncertainty as in Eq. 6.3 and Eq. 6.4. This operation was done considering only the boxes in which the integrated flux density was above  $3\sigma_{rms}$  in all images simultaneously. The color-color plots for both relics can be seen in Fig. 6.12.

Surprisingly, the high-resolution color-color plots show an inverted curvature with

respect to ageing models. This kind of “concave” curvature implies that, at higher frequencies, we observe a flatter spectrum, which holds for higher energetic particles with respect to the expected behaviour. In these plots, a JP model with injection spectrum of  $-0.5$  (Jaffe and Perola, 1973) was plotted together with the observed curvature points. The JP model assumes a single burst of particle acceleration and an isotropic angle between the magnetic field and the electron velocity vectors (the so-called pitch angle), on a timescale shorter than the radiative timescale. It is commonly used for post-shock regions, assuming a planar shock front, observed perfectly edge-on. Clearly, the observed curvature points are not represented by the JP model. Other models are present, which take into account a slight inclination along the LoS for the shock front (i.e. KGJP), but as the trend is similar to the one produced by the JP model, and since we see no sign of particle ageing, we decided to not plot them. In order to better investigate the spatial distribution of the curved spectra in the relics, we generated a high-resolution spectral curvature map. The spectral curvature map can be generated using data at four frequencies, as:

$$\text{SC} = -\alpha_{\nu_2}^{\nu_1} + \alpha_{\nu_4}^{\nu_3}, \quad (6.10)$$

with an uncertainty on each pixel of

$$\Delta\text{SC} = \sqrt{(\Delta\alpha_{\nu_2}^{\nu_1})^2 + (\Delta\alpha_{\nu_4}^{\nu_3})^2}. \quad (6.11)$$

The spectral curvature map we obtained can be seen in Fig. 6.13. This map shows that the NE relic has many points in which the curvature has a positive value, with a typical value of  $\sim +0.2$ , which represents a concave spectrum, opposite to the one predicted by any aging model. These points also resemble the substructures that are visible in the high-resolution images of the cluster, suggesting that the regions that generate the “concave” spectrum are related to the *outer edge* and the *bright bar* substructure. The SW relic, instead, shows a gradient of curvature along the relic main axis, having negative curvature at the center of the relic, but positive at its extremes. This kind of flattening trend in synchrotron spectra is not reproduced by any kind of particle aging model.

Rajpurohit et al. (2021) showed how this kind of “concave” spectrum in color-color plots of radio relics could be due to projection effects, by simulating the same color-color plot on a relic seen at different angles. Therefore, the observed result might be influenced by the angle with which these structures are observed. Meanwhile,

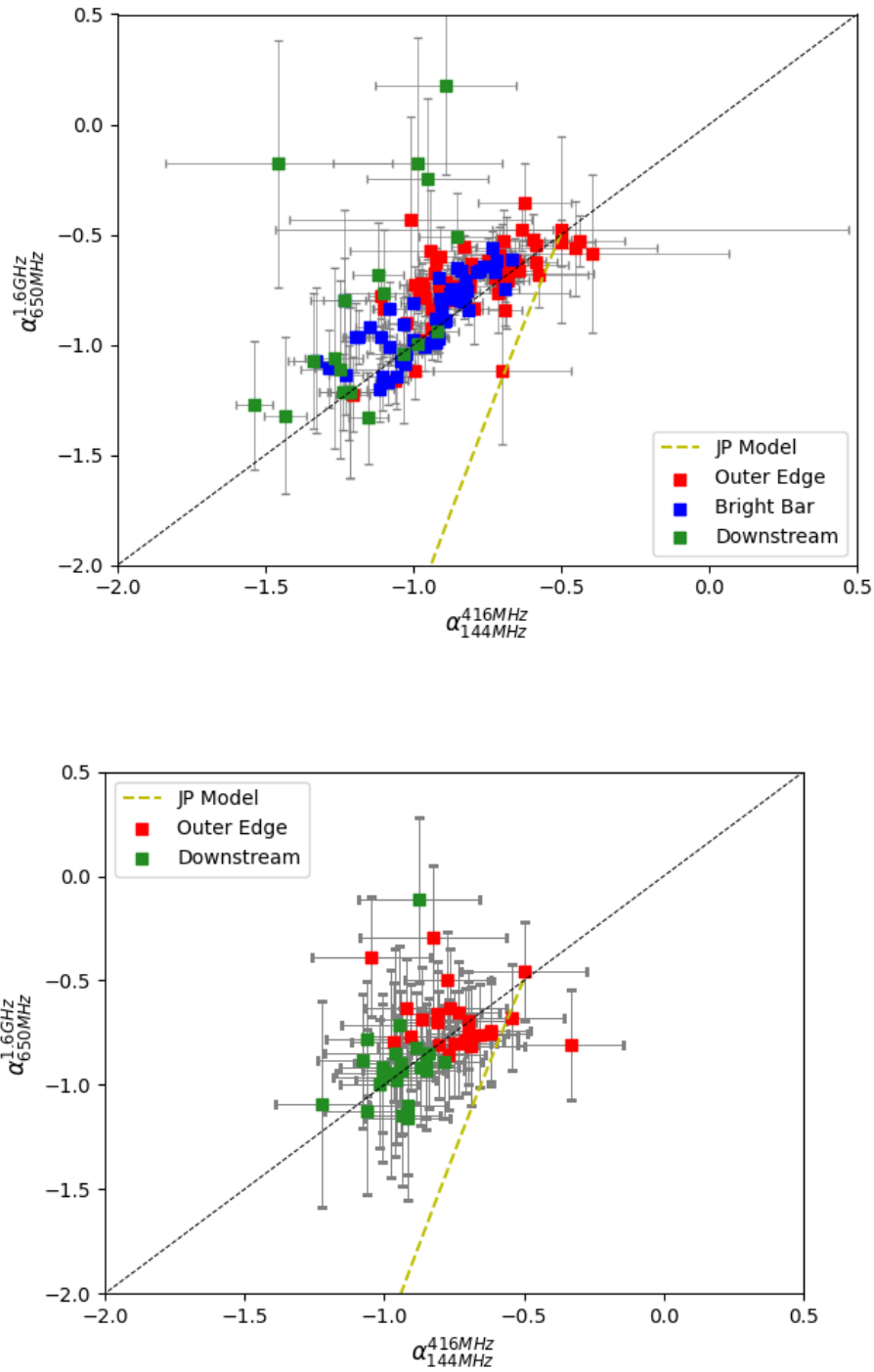


**Figure 6.12:** Color-color plot of both radio relics at high-resolution. *Top:* the NE relic shows a lack of points below the power-law line, which indicates a mostly power-law spectrum, with points appearing in the “concave” spectrum region. The coloring shows how the *outer edge* and the *bright bar* both fall mostly on the power-law line, with no sign of spectral steepening. *Bottom:* the SW relic displays some steepening in points at lower spectral index, but still presents multiple points representing a flattening spectrum.

as the color-color plots show no sign of ageing, it is likely that either the angle of the shock front was not small, or other effects, not taken into account into spectral aging model, are in action. For instance, the assumption of multiple shock surfaces or magnetic field compression are not considered in JP (and KGJP) models. Furthermore, although it has been shown by simulations that radio relics are best observed in cluster mergers whose collision axis is aligned with the plane of the sky, and considering the possible influence of the magnetic field in the shape of the NE relic, these new discoveries prompted our follow up study on polarization. Indeed, the observe polarized emission could be affected by the presence of substructures overlapping along the line of sight (see Chap. 6.5).

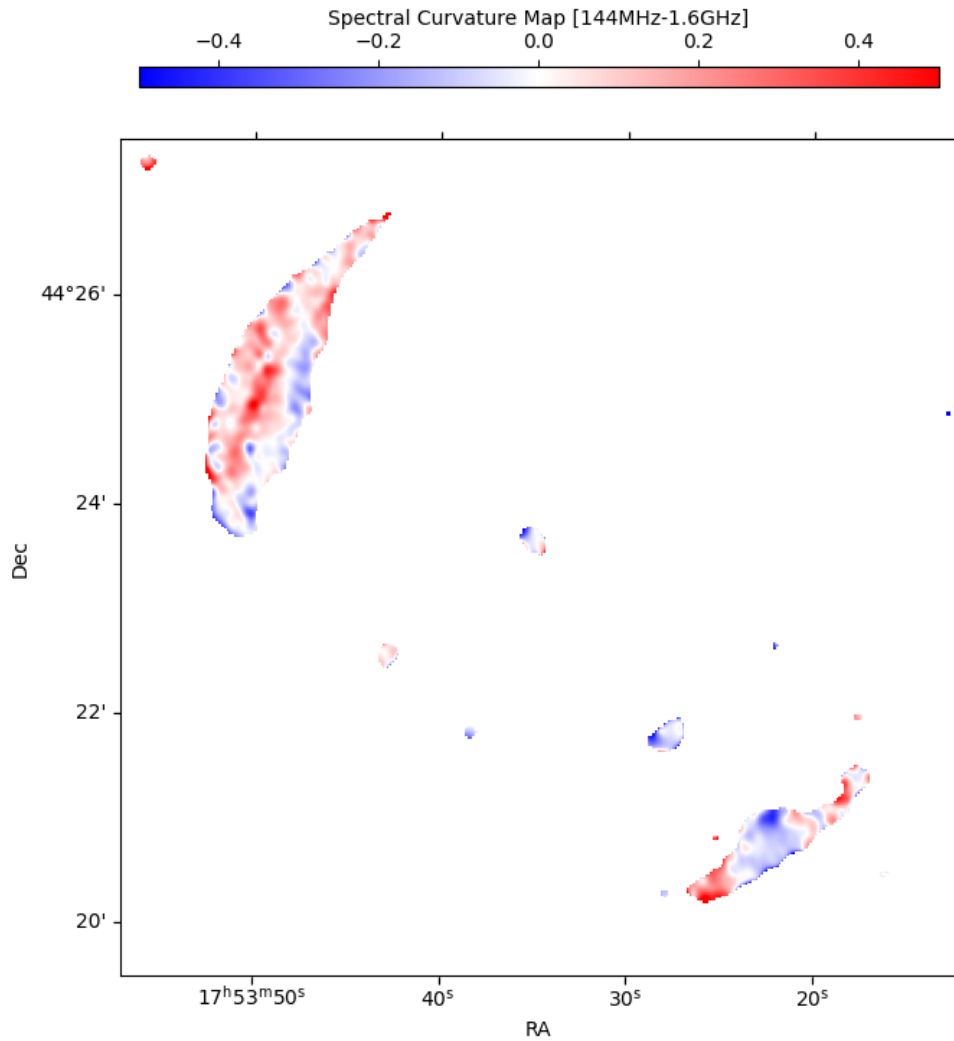


**Figure 6.13:** Spectral curvature map of MACS J1752+4440. The spectral curvature was calculated between 144 MHz and 1.6 GHz. The map shows a typical value of  $\sim +0.2$  and does not show a uniform negative curvature, as it would be expected. The NE relic shows a strongly positive curvature along its substructure, with negative curvature appearing downstream. The SW relic instead shows a gradient in spectral curvature along its major axis. The spectral curvature error map is present in [APPENDIX A](#).

## 6.5 Polarization

The synchrotron emission is linearly polarized. For an optically thin source, considering a homogeneous distribution of relativistic electrons with a power-law spectrum  $N(E)dE \propto E^{-\delta}dE$ , the degree of intrinsic linear polarization is calculated as:

$$p_{int} = \frac{3\delta + 3}{3\delta + 7}. \quad (6.12)$$

In radio relics, the intrinsic polarization degree can reach up to  $\sim 60\%$  (Ensslin et al., 1998), although, in practice, the observed polarization degree is often smaller due to different effects. One of these effects, of particular interest for our study, is the Faraday depolarization effect.

The polarization of an electromagnetic wave is described through the Stokes parameters (I, Q, U, V), representing the orientation of the wave electric field. In radio interferometry, the signals between antennas are cross-correlated, and the Stokes parameters are calculated through the right and left circular polarization of the electromagnetic wave. Thanks to the Stokes parameters, it is possible to define the linear polarization P as:

$$P = pIe^{2i\chi} = Q + iU, \quad \text{with} \quad |P| = \sqrt{Q^2 + U^2}, \quad (6.13)$$

where

$$\chi = \frac{1}{2} \arctan \frac{U}{Q} \quad (6.14)$$

is the observed polarization angle. When an electromagnetic wave passes through a magnetized, ionized medium, the Faraday rotation effect rotates the polarization angle as a function of frequency, due to the phase shift of the right and left circular polarization, composing a linearly polarized wave. Therefore, traveling along a cluster path length, the intrinsic polarization angle  $\chi_{int}$  will be rotated by an angle, typically written in terms of the rotation measure  $RM$ , as:

$$\chi_{obs} = \chi_{int} + \Delta\chi = \chi_{int} + RM\lambda^2, \quad (6.15)$$

where  $RM$  is proportional to the electron density  $n_e$  and the LoS component of the magnetic field  $B_{||}$  (Burn, 1966), as

$$RM = k \int_{LoS} n_e B_{||} dl. \quad (6.16)$$

In a radio source, the observed polarization intensity can be significantly lower with respect to the intrinsic value, if differential Faraday rotation, or beam depolarization, occur. In fact, along the LoS, the radio emission can arise from different depths and undergo different Faraday rotation, due to the different path length and regions with different magnetic fields and gas density. Moreover, in the case of a turbulent magnetic field, different turbulent cells might be within the synthesised telescope beam, generating beam depolarization. The sum of these effects results in a reduction of the observed polarization degree. Both effects can be described by:

$$P = pe^{-2\sigma_{RM}^2\lambda^4} e^{2i(\chi_{int}+RM\lambda^2)}, \quad (6.17)$$

where  $\sigma_{RM}$  is the dispersion of the RM across the source on the sky (O’Sullivan et al., 2012).

The positive spectral curvature can be explained by different relic substructures seen in projection, considering the cluster merger axis to not be perfectly aligned with the plane of the sky, but having a slight inclination along the LoS. The presence of these substructures could also leave imprints on the observed fractional polarization, as the filamentary structure, and a possible inclination angle, might increase the Faraday depolarization of the *bright bar* and of the downstream.

We produced polarization images as described in Chap. 5.1.3 at  $5'' \times 4.5''$  resolution, of all Stokes parameters, combining the three B, C and D configurations of JVLA. Using the Q and U images, we produced the Polarization Intensity map  $P$ , computing the module of the polarization intensity as in the right side of Eq. 6.13 and the polarization angle map through Eq. 6.14. When computing  $P$ , we corrected for the Ricean bias which induces a positive “floor” to the polarization intensity image, due to the positivity of the noise in polarization (Eq. 6.13, left). The correction for the Ricean bias was suggested by Wardle and Kronberg (1974), in which  $P$  is corrected by performing the sum of squares between  $P$  and the noise  $\sigma_{rms,QU}$ , average noise between the Q and U image, as

$$P = \sqrt{P^2 - \sigma_{rms,QU}^2}. \quad (6.18)$$

After computing  $P$ , we obtained the Polarization Fraction  $p$  map as

$$p = \frac{P}{I}, \quad (6.19)$$

where I is the Stokes I image. All of the produced images can be seen in Fig. 6.14.

The polarization intensity map shows the two relics as a combination of the emission coming from the Stokes Q and U parameters. It is notable how the NE relic shows two distinct structures resembling the *outer edge* and the *bright bar* substructure, while the SW relic has the same shape of its Stokes I emission, with smaller size. The peak of the SW relic coincides with the peak of the emission in the Stokes I image, centered with respect to the position of the shock. The polarization fraction image follows the same shapes, with values following a uniform value of  $\sim 0.2 - 0.4$ . Although radio relics are thought to be highly polarized sources, the obtained values are in line with several observations of other radio relics (i.e. Stuardi et al., 2019).

As the NE relic consists of two main substructures, we wanted to check if this composition, together with possible magnetic and projection effects, left any imprint on the polarized emission. To do it, we investigated the profile of the polarization fraction along the same elliptical-arc regions generated for the spectral index analysis in Chap. 6.2. Fig. 6.15 shows the fractional polarization profile, which has a peak of polarization fraction in region 1, along the *outer edge*, and shows a second peak in region 4, at the position of the *bright bar*. This second peak can be interpreted as a higher polarization fraction due to the presence of the substructure (i.e. the *bright bar*).

As described by Eq. 6.17, in the case in which the positive spectral curvature is due to projection effects, the angle with respect to the LoS could change the observed polarization fraction of the relics, as more (or less) magnetized medium could be present along the LoS and increase (or decrease) the Faraday depolarization and beam depolarization effects. Therefore, assuming the presence of projection effects, by comparing the spectral curvature and the polarization fraction, calculated along the same regions, one could expect to observe a trend between the two quantities.

Starting from the polarization intensity and the Stokes I images, we calculated the spectral curvature and the polarization fraction on the same boxes that were generated for the color-color plot analysis in Chap. 6.4. The produced plot, in Fig. 6.16, displays no significant trend, as many of the spectral curvature points are located around  $\sim 0.2$ , while the polarization fraction ranges between 0.05 and 0.45. In this plot, the polarization fraction was calculated considering both boxes

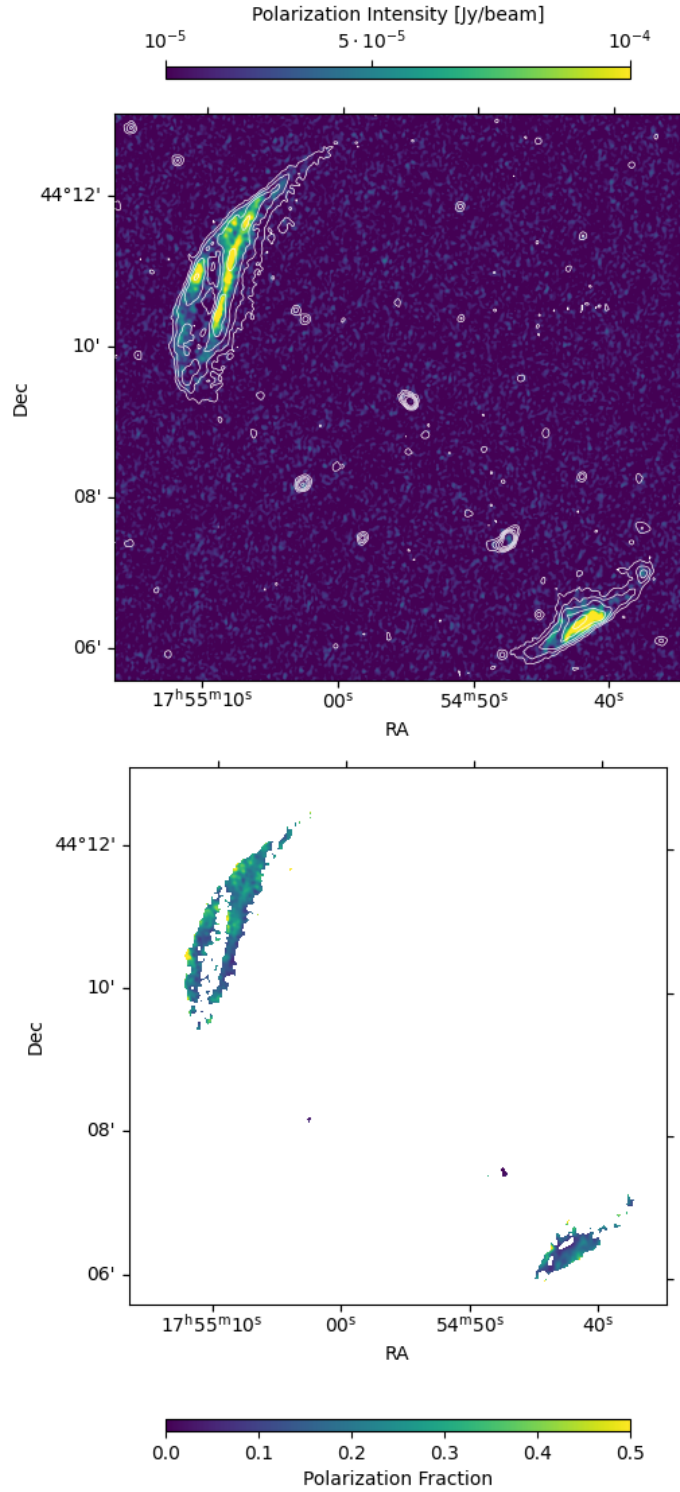


**Figure 6.14:** *Top:* Polarization Intensity image. The image shows polarized emission coming from the two substructures which compose the NE relic. Contours are drawn from the Stokes I image, straging at  $3\sigma$  and separated by powers of 2. *Bottom:* Polarization fraction image, showing that the two substructures of the NE relic have a similar fractional polarization, together with the SW relic. The polarization fraction ranges from  $\sim 20\%$  to  $\sim 40\%$  in both radio relics.

in which the polarization intensity was above and below  $2\sigma_{rms,QU}$ . Following this approach, points below the threshold are indicated as downward arrows and are to be considered as upper limits. We are then unable to say if projection effects are responsible for the observed trend of the polarization fraction.

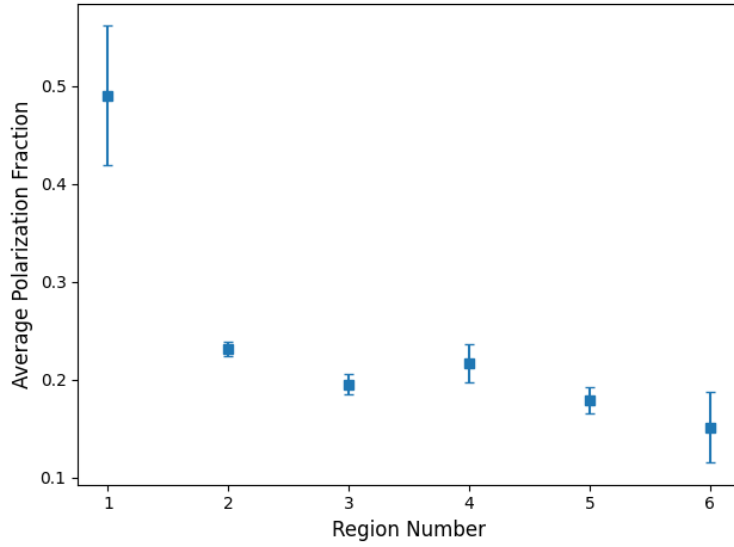


**Figure 6.15:** Fractional polarization profile. The polarization fraction was calculated along the same elliptical arc regions generated for the spectral index analysis.

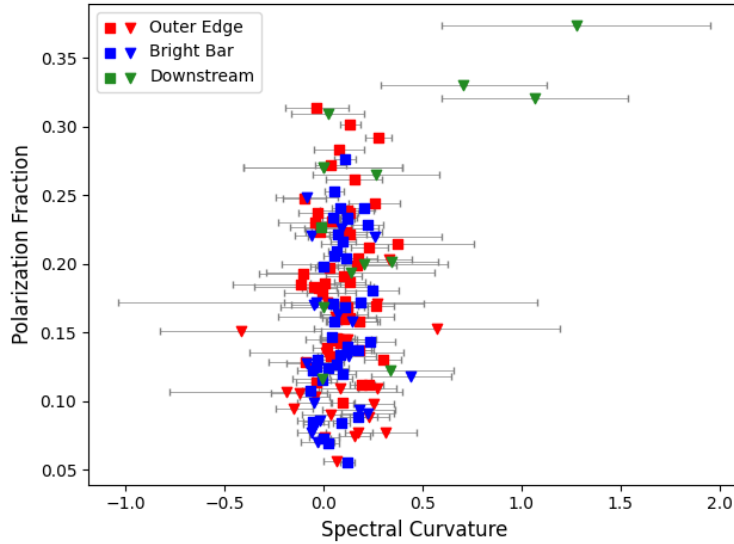


**Figure 6.16:** Fractional polarization against spectral curvature plot. As expected from the SC map, most points are located around a spectral curvature of  $\sim +0.2$ , while the fractional polarization ranges from 0.05 to 0.45 without showing any particular trend. Points are colored following the distribution of boxes as explained in previous chapters. Downward arrows are to be intended as upper limits, as they represent points in which the polarization intensity was below  $2\sigma_{rms}$ .

**Table 6.3:** Equipartition magnetic field parameters.

	$\alpha$	$\nu_0$ [MHz]	$\xi(\alpha, \nu_1, \nu_2)$	k	z	$I_0$ [ $\frac{\text{Jy}}{\text{arcsec}^2}$ ]	d [kpc]
NE	0.91	144	$6.77 \cdot 10^{-13}$	1	0.366	0.040	867.5
SW	0.83	144	$8.75 \cdot 10^{-13}$	1	0.366	0.046	552.5

## 6.6 Physical parameters

We estimated the strength of the magnetic field in the two radio relics through the minimum energy conditions (Burbidge, 1956). Govoni and Feretti (2004) expressed minimum energy through observable quantities as:

$$u_{min} \left[ \frac{\text{erg}}{\text{cm}^3} \right] = \xi(\alpha, \nu_1, \nu_2) (1+k)^{4/7} \left( \frac{\nu_0}{\text{MHz}} \right)^{4\alpha/7} (1+z)^{(12+4\alpha)/7} \times \quad (6.20)$$

$$\times \left( \frac{I_0}{\left[ \frac{\text{mJy}}{\text{arcsec}^2} \right]} \right)^{4/7} \left( \frac{d}{\text{kpc}} \right)^{-4/7}, \quad (6.21)$$

where  $I_0$  is the source brightness at the central frequency  $\nu_0$  and d is the source depth, calculated as the average between the length and the width of the two relics on the plane of the sky. We chose  $\alpha$  to be the injection spectral index calculated on region 1, along the main shock for both radio relics, and the  $\xi(\alpha, \nu_1, \nu_2)$  constant was then chosen to be representative of that spectral index (see Govoni and Feretti, 2004). The  $k$  constant represents the ratio of energy between relativistic protons and electrons and depends on the mechanism of generation of relativistic particles, which is yet not fully known. Therefore, we chose  $k = 1$  as commonly done in the literature. A summary of the assumed values is in Tab. 6.3.

The equipartition magnetic field was then obtained as:

$$B_{eq} = \left( \frac{24\pi}{7} u_{min} \right)^{1/2}. \quad (6.22)$$

We obtain two similar values between the two radio relics of:

$$B_{eq,NE} = 0.95 \mu\text{G} \quad (6.23)$$

$$B_{eq,SW} = 1.1 \mu\text{G}, \quad (6.24)$$

calculated using the LOFAR 144 MHz source brightness on the low-resolution image. Both the measurement are in the order of the  $\mu\text{G}$ , a value which is commonly found

while studying equipartition magnetic fields in galaxy clusters. The field calculated on the three remaining frequencies give compatible results.

# Chapter 7

## Conclusions and future perspective

In this thesis, we presented a radio continuum study of the double-relic, merging cluster MACS J1752+4440. The cluster was studied by [van Weeren et al. \(2012\)](#) and [Bonafede et al. \(2012\)](#) through WSRT, GMRT and VLA data (Chap. 3). These works detected the double-relic system and characterized its spectral and polarization properties, though limited by the low resolution of the observations.

The goal of this thesis was to study the same double-relic system, making use of the new generation of radio interferometers, with better sensitivity and a wider frequency band. We used LOFAR (144 MHz), new uGMRT at 416 MHz and 650 MHz and JVLA (1.6 GHz) data to obtain new high-resolution images of the cluster at 7'' and low-resolution images at 20'', reaching unprecedented details.

Thanks to the high resolution images, we were able to detect substructures along the NE relic (Fig. 5.1), namely a *outer edge* at the position of the merger shock and a *bright bar*, central with respect to the width of the relic.

To understand the origin of these structures, we produced new brightness profiles (Fig. 6.5), showing how the emission from the NE relic peaks at the position of the *bright bar* substructure, with a secondary peak along the *outer edge*, at the location of the merger shock.

We measured an integrated flux density at 144 MHz of  $S_{144}^{NE} = 530 \pm 50$  mJy for the NE relic and  $S_{144}^{SW} = 177 \pm 18$  mJy for the SW relic, and a radio power of  $P_{144}^{NE} = 2.40 \times 10^{26}$  WHz<sup>-1</sup> and  $P_{144}^{SW} = 7.90 \times 10^{25}$  WHz<sup>-1</sup>, compatible with literature studies of radio relics ([Botteon et al., 2020](#)). We find the integrated spectral

index for the two relics at  $\alpha_{int}^{NE} = -0.91 \pm 0.06$  and  $\alpha_{int}^{SW} = -0.83 \pm 0.05$  (Fig. 6.7). Surprisingly, both these spectral indexes are  $\alpha_{int} > -1$ , in contrast with basic DSA predictions about particle acceleration and different from literature studies.

We produced a spectral index map at high-resolution (Fig. 6.3), showing how the spectral index for the NE relic follows the same structures of the radio brightness emission. This was never observed before for this cluster due to resolution limitations, and cannot be explained by a simple, single shock model. We analyzed the trend of the spectral index on both relics by generating spectral index profiles (Fig. 6.6), observing a linearly decreasing profile for the SW relic, as we would expect from particle aging, while the NE relic shows a complex profile, with flattest spectral index at the region along the merger shock, but a second flattening at the position of the *bright bar*. This behavior is unexpected in the scenario in which relics are generated by a single merger shock surface. Furthermore, we observe a constantly flatter profile at higher frequencies, which is in opposition with particle aging. At low resolution, the spectral index profile of the SW relic shows a peculiar feature, in which the low-frequency profile flattens in the most central region, at the position of the downstream (Fig. 6.7). We suggest that this flattening is due to the presence of a nearby cluster radio source, which radio emission generates a “bridge” between the source and the SW relic (Fig. 6.8).

We conclude that the observed *bright bar* filament and its imprint on the surface brightness and spectral index profiles could be due to projection effects of a double shock front observed in projection. Wittor et al. (2017) showed how the same structures could be generated by fluctuating a Mach number distribution inside the relic structure, by changes in the particle acceleration efficiency or by a complex magnetic field structure, being compressed by the merger shock.

Under DSA assumptions, we calculated the radio Mach numbers for both relics. As both integrated spectral indices were  $\alpha_{int} > -1$ , the integrated Mach number could not be calculated through DSA equations. Therefore, we calculated the injection Mach numbers by assuming, as injection spectral index, the one calculated on the region overlaying the *outer edge*. We measure two Mach numbers of  $3.12_{-0.42}^{+0.82}$  and  $\mathcal{M} = 4.19_{-0.50}^{+0.94}$  for the NE and SW relic, respectively (see Tab. 6.2). Shocks with Mach numbers like the one of the SW relic are extremely rare events. Cosmological simulations (Vazza et al., 2019; Bykov et al., 2019) show

that, even though they are possible, the Mach number should vary greatly along the merger shock. If this happens, the radio calculated Mach number would be overestimated, as synchrotron luminosity strongly increases with Mach number.

Considering the observed surface brightness profile, and the trend on the spectral index, for the NE relic, we discuss the possibility of explaining such evidences through a complex shock structure. [Markevitch et al. \(2005\)](#) has shown that particle re-acceleration, due to a second shock surface, can flatten the spectra of the particle population, in case in which the fossil plasma had a steeper spectrum before the shock. This scenario could explain the observed integrated spectral indices, the shape of the surface brightness profile and the flatter spectra at higher frequencies observed in the spectral index profile. If this assumption holds, we would expect to observe two or more distinct radio emitting particle populations. To check this, we plotted the spectral index calculated between LOFAR 144 MHz and JVLA 1.6 GHz against the LOFAR flux (Fig. 6.11), observing two distinct trends linked to the *outer edge* and the *bright bar* substructure, in agreement with our proposed scenario.

Merger-shock models predict increasing spectral curvature in post-shock regions. To check on the curvature of the relics, considering the NE relic substructures, we generated color-color plots (Fig. 6.12). We observe how, for both radio relics, the spectral curvature is almost perfectly represented by a power-law trend, in which the spectral index at high and low frequency are equal. Interestingly, many points fall in the “concave” part of the spectrum, in which the high frequency spectral index is flatter than the low-frequency one, and they are not represented by any spectral aging model. [Rajpurohit et al., 2021](#) showed how this kind of trends in color-color plots could be represented by projection effects. We also calculated the spectral curvature map of the galaxy cluster (Fig. 6.13) and observed how the spectral curvature follows the substructures of the NE relic, with positive values (hence a “concave” spectrum) along the *bright bar* and the *outer edge*, in the NE relic. The SW relic shows a spectral curvature gradient along its longitudinal axis, a trend not reproduced by particle aging.

To inspect possible projection effects along the LoS, we produced polarization images through JVLA (1.6 GHz) polarization data. We generate polarization

intensity and polarization fraction maps (Fig. 6.14), detecting polarized emission coming from the same substructures along the NE relic. The polarization fraction spans from  $\sim 20\%$  to  $\sim 40\%$ . Using the same elliptical arc regions, we investigated the trend of the polarization fraction for the NE relic (Fig. 6.15), highlighting the presence of a flat profile of the polarization fraction along the regions of the *bright bar*. Considering possible projection effects, we investigated the trend of the polarization fraction against the spectral curvature, calculated on the same regions. If projection was in action, we could expect to observe a trend between these two properties. However, Fig. 6.16 shows no trend between the two quantities. We note that the study of the polarization and depolarization could be better conducted with techniques, like the RM synthesis, Taking into account bandwidth depolarization and multiple emitting components.

Using the assumption of equipartition, we calculate the equipartition magnetic field with both radio relics, obtaining a compatible result of  $B_{eq} \sim 1\mu\text{G}$ .

In summary, this thesis works confirmed the presence of sub-structures in radio relics of MACSJ 1752+4440 and proposed a scenario able to explain the observed brightness and spectral trends. From the spectral curvature study, we conclude that the observation could be dominated by several effects: projection effects could explain the concave curvature observed on both relic, while a complex magnetic structure could explain the enhanced brightness and flatter spectra at the location of the *bright bar*.

Future prospects include the study of the radio halo component, which was excluded in this thesis, and an in depth RM-synthesis analysis to quantify the expected Faraday rotation on radio relics.

# APPENDIX A

In Fig. 7.1 we show the spectral curvature uncertainty map. We note that the uncertainty values are low across the whole relics surface, with peaks at their outer edges. In Fig. 7.2 and Fig. 7.3 we show the integrated spectral index error maps. These errors are calculated as the error of the `polyfit` function, pixel per pixel, and are uniform along the two relics, but higher at the relics' edge.

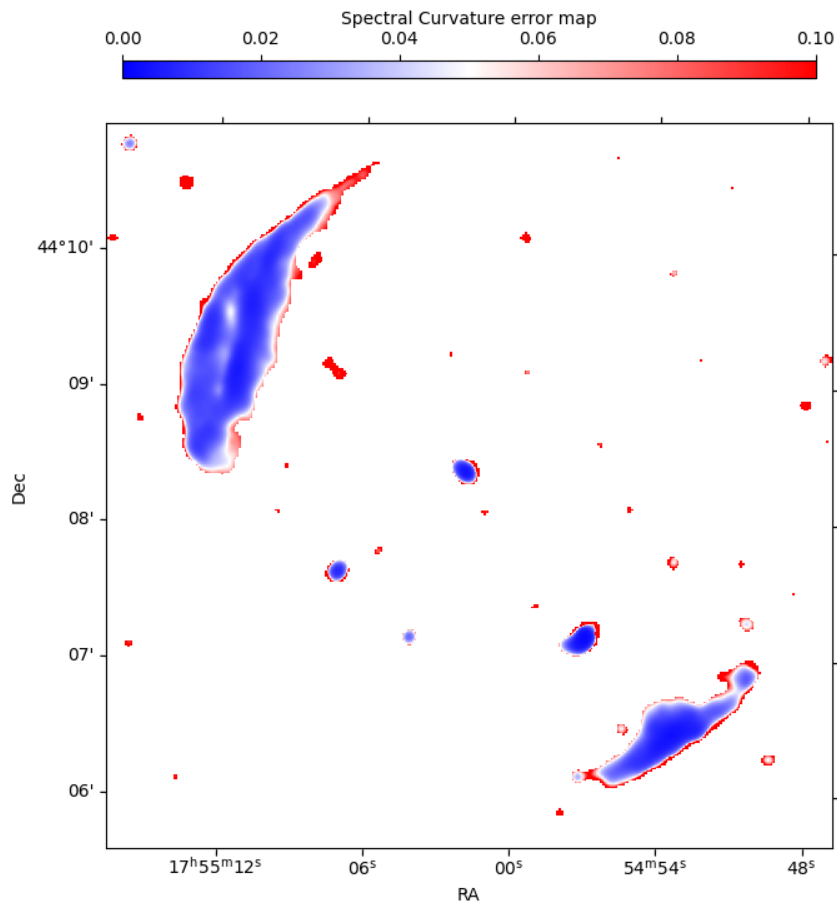


**Figure 7.1:** Spectral curvature error map.

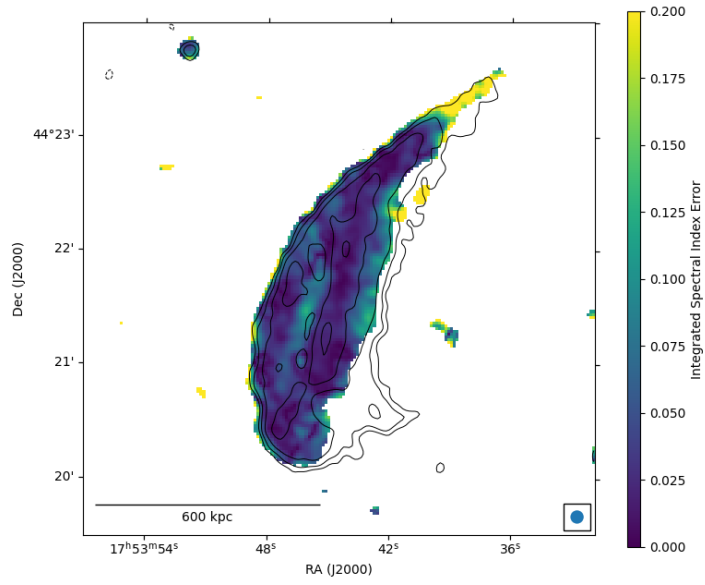


**Figure 7.2:** NE relic integrated spectral index error map.

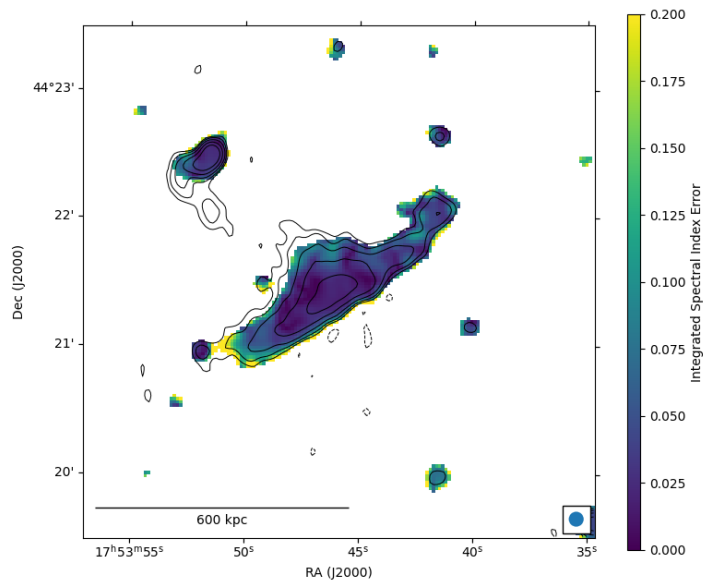


**Figure 7.3:** SW relic integrated spectral index error map.

# Bibliography

- [1] R. Adam, A. Adane, P. A. R. Ade, P. André, A. Andrianasolo, H. Aussel, A. Beelen, A. Benoît, A. Bideaud, N. Billot, O. Bourrion, A. Bracco, M. Calvo, A. Catalano, G. Coiffard, B. Comis, M. De Petris, F. X. Désert, S. Doyle, E. F. C. Driessen, R. Evans, J. Goupy, C. Kramer, G. Lagache, S. Leclercq, J. P. Leggeri, J. F. Lestrade, J. F. Macías-Pérez, P. Mauskopf, F. Mayet, A. Maury, A. Monfardini, S. Navarro, E. Pascale, L. Perotto, G. Pisano, N. Ponthieu, V. Revéret, A. Rigby, A. Ritacco, C. Romero, H. Roussel, F. Ruppin, K. Schuster, A. Sievers, S. Triqueneaux, C. Tucker, and R. Zylka. The NIKA2 large-field-of-view millimetre continuum camera for the 30 m IRAM telescope. *A&A*, 609:A115, January 2018. doi: 10.1051/0004-6361/201731503.
- [2] H. Akamatsu, M. Mizuno, N. Ota, Y. Y. Zhang, R. J. van Weeren, H. Kawahara, Y. Fukazawa, J. S. Kaastra, M. Kawaharada, K. Nakazawa, T. Ohashi, H. J. A. Röttgering, M. Takizawa, J. Vink, and F. Zandanel. Suzaku observations of the merging galaxy cluster Abell 2255: The northeast radio relic. *A&A*, 600:A100, April 2017. doi: 10.1051/0004-6361/201628400.
- [3] Steven W. Allen, August E. Evrard, and Adam B. Mantz. Cosmological Parameters from Observations of Galaxy Clusters. *ARA&A*, 49(1):409–470, September 2011. doi: 10.1146/annurev-astro-081710-102514.
- [4] M. G. Baring. Diffusive Shock Acceleration : the Fermi Mechanism. page 97, January 1997. doi: 10.48550/arXiv.astro-ph/9711177.
- [5] Anthony Raymond Bell. Particle Acceleration by Shocks in Supernova Remnants. *Brazilian Journal of Physics*, 44(5):415–425, October 2014. doi: 10.1007/s13538-014-0219-5.
- [6] Roger Blandford and David Eichler. Particle acceleration at astrophysical

- shocks: A theory of cosmic ray origin. *Phys. Rep.*, 154(1):1–75, October 1987. doi: 10.1016/0370-1573(87)90134-7.
- [7] A. Bonafede, M. Brüggen, R. van Weeren, F. Vazza, G. Giovannini, H. Ebeling, A. C. Edge, M. Hoeft, and U. Klein. Discovery of radio haloes and double relics in distant MACS galaxy clusters: clues to the efficiency of particle acceleration. *MNRAS*, 426(1):40–56, October 2012. doi: 10.1111/j.1365-2966.2012.21570.x.
- [8] A. Bonafede, H. T. Intema, M. Brüggen, M. Girardi, M. Nonino, N. Kantharia, R. J. van Weeren, and H. J. A. Röttgering. Evidence for Particle Re-acceleration in the Radio Relic in the Galaxy Cluster PLCKG287.0+32.9. *ApJ*, 785(1):1, April 2014. doi: 10.1088/0004-637X/785/1/1.
- [9] A. Bonafede, M. Brüggen, D. Rafferty, I. Zhuravleva, C. J. Riseley, R. J. van Weeren, J. S. Farnes, F. Vazza, F. Savini, A. Wilber, A. Botteon, G. Brunetti, R. Cassano, C. Ferrari, F. de Gasperin, E. Orrú, R. F. Pizzo, H. J. A. Röttgering, and T. W. Shimwell. LOFAR discovery of radio emission in MACS J0717.5+3745. *MNRAS*, 478(3):2927–2938, August 2018. doi: 10.1093/mnras/sty1121.
- [10] A. Botteon, F. Gastaldello, G. Brunetti, and D. Dallacasa. A shock at the radio relic position in Abell 115. *MNRAS*, 460(1):L84–L88, July 2016. doi: 10.1093/mnrasl/slw082.
- [11] A. Botteon, T. W. Shimwell, A. Bonafede, D. Dallacasa, G. Brunetti, S. Mandal, R. J. van Weeren, M. Brüggen, R. Cassano, F. de Gasperin, D. N. Hoang, M. Hoeft, H. J. A. Röttgering, F. Savini, G. J. White, A. Wilber, and T. Venturi. LOFAR discovery of a double radio halo system in Abell 1758 and radio/X-ray study of the cluster pair. *MNRAS*, 478(1):885–898, July 2018. doi: 10.1093/mnras/sty1102.
- [12] A. Botteon, G. Brunetti, D. Ryu, and S. Roh. Shock acceleration efficiency in radio relics. *A&A*, 634:A64, February 2020. doi: 10.1051/0004-6361/201936216.
- [13] A. Botteon, T. W. Shimwell, R. Cassano, V. Cuciti, X. Zhang, L. Bruno, L. Camillini, R. Natale, A. Jones, F. Gastaldello, A. Simionescu, M. Rossetti, H. Akamatsu, R. J. van Weeren, G. Brunetti, M. Brüggen, C. Groeneveld,

- D. N. Hoang, M. J. Hardcastle, A. Iagnesi, G. Di Gennaro, A. Bonafede, A. Drabant, H. J. A. Röttgering, M. Hoeft, and F. de Gasperin. The Planck clusters in the LOFAR sky. I. LoTSS-DR2: New detections and sample overview. *A&A*, 660:A78, April 2022. doi: 10.1051/0004-6361/202143020.
- [14] D. S. Briggs. High Fidelity Interferometric Imaging: Robust Weighting and NNLS Deconvolution. In *American Astronomical Society Meeting Abstracts*, volume 187 of *American Astronomical Society Meeting Abstracts*, page 112.02, December 1995.
- [15] Marcus Brüggen, Andrei Bykov, Dongsu Ryu, and Huub Röttgering. Magnetic Fields, Relativistic Particles, and Shock Waves in Cluster Outskirts. *Space Sci. Rev.*, 166(1-4):187–213, May 2012. doi: 10.1007/s11214-011-9785-9.
- [16] G. Brunetti. Matter and Energy in Clusters of Galaxies. 301:349, 2003.
- [17] G. Brunetti, G. Setti, L. Feretti, and G. Giovannini. Particle reacceleration in the Coma cluster: radio properties and hard X-ray emission. *MNRAS*, 320(3):365–378, January 2001. doi: 10.1046/j.1365-8711.2001.03978.x.
- [18] Gianfranco Brunetti and Thomas W. Jones. Cosmic Rays in Galaxy Clusters and Their Nonthermal Emission. *International Journal of Modern Physics D*, 23(4):1430007-98, March 2014. doi: 10.1142/S0218271814300079.
- [19] G. R. Burbidge. On Synchrotron Radiation from Messier 87. *ApJ*, 124:416, September 1956. doi: 10.1086/146237.
- [20] B. J. Burn. On the depolarization of discrete radio sources by Faraday dispersion. *MNRAS*, 133:67, January 1966. doi: 10.1093/mnras/133.1.67.
- [21] A. M. Bykov, F. Vazza, J. A. Kropotina, K. P. Levenfish, and F. B. S. Paerels. Shocks and Non-thermal Particles in Clusters of Galaxies. *Space Sci. Rev.*, 215(1):14, February 2019. doi: 10.1007/s11214-019-0585-y.
- [22] R. Cassano, M. Gitti, and G. Brunetti. A morphological comparison between giant radio halos and radio mini-halos in galaxy clusters. *A&A*, 486(3):L31–L34, August 2008. doi: 10.1051/0004-6361:200810179.

- [23] P. Chandra, A. Ray, and S. Bhatnagar. The Late-Time Radio Emission from SN 1993J at Meter Wavelengths. *ApJ*, 612(2):974–987, September 2004. doi: 10.1086/422675.
- [24] James O. Chibueze, Hiroki Akamatsu, Viral Parekh, Haruka Sakemi, Takumi Ohmura, Ruby van Rooyen, Takuya Akahori, Hiroyuki Nakanishi, Mami Machida, Tsutomu T. Takeuchi, Oleg Smirnov, Dane Kleiner, and Filippo M. Maccagni. MeerKAT’s view of double radio relic galaxy cluster Abell 3376. *PASJ*, 75:S97–S107, February 2023. doi: 10.1093/pasj/psac009.
- [25] J. J. Condon, W. D. Cotton, E. W. Greisen, Q. F. Yin, R. A. Perley, G. B. Taylor, and J. J. Broderick. The NRAO VLA Sky Survey. *AJ*, 115(5):1693–1716, May 1998. doi: 10.1086/300337.
- [26] James J. Condon and Scott M. Ransom. *Essential Radio Astronomy*. 2016.
- [27] B. Dennison. Formation of radio halos in clusters of galaxies from cosmic-ray protons. *ApJ*, 239:L93–L96, August 1980. doi: 10.1086/183300.
- [28] G. Di Gennaro, R. J. van Weeren, M. Hoeft, H. Kang, D. Ryu, L. Rudnick, W. Forman, H. J. A. Röttgering, M. Brüggen, W. A. Dawson, N. Golovich, D. N. Hoang, H. T. Intema, C. Jones, R. P. Kraft, T. W. Shimwell, and A. Stroe. Deep Very Large Array Observations of the Merging Cluster CIZA J2242.8+5301: Continuum and Spectral Imaging. *ApJ*, 865(1):24, September 2018. doi: 10.3847/1538-4357/aad738.
- [29] H. Ebeling, A. C. Edge, and J. P. Henry. MACS: A Quest for the Most Massive Galaxy Clusters in the Universe. *ApJ*, 553(2):668–676, June 2001. doi: 10.1086/320958.
- [30] A. C. Edge, H. Ebeling, M. Bremer, H. Röttgering, M. P. van Haarlem, R. Rengelink, and N. J. D. Courtney. The discovery of two distant, massive clusters of galaxies in the ROSAT All-Sky Survey. *MNRAS*, 339(4):913–924, March 2003. doi: 10.1046/j.1365-8711.2003.06270.x.
- [31] T. Enßlin, C. Pfrommer, F. Miniati, and K. Subramanian. Cosmic ray transport in galaxy clusters: implications for radio halos, gamma-ray signatures, and cool core heating. *A&A*, 527:A99, March 2011. doi: 10.1051/0004-6361/201015652.

- [32] T. A. Enßlin and Gopal-Krishna. Reviving fossil radio plasma in clusters of galaxies by adiabatic compression in environmental shock waves. *A&A*, 366: 26–34, January 2001. doi: 10.1051/0004-6361:20000198.
- [33] Torsten A. Ensslin, Peter L. Biermann, Ulrich Klein, and Sven Kohle. Shock Waves of the Large-Scale Structure Formation in the Universe. *arXiv e-prints*, art. astro-ph/9805367, May 1998. doi: 10.48550/arXiv.astro-ph/9805367.
- [34] Enrico Fermi. On the Origin of the Cosmic Radiation. *Physical Review*, 75 (8):1169–1174, April 1949. doi: 10.1103/PhysRev.75.1169.
- [35] Kyle Finner, Kim HyeongHan, M. James Jee, David Wittman, William R. Forman, Reinout J. van Weeren, Nathan R. Golovich, William A. Dawson, Alexander Jones, Francesco de Gasperin, and Christine Jones. Exemplary Merging Clusters: Weak-lensing and X-Ray Analysis of the Double Radio Relic, Merging Galaxy Clusters MACS J1752.0+4440 and ZWCL 1856.8+6616. *ApJ*, 918(2):72, September 2021. doi: 10.3847/1538-4357/ac0d00.
- [36] Alexis Finoguenov, Craig L. Sarazin, Kazuhiro Nakazawa, Daniel R. Wik, and Tracy E. Clarke. XMM-Newton Observation of the Northwest Radio Relic Region in A3667. *ApJ*, 715(2):1143–1151, June 2010. doi: 10.1088/0004-637X/715/2/1143.
- [37] M. Gendron-Marsolais, J. Hlavacek-Larrondo, R. J. van Weeren, T. Clarke, A. C. Fabian, H. T. Intema, G. B. Taylor, K. M. Blundell, and J. S. Sanders. Deep 230–470 MHz VLA observations of the mini-halo in the Perseus cluster. *MNRAS*, 469(4):3872–3880, August 2017. doi: 10.1093/mnras/stx1042.
- [38] N. Golovich, W. A. Dawson, D. M. Wittman, R. J. van Weeren, F. Andrade-Santos, M. J. Jee, B. Benson, F. de Gasperin, T. Venturi, A. Bonafede, D. Sobral, G. A. Ogrean, B. C. Lemaux, M. Bradač, M. Brüggen, and A. Peter. Merging Cluster Collaboration: A Panchromatic Atlas of Radio Relic Mergers. *ApJ*, 882(1):69, September 2019. doi: 10.3847/1538-4357/ab2f90.
- [39] Nathan Golovich, William A. Dawson, David M. Wittman, Myungkook J. Jee, Bryant Benson, Brian Lemaux, Reinout J. van Weeren, Felipe Andrade-Santos, David Sobral, Francesco de Gasperin, Marcus Bruggen, Marusa

- Bradac, Kyle Finner, and Annika Peter. Merging Cluster Collaboration: Optical and Spectroscopic Survey of a Radio-Selected Sample of Twenty Nine Merging Galaxy Clusters. *arXiv e-prints*, art. arXiv:1711.01347, November 2017. doi: 10.48550/arXiv.1711.01347.
- [40] Federica Govoni and Luigina Feretti. Magnetic Fields in Clusters of Galaxies. *International Journal of Modern Physics D*, 13(8):1549–1594, January 2004. doi: 10.1142/S0218271804005080.
- [41] Y. Gupta, B. Ajithkumar, H. S. Kale, S. Nayak, S. Sabhapathy, S. Suresh Kumar, R. V. Swami, J. N. Chengalur, S. K. Ghosh, C. H. Ishwara-Chandra, B. C. Joshi, N. Kanekar, D. V. Lal, and S. Roy. The upgraded GMRT: opening new windows on the radio Universe. *Current Science*, 113(4):707–714, August 2017. doi: 10.18520/cs/v113/i04/707-714.
- [42] S. E. G. Hales, C. R. Masson, P. J. Warner, and J. E. Baldwin. The 6C survey of radio sources - III. The zone 48<sup>h</sup>Dec<sup>j</sup>68, 05<sup>h</sup>25<sup>m</sup>RA<sup>j</sup>18<sup>h</sup>17. *MNRAS*, 246: 256–262, September 1990.
- [43] M. J. Hardcastle, G. Gürkan, R. J. van Weeren, W. L. Williams, P. N. Best, F. de Gasperin, D. A. Rafferty, S. C. Read, J. Sabater, T. W. Shimwell, D. J. B. Smith, C. Tasse, N. Bourne, M. Brienza, M. Brügger, G. Brunetti, K. T. Chyży, J. Conway, L. Dunne, S. A. Eales, S. J. Maddox, M. J. Jarvis, E. K. Mahony, R. Morganti, I. Prandoni, H. J. A. Röttgering, E. Valiante, and G. J. White. LOFAR/H-ATLAS: a deep low-frequency survey of the Herschel-ATLAS North Galactic Pole field. *MNRAS*, 462(2):1910–1936, October 2016. doi: 10.1093/mnras/stw1763.
- [44] D. N. Hoang, T. W. Shimwell, R. J. van Weeren, H. T. Intema, H. J. A. Röttgering, F. Andrade-Santos, H. Akamatsu, A. Bonafede, G. Brunetti, W. A. Dawson, N. Golovich, P. N. Best, A. Botteon, M. Brügger, R. Cassano, F. de Gasperin, M. Hoeft, A. Stroe, and G. J. White. Radio observations of the double-relic galaxy cluster Abell 1240. *MNRAS*, 478(2):2218–2233, August 2018. doi: 10.1093/mnras/sty1123.
- [45] Matthias Hoeft and Marcus Brügger. Radio signature of cosmological structure formation shocks. *MNRAS*, 375(1):77–91, February 2007. doi: 10.1111/j.1365-2966.2006.11111.x.

- [46] Matthias Hoeft, Kamlesh Rajpurohit, Denis Wittor, Gabriella di Gennaro, and Paola Domínguez-Fernández. On the Polarisation of Radio Relics. *Galaxies*, 10(1):10, January 2022. doi: 10.3390/galaxies10010010.
- [47] J. A. Högbom. Aperture Synthesis with a Non-Regular Distribution of Interferometer Baselines. *A&AS*, 15:417, June 1974.
- [48] H. T. Intema, S. van der Tol, W. D. Cotton, A. S. Cohen, I. M. van Bemmell, and H. J. A. Röttgering. Ionospheric calibration of low frequency radio interferometric observations using the peeling scheme. I. Method description and first results. *A&A*, 501(3):1185–1205, July 2009. doi: 10.1051/0004-6361/200811094.
- [49] Madoka Itahana, Motokazu Takizawa, Hiroki Akamatsu, Takaya Ohashi, Yoshitaka Ishisaki, Hajime Kawahara, and Reinout J. van Weeren. Suzaku observations of the galaxy cluster 1RXS J0603.3+4214: Implications of particle acceleration processes in the “Toothbrush” radio relic. *PASJ*, 67(6):113, December 2015. doi: 10.1093/pasj/psv084.
- [50] W. J. Jaffe. Origin and transport of electrons in the halo radio source in the Coma cluster. *ApJ*, 212:1–7, February 1977. doi: 10.1086/155011.
- [51] W. J. Jaffe and G. C. Perola. Dynamical Models of Tailed Radio Sources in Clusters of Galaxies. *A&A*, 26:423, August 1973.
- [52] Hyesung Kang, Dongsu Ryu, and T. W. Jones. Diffusive Shock Acceleration Simulations of Radio Relics. *ApJ*, 756(1):97, September 2012. doi: 10.1088/0004-637X/756/1/97.
- [53] Kravtsov and Borgani. Formation of galaxy clusters. 2012.
- [54] M. Markevitch. Chandra Observation of the Most Interesting Cluster in the Universe. 604:723, January 2006. doi: 10.48550/arXiv.astro-ph/0511345.
- [55] M. Markevitch, F. Govoni, G. Brunetti, and D. Jerius. Bow Shock and Radio Halo in the Merging Cluster A520. *ApJ*, 627(2):733–738, July 2005. doi: 10.1086/430695.
- [56] Maxim Markevitch and Alexey Vikhlinin. Shocks and cold fronts in galaxy clusters. *Phys. Rep.*, 443(1):1–53, May 2007. doi: 10.1016/j.physrep.2007.01.001.

- [57] A. R. Offringa and O. Smirnov. An optimized algorithm for multiscale wide-band deconvolution of radio astronomical images. *MNRAS*, 471(1):301–316, October 2017. doi: 10.1093/mnras/stx1547.
- [58] A. R. Offringa, B. McKinley, N. Hurley-Walker, F. H. Briggs, R. B. Wayth, D. L. Kaplan, M. E. Bell, L. Feng, A. R. Neben, J. D. Hughes, J. Rhee, T. Murphy, N. D. R. Bhat, G. Bernardi, J. D. Bowman, R. J. Cappallo, B. E. Corey, A. A. Deshpande, D. Emrich, A. Ewall-Wice, B. M. Gaensler, R. Goeke, L. J. Greenhill, B. J. Hazelton, L. Hindson, M. Johnston-Hollitt, D. C. Jacobs, J. C. Kasper, E. Kratzenberg, E. Lenc, C. J. Lonsdale, M. J. Lynch, S. R. McWhirter, D. A. Mitchell, M. F. Morales, E. Morgan, N. Kudryavtseva, D. Oberoi, S. M. Ord, B. Pindor, P. Procopio, T. Prabu, J. Riding, D. A. Roshi, N. Udaya Shankar, K. S. Srivani, R. Subrahmanyam, S. J. Tingay, M. Waterson, R. L. Webster, A. R. Whitney, A. Williams, and C. L. Williams. WSCLEAN: an implementation of a fast, generic wide-field imager for radio astronomy. *MNRAS*, 444(1):606–619, October 2014. doi: 10.1093/mnras/stu1368.
- [59] S. P. O’Sullivan, S. Brown, T. Robishaw, D. H. F. M. Schnitzeler, N. M. McClure-Griffiths, I. J. Feain, A. R. Taylor, B. M. Gaensler, T. L. Landecker, L. Harvey-Smith, and E. Carretti. Complex Faraday depth structure of active galactic nuclei as revealed by broad-band radio polarimetry. *MNRAS*, 421(4): 3300–3315, April 2012. doi: 10.1111/j.1365-2966.2012.20554.x.
- [60] Frazer N. Owen, Lawrence Rudnick, Jean Eilek, Urvashi Rau, Sanjay Bhatnagar, and Leonid Kogan. Wideband Very Large Array Observations of A2256. I. Continuum, Rotation Measure, and Spectral Imaging. *ApJ*, 794(1):24, October 2014. doi: 10.1088/0004-637X/794/1/24.
- [61] C. J. J. Pearce, R. J. van Weeren, F. Andrade-Santos, C. Jones, W. R. Forman, M. Brüggen, E. Bulbul, T. E. Clarke, R. P. Kraft, E. Medezinski, T. Mroczkowski, M. Nonino, P. E. J. Nulsen, S. W. Randall, and K. Umetsu. VLA Radio Observations of the HST Frontier Fields Cluster Abell 2744: The Discovery of New Radio Relics. *ApJ*, 845(1):81, August 2017. doi: 10.3847/1538-4357/aa7e2f.
- [62] R. A. Perley and B. J. Butler. An Accurate Flux Density Scale from 1 to 50 GHz. *ApJS*, 204(2):19, February 2013. doi: 10.1088/0067-0049/204/2/19.

- [63] Planck Collaboration, P. A. R. Ade, N. Aghanim, M. Arnaud, M. Ashdown, J. Aumont, C. Baccigalupi, A. J. Banday, R. B. Barreiro, R. Barrena, J. G. Bartlett, N. Bartolo, E. Battaner, R. Battye, K. Benabed, A. Benoît, A. Benoit-Lévy, J. P. Bernard, M. Bersanelli, P. Bielewicz, I. Bikmaev, H. Böhringer, A. Bonaldi, L. Bonavera, J. R. Bond, J. Borrill, F. R. Bouchet, M. Bucher, R. Burenin, C. Burigana, R. C. Butler, E. Calabrese, J. F. Cardoso, P. Carvalho, A. Catalano, A. Challinor, A. Chamballu, R. R. Chary, H. C. Chiang, G. Chon, P. R. Christensen, D. L. Clements, S. Colombi, L. P. L. Colombo, C. Combet, B. Comis, F. Couchot, A. Coulais, B. P. Crill, A. Curto, F. Cuttaia, H. Dahle, L. Danese, R. D. Davies, R. J. Davis, P. de Bernardis, A. de Rosa, G. de Zotti, J. Delabrouille, F. X. Désert, C. Dickinson, J. M. Diego, K. Dolag, H. Dole, S. Donzelli, O. Doré, M. Douspis, A. Ducout, X. Dupac, G. Efstathiou, P. R. M. Eisenhardt, F. Elsner, T. A. Enßlin, H. K. Eriksen, E. Falgarone, J. Fergusson, F. Feroz, A. Ferragamo, F. Finelli, O. Forni, M. Frailis, A. A. Fraisse, E. Franceschi, A. Frejsel, S. Galeotta, S. Galli, K. Ganga, R. T. Génova-Santos, M. Giard, Y. Giraud-Héraud, E. Gjerløw, J. González-Nuevo, K. M. Górski, K. J. B. Grainge, S. Gratton, A. Gregorio, A. Gruppuso, J. E. Gudmundsson, F. K. Hansen, D. Hanson, D. L. Harrison, A. Hempel, S. Henrot-Versillé, C. Hernández-Montenegro, D. Herranz, S. R. Hildebrandt, E. Hivon, M. Hobson, W. A. Holmes, A. Hornstrup, W. Hovest, K. M. Huffenberger, G. Hurier, A. H. Jaffe, T. R. Jaffe, T. Jin, W. C. Jones, M. Juvela, E. Keihänen, R. Keskitalo, I. Khamitov, T. S. Kisner, R. Kneissl, J. Knoche, M. Kunz, H. Kurki-Suonio, G. Lagache, J. M. Lamarre, A. Lasenby, M. Lattanzi, C. R. Lawrence, R. Leonardi, J. Lesgourgues, F. Levrier, M. Liguori, P. B. Lilje, M. Linden-Vørnle, M. López-Cañiego, P. M. Lubin, J. F. Macías-Pérez, G. Maggio, D. Maino, D. S. Y. Mak, N. Mandolesi, A. Mangilli, P. G. Martin, E. Martínez-González, S. Masi, S. Matarrese, P. Mazzotta, P. McGehee, S. Mei, A. Melchiorri, J. B. Melin, L. Mendes, A. Mennella, M. Migliaccio, S. Mitra, M. A. Miville-Deschênes, A. Moneti, L. Montier, G. Morgante, D. Mortlock, A. Moss, D. Munshi, J. A. Murphy, P. Naselsky, A. Nastasi, F. Nati, P. Natoli, C. B. Netterfield, H. U. Nørgaard-Nielsen, F. Noviello, D. Novikov, I. Novikov, M. Olamaie, C. A. Oxborrow, F. Paci, L. Pagano, F. Pajot, D. Paoletti, F. Pasian, G. Patanchon, T. J. Pearson, O. Perdereau, L. Perotto, Y. C. Perrott, F. Perrotta, V. Pettorino, F. Piacentini, M. Piat, E. Pierpaoli, D. Pietrobon, S. Plaszczyński, E. Pointe-

- couteau, G. Polenta, G. W. Pratt, G. Prézeau, S. Prunet, J. L. Puget, J. P. Rachen, W. T. Reach, R. Rebolo, M. Reinecke, M. Remazeilles, C. Renault, A. Renzi, I. Ristorcelli, G. Rocha, C. Rosset, M. Rossetti, G. Roudier, E. Rozo, J. A. Rubiño-Martín, C. Rumsey, B. Rusholme, E. S. Rykoff, M. Sandri, D. Santos, R. D. E. Saunders, M. Savelainen, G. Savini, M. P. Schammel, D. Scott, M. D. Seiffert, E. P. S. Shellard, T. W. Shimwell, L. D. Spencer, S. A. Stanford, D. Stern, V. Stolyarov, R. Stompor, A. Streblyanska, R. Sudiwala, R. Sunyaev, D. Sutton, A. S. Suur-Uski, J. F. Sygnet, J. A. Tauber, L. Terenzi, L. Toffolatti, M. Tomasi, D. Tramonte, M. Tristram, M. Tucci, J. Tuovinen, G. Umama, L. Valenziano, J. Valiviita, B. Van Tent, P. Vielva, F. Villa, L. A. Wade, B. D. Wandelt, I. K. Wehus, S. D. M. White, E. L. Wright, D. Yvon, A. Zacchei, and A. Zonca. Planck 2015 results. XXVII. The second Planck catalogue of Sunyaev-Zeldovich sources. *A&A*, 594:A27, September 2016. doi: 10.1051/0004-6361/201525823.
- [64] K. Rajpurohit, M. Hoeft, R. J. van Weeren, L. Rudnick, H. J. A. Röttgering, W. R. Forman, M. Brüggen, J. H. Croston, F. Andrade-Santos, W. A. Dawson, H. T. Intema, R. P. Kraft, C. Jones, and M. James Jee. Deep VLA Observations of the Cluster 1RXS J0603.3+4214 in the Frequency Range of 1-2 GHz. *ApJ*, 852(2):65, January 2018. doi: 10.3847/1538-4357/aa9f13.
- [65] K. Rajpurohit, M. Hoeft, F. Vazza, L. Rudnick, R. J. van Weeren, D. Wittor, A. Drabent, M. Brienza, E. Bonnassieux, N. Locatelli, R. Kale, and C. Dumba. New mysteries and challenges from the Toothbrush relic: wide-band observations from 550 MHz to 8 GHz. *A&A*, 636:A30, April 2020. doi: 10.1051/0004-6361/201937139.
- [66] K. Rajpurohit, D. Wittor, R. J. van Weeren, F. Vazza, M. Hoeft, L. Rudnick, N. Locatelli, J. Eilek, W. R. Forman, A. Bonafede, E. Bonnassieux, C. J. Riseley, M. Brienza, G. Brunetti, M. Brüggen, F. Loi, A. S. Rajpurohit, H. J. A. Röttgering, A. Botteon, T. E. Clarke, A. Drabent, P. Domínguez-Fernández, G. Di Gennaro, and F. Gastaldello. Understanding the radio relic emission in the galaxy cluster MACS J0717.5+3745: Spectral analysis. *A&A*, 646:A56, February 2021. doi: 10.1051/0004-6361/202039428.
- [67] P. H. Richter. Estimating Errors in Least-Squares Fitting. *Telecommunications and Data Acquisition Progress Report*, 122:107–137, April 1995.

- [68] C. J. Riseley, E. Bonmassieux, T. Vernstrom, T. J. Galvin, A. Chokshi, A. Botteon, K. Rajpurohit, S. W. Duchesne, A. Bonafede, L. Rudnick, M. Hoeft, B. Quici, D. Eckert, M. Brienza, C. Tasse, E. Carretti, J. D. Collier, J. M. Diego, L. Di Mascolo, A. M. Hopkins, M. Johnston-Hollitt, R. R. Keel, B. S. Koribalski, and T. H. Reiprich. Radio fossils, relics, and haloes in Abell 3266: cluster archaeology with ASKAP-EMU and the ATCA. *MNRAS*, 515(2): 1871–1896, September 2022. doi: 10.1093/mnras/stac1771.
- [69] Piero Rosati, Stefano Borgani, and Colin Norman. The Evolution of X-ray Clusters of Galaxies. *ARA&A*, 40:539–577, January 2002. doi: 10.1146/annurev.astro.40.120401.150547.
- [70] Lawrence Rudnick, Debora M. Katz-Stone, and Martha C. Anderson. Do Relativistic Electrons either Gain or Lose Energy, outside of Extragalactic Nuclei? *ApJS*, 90:955, February 1994. doi: 10.1086/191931.
- [71] Craig L. Sarazin. X-ray emission from clusters of galaxies. *Reviews of Modern Physics*, 58(1):1–115, January 1986. doi: 10.1103/RevModPhys.58.1.
- [72] Craig L. Sarazin and Paul M. Ricker. Off-Axis Cluster Mergers: Effects of a Strongly Peaked Dark Matter Profile. *ApJ*, 561(2):621–644, November 2001. doi: 10.1086/323365.
- [73] Craig L. Sarazin, L. Feretti, Isabella Gioia, and G. Giovannini. Merging processes in galaxy cluster. volume 272, 06 2002. ISBN 978-1-4020-0531-2. doi: 10.1007/0-306-48096-4.
- [74] Anna M. M. Scaife and George H. Heald. A broad-band flux scale for low-frequency radio telescopes. *MNRAS*, 423(1):L30–L34, June 2012. doi: 10.1111/j.1745-3933.2012.01251.x.
- [75] R. Schlickeiser, A. Sievers, and H. Thiemann. The diffuse radio emission from the Coma cluster. *A&A*, 182:21–35, August 1987.
- [76] T. W. Shimwell, H. J. A. Röttgering, P. N. Best, W. L. Williams, T. J. Djkema, F. de Gasperin, M. J. Hardcastle, G. H. Heald, D. N. Hoang, A. Hornefer, H. Intema, E. K. Mahony, S. Mandal, A. P. Mechev, L. Morabito, J. B. R. Oonk, D. Rafferty, E. Retana-Montenegro, J. Sabater, C. Tasse, R. J. van Weeren, M. Brüggen, G. Brunetti, K. T. Chyży, J. E. Conway, M. Haverkorn, N. Jackson, M. J. Jarvis, J. P. McKean, G. K. Miley, R. Morganti, G. J.

- White, M. W. Wise, I. M. van Bemmell, R. Beck, M. Brienza, A. Bonafede, G. Calistro Rivera, R. Cassano, A. O. Clarke, D. Cseh, A. Deller, A. Drabent, W. van Driel, D. Engels, H. Falcke, C. Ferrari, S. Fröhlich, M. A. Garrett, J. J. Harwood, V. Heesen, M. Hoeft, C. Horellou, F. P. Israel, A. D. Kapińska, M. Kunert-Bajraszewska, D. J. McKay, N. R. Mohan, E. Orrú, R. F. Pizzo, I. Prandoni, D. J. Schwarz, A. Shulevski, M. Sipior, D. J. B. Smith, S. S. Sridhar, M. Steinmetz, A. Stroe, E. Varenius, P. P. van der Werf, J. A. Zensus, and J. T. L. Zwart. The LOFAR Two-metre Sky Survey. I. Survey description and preliminary data release. *A&A*, 598:A104, February 2017. doi: 10.1051/0004-6361/201629313.
- [77] T. W. Shimwell, C. Tasse, M. J. Hardcastle, A. P. Mechev, W. L. Williams, P. N. Best, H. J. A. Röttgering, J. R. Callingham, T. J. Dijkema, F. de Gasperin, D. N. Hoang, B. Hugo, M. Mirmont, J. B. R. Oonk, I. Prandoni, D. Rafferty, J. Sabater, O. Smirnov, R. J. van Weeren, G. J. White, M. Atemkeng, L. Bester, E. Bonnassieux, M. Brügger, G. Brunetti, K. T. Chyży, R. Cochrane, J. E. Conway, J. H. Croston, A. Danezi, K. Duncan, M. Haverkorn, G. H. Heald, M. Iacobelli, H. T. Intema, N. Jackson, M. Jamrozny, M. J. Jarvis, R. Lakhoo, M. Mevius, G. K. Miley, L. Morabito, R. Morganti, D. Nisbet, E. Orrú, S. Perkins, R. F. Pizzo, C. Schrijvers, D. J. B. Smith, R. Vermeulen, M. W. Wise, L. Alegre, D. J. Bacon, I. M. van Bemmell, R. J. Beswick, A. Bonafede, A. Botteon, S. Bourke, M. Brienza, G. Calistro Rivera, R. Cassano, A. O. Clarke, C. J. Conselice, R. J. Dettmar, A. Drabent, C. Dumba, K. L. Emig, T. A. Enßlin, C. Ferrari, M. A. Garrett, R. T. Génova-Santos, A. Goyal, G. Gürkan, C. Hale, J. J. Harwood, V. Heesen, M. Hoeft, C. Horellou, C. Jackson, G. Kokotanekov, R. Kondapally, M. Kunert-Bajraszewska, V. Mahatma, E. K. Mahony, S. Mandal, J. P. McKean, A. Merloni, B. Mingo, A. Miskolczy, S. Mooney, B. Nikiel-Wroczyński, S. P. O’Sullivan, J. Quinn, W. Reich, C. Roskowiński, A. Rowlinson, F. Savini, A. Saxena, D. J. Schwarz, A. Shulevski, S. S. Sridhar, H. R. Stacey, S. Urquhart, M. H. D. van der Wiel, E. Varenius, B. Webster, and A. Wilber. The LOFAR Two-metre Sky Survey. II. First data release. *A&A*, 622:A1, February 2019. doi: 10.1051/0004-6361/201833559.
- [78] T. W. Shimwell, M. J. Hardcastle, C. Tasse, P. N. Best, H. J. A. Röttgering, W. L. Williams, A. Botteon, A. Drabent, A. Mechev, A. Shulevski, R. J. van Weeren, L. Bester, M. Brügger, G. Brunetti, J. R. Callingham, K. T.

Chyży, J. E. Conway, T. J. Dijkema, K. Duncan, F. de Gasperin, C. L. Hale, M. Haverkorn, B. Hugo, N. Jackson, M. Mevius, G. K. Miley, L. K. Morabito, R. Morganti, A. Offringa, J. B. R. Oonk, D. Rafferty, J. Sabater, D. J. B. Smith, D. J. Schwarz, O. Smirnov, S. P. O’Sullivan, H. Vedantham, G. J. White, J. G. Albert, L. Alegre, B. Asabere, D. J. Bacon, A. Bonafede, E. Bonnassieux, M. Brienza, M. Bilicki, M. Bonato, G. Calistro Rivera, R. Cassano, R. Cochrane, J. H. Croston, V. Cuciti, D. Dallacasa, A. Danezi, R. J. Dettmar, G. Di Gennaro, H. W. Edler, T. A. Enßlin, K. L. Emig, T. M. O. Franzen, C. García-Vergara, Y. G. Grange, G. Gürkan, M. Hajduk, G. Heald, V. Heesen, D. N. Hoang, M. Hoeft, C. Horellou, M. Iacobelli, M. Jamrozy, V. Jelić, R. Kondapally, P. Kukreti, M. Kunert-Bajraszewska, M. Magliocchetti, V. Mahatma, K. Małek, S. Mandal, F. Massaro, Z. Meyer-Zhao, B. Mingo, R. I. J. Mostert, D. G. Nair, S. J. Nakoneczny, B. Nikiel-Wroczyński, E. Orrú, U. Pajdosz-Śmierciak, T. Pasini, I. Prandoni, H. E. van Piggelen, K. Rajpurohit, E. Retana-Montenegro, C. J. Riseley, A. Rowlinson, A. Saxena, C. Schrijvers, F. Sweijen, T. M. Siewert, R. Timmerman, M. Vaccari, J. Vink, J. L. West, A. Wołowska, X. Zhang, and J. Zheng. The LOFAR Two-metre Sky Survey. V. Second data release. *A&A*, 659:A1, March 2022. doi: 10.1051/0004-6361/202142484.

- [79] Samuel W. Skillman, Hao Xu, Eric J. Hallman, Brian W. O’Shea, Jack O. Burns, Hui Li, David C. Collins, and Michael L. Norman. Cosmological Magnetohydrodynamic Simulations of Galaxy Cluster Radio Relics: Insights and Warnings for Observations. *ApJ*, 765(1):21, March 2013. doi: 10.1088/0004-637X/765/1/21.
- [80] C. Stuardi, A. Bonafede, D. Wittor, F. Vazza, A. Botteon, N. Locatelli, D. Dallacasa, N. Golovich, M. Hoeft, R. J. van Weeren, M. Brüggen, and F. de Gasperin. Particle re-acceleration and Faraday-complex structures in the RXC J1314.4-2515 galaxy cluster. *MNRAS*, 489(3):3905–3926, November 2019. doi: 10.1093/mnras/stz2408.
- [81] C. Stuardi, A. Bonafede, K. Rajpurohit, M. Brüggen, F. de Gasperin, D. Hoang, R. J. van Weeren, and F. Vazza. Using the polarization properties of double radio relics to probe the turbulent compression scenario. *A&A*, 666: A8, October 2022. doi: 10.1051/0004-6361/202244179.
- [82] C. Tasse, T. Shimwell, M. J. Hardcastle, S. P. O’Sullivan, R. van Weeren,

- P. N. Best, L. Bester, B. Hugo, O. Smirnov, J. Sabater, G. Calistro-Rivera, F. de Gasperin, L. K. Morabito, H. Röttgering, W. L. Williams, M. Bonato, M. Bondi, A. Botteon, M. Brüggen, G. Brunetti, K. T. Chyży, M. A. Garrett, G. Gürkan, M. J. Jarvis, R. Kondapally, S. Mandal, I. Prandoni, A. Repetti, E. Retana-Montenegro, D. J. Schwarz, A. Shulevski, and Y. Wiaux. The LOFAR Two-meter Sky Survey: Deep Fields Data Release 1. I. Direction-dependent calibration and imaging. *A&A*, 648:A1, April 2021. doi: 10.1051/0004-6361/202038804.
- [83] M. P. van Haarlem, M. W. Wise, A. W. Gunst, G. Heald, J. P. McKean, J. W. T. Hessels, A. G. de Bruyn, R. Nijboer, J. Swinbank, R. Fallows, M. Brentjens, A. Nelles, R. Beck, H. Falcke, R. Fender, J. Hörandel, L. V. E. Koopmans, G. Mann, G. Miley, H. Röttgering, B. W. Stappers, R. A. M. J. Wijers, S. Zaroubi, M. van den Akker, A. Alexov, J. Anderson, K. Anderson, A. van Ardenne, M. Arts, A. Asgekar, I. M. Avruch, F. Batejat, L. Bähren, M. E. Bell, M. R. Bell, I. van Bemmelen, P. Bennema, M. J. Bentum, G. Bernardi, P. Best, L. Bîrzan, A. Bonafede, A. J. Boonstra, R. Braun, J. Bregman, F. Breitling, R. H. van de Brink, J. Broderick, P. C. Broekema, W. N. Brouw, M. Brüggen, H. R. Butcher, W. van Cappellen, B. Ciardi, T. Coenen, J. Conway, A. Coolen, A. Corstanje, S. Damstra, O. Davies, A. T. Deller, R. J. Dettmar, G. van Diepen, K. Dijkstra, P. Donker, A. Door-duin, J. Dromer, M. Drost, A. van Duin, J. Eislöffel, J. van Enst, C. Ferrari, W. Frieswijk, H. Gankema, M. A. Garrett, F. de Gasperin, M. Gerbers, E. de Geus, J. M. Grießmeier, T. Grit, P. Gruppen, J. P. Hamaker, T. Hassall, M. Hoeft, H. A. Holties, A. Horneffer, A. van der Horst, A. van Houwelingen, A. Huijgen, M. Iacobelli, H. Intema, N. Jackson, V. Jelic, A. de Jong, E. Juette, D. Kant, A. Karastergiou, A. Koers, H. Kollen, V. I. Kondratiev, E. Kooistra, Y. Koopman, A. Koster, M. Kuniyoshi, M. Kramer, G. Kuper, P. Lambropoulos, C. Law, J. van Leeuwen, J. Lemaître, M. Loose, P. Maat, G. Macario, S. Markoff, J. Masters, R. A. McFadden, D. McKay-Bukowski, H. Meijering, H. Meulman, M. Mevius, E. Middelberg, R. Millenaar, J. C. A. Miller-Jones, R. N. Mohan, J. D. Mol, J. Morawietz, R. Morganti, D. D. Mulcahy, E. Mulder, H. Munk, L. Nieuwenhuis, R. van Nieuwpoort, J. E. Noordam, M. Norden, A. Noutsos, A. R. Offringa, H. Olofsson, A. Omar, E. Orrú, R. Overeem, H. Paas, M. Pandey-Pommier, V. N. Pandey, R. Pizzo, A. Polatidis, D. Rafferty, S. Rawlings, W. Reich, J. P. de Reijer, J. Reitsma, G. A.

- Renting, P. Riemers, E. Rol, J. W. Romein, J. Roosjen, M. Ruiter, A. Scaife, K. van der Schaaf, B. Scheers, P. Schellart, A. Schoenmakers, G. Schoonderbeek, M. Serylak, A. Shulevski, J. Sluman, O. Smirnov, C. Sobey, H. Spreeuw, M. Steinmetz, C. G. M. Sterks, H. J. Stiepel, K. Stuurwold, M. Tagger, Y. Tang, C. Tasse, I. Thomas, S. Thoudam, M. C. Toribio, B. van der Tol, O. Usov, M. van Veelen, A. J. van der Veen, S. ter Veen, J. P. W. Verbiest, R. Vermeulen, N. Vermaas, C. Vocks, C. Vogt, M. de Vos, E. van der Wal, R. van Weeren, H. Weggemans, P. Weltevrede, S. White, S. J. Wijnholds, T. Wilhelmsson, O. Wucknitz, S. Yatawatta, P. Zarka, A. Zensus, and J. van Zwieten. LOFAR: The LOw-Frequency ARray. *A&A*, 556:A2, August 2013. doi: 10.1051/0004-6361/201220873.
- [84] R. J. van Weeren, M. Brüggen, H. J. A. Röttgering, and M. Hoeft. Using double radio relics to constrain galaxy cluster mergers: a model of double radio relics in CIZA J2242.8+5301. *MNRAS*, 418(1):230–243, November 2011. doi: 10.1111/j.1365-2966.2011.19478.x.
- [85] R. J. van Weeren, A. Bonafede, H. Ebeling, A. C. Edge, M. Brüggen, G. Giovannini, M. Hoeft, and H. J. A. Röttgering. Diffuse radio emission in MACS J1752.0+4440. *MNRAS*, 425(1):L36–L40, September 2012. doi: 10.1111/j.1745-3933.2012.01301.x.
- [86] R. J. van Weeren, H. J. A. Röttgering, H. T. Intema, L. Rudnick, M. Brüggen, M. Hoeft, and J. B. R. Oonk. The “toothbrush-relic”: evidence for a coherent linear 2-Mpc scale shock wave in a massive merging galaxy cluster? *A&A*, 546:A124, October 2012. doi: 10.1051/0004-6361/201219000.
- [87] R. J. van Weeren, F. de Gasperin, H. Akamatsu, M. Brüggen, L. Ferretti, H. Kang, A. Stroe, and F. Zandanel. Diffuse Radio Emission from Galaxy Clusters. *Space Sci. Rev.*, 215(1):16, February 2019. doi: 10.1007/s11214-019-0584-z.
- [88] R. J. van Weeren, T. W. Shimwell, A. Botteon, G. Brunetti, M. Brüggen, J. M. Boxelaar, R. Cassano, G. Di Gennaro, F. Andrade-Santos, E. Bonnassieux, A. Bonafede, V. Cuciti, D. Dallacasa, F. de Gasperin, F. Gastaldello, M. J. Hardcastle, M. Hoeft, R. P. Kraft, S. Mandal, M. Rossetti, H. J. A. Röttgering, C. Tasse, and A. G. Wilber. LOFAR observations of galaxy clusters

- in HETDEX. Extraction and self-calibration of individual LOFAR targets. *A&A*, 651:A115, July 2021. doi: 10.1051/0004-6361/202039826.
- [89] Reinout J. van Weeren, Huub J. A. Röttgering, Marcus Brüggen, and Matthias Hoeft. Particle Acceleration on Megaparsec Scales in a Merging Galaxy Cluster. *Science*, 330(6002):347, October 2010. doi: 10.1126/science.1194293.
- [90] Reinout J. Van Weeren, Felipe Andrade-Santos, William Dawson, Nathan Golovich, Dharam V. Lal, Hyesung Kang, Dongsu Ryu, Marcus Brüggen, Georgiana Ogorean, William R. Forman, Christine Jones, Vinicius Placco, Rafael Santucci, David M. Wittman, M. James Lee, Ralph P. Kraft, David Sobral, Andra Stroe, and Kevin Fogarty. Discovery of Electron Re-Acceleration at Galaxy Cluster Shocks. In *American Astronomical Society Meeting Abstracts #229*, volume 229 of *American Astronomical Society Meeting Abstracts*, page 404.03, January 2017.
- [91] F. Vazza and M. Brüggen. Do radio relics challenge diffusive shock acceleration? *MNRAS*, 437(3):2291–2296, January 2014. doi: 10.1093/mnras/stt2042.
- [92] F. Vazza, M. Brüggen, R. van Weeren, A. Bonafede, K. Dolag, and G. Brunetti. Why are central radio relics so rare? *MNRAS*, 421(3):1868–1873, April 2012. doi: 10.1111/j.1365-2966.2011.20160.x.
- [93] F. Vazza, S. Ettori, M. Roncarelli, M. Angelinelli, M. Brüggen, and C. Gheller. Detecting shocked intergalactic gas with X-ray and radio observations. *A&A*, 627:A5, July 2019. doi: 10.1051/0004-6361/201935439.
- [94] W. Voges, B. Aschenbach, Th. Boller, H. Bräuninger, U. Briel, W. Burkert, K. Dennerl, J. Englhauser, R. Gruber, F. Haberl, G. Hartner, G. Hasinger, M. Kürster, E. Pfeffermann, W. Pietsch, P. Predehl, C. Rosso, J. H. M. M. Schmitt, J. Trümper, and H. U. Zimmermann. The ROSAT all-sky survey bright source catalogue. *A&A*, 349:389–405, September 1999. doi: 10.48550/arXiv.astro-ph/9909315.
- [95] J. F. C. Wardle and P. P. Kronberg. The linear polarization of quasi-stellar radio sources at 3.71 and 11.1 centimeters. *ApJ*, 194:249, January 1974. doi: 10.1086/153240.

- [96] M. A. G. Willson. Radio observations of the cluster of galaxies in Coma Berenices - the 5C4 survey. *MNRAS*, 151:1, January 1970. doi: 10.1093/mnras/151.1.1.
- [97] D. Wittor, F. Vazza, and M. Brüggen. Testing cosmic ray acceleration with radio relics: a high-resolution study using MHD and tracers. *MNRAS*, 464(4):4448–4462, February 2017. doi: 10.1093/mnras/stw2631.
- [98] D. Wittor, S. Ettori, F. Vazza, K. Rajpurohit, M. Hoeft, and P. Domínguez-Fernández. Exploring the spectral properties of radio relics - I: integrated spectral index and Mach number. *MNRAS*, 506(1):396–414, September 2021. doi: 10.1093/mnras/stab1735.
- [99] D. Wittor, M. Brüggen, P. Grete, and K. Rajpurohit. A morphological analysis of the substructures in radio relics. *MNRAS*, 523(1):701–719, July 2023. doi: 10.1093/mnras/stad1463.
- [100] Denis Wittor. On the Challenges of Cosmic-Ray Proton Shock Acceleration in the Intracluster Medium. *New A*, 85:101550, May 2021. doi: 10.1016/j.newast.2020.101550.
- [101] John ZuHone and Yuanyuan Su. The Merger Dynamics of the X-Ray-Emitting Plasma in Clusters of Galaxies. art. 93, 2022. doi: 10.1007/978-981-16-4544-0\_124-1.
- [102] F. Zwicky. On the Masses of Nebulae and of Clusters of Nebulae. *ApJ*, 86:217, October 1937. doi: 10.1086/143864.